

ABSTRACT

HOOK, DAVID ADAM. Physical Mechanisms of Failure, Ultralow Partial Pressure Lubrication, and the Reservoir Effect in MEMS. (Under the direction of Professor Jacqueline Krim.)

The aim of this work is to examine the effectiveness of self-assembled monolayer (SAM) coatings as long term lubrication coatings in microsystems, to examine the failure regimes of SAM coated devices, to examine the role of mobility in adsorbed lubricating films, and to examine evolution of the coefficient of friction of devices surrounded by ultralow partial pressures of alcohols up to saturation. Finally the role of self assembled monolayers in vapor phase lubrication is examined. Self-assembled monolayers are ubiquitous in fabrication of free-standing microdevices because of their ability to prevent release related and dormancy related stiction. However their ability to lubricate under sliding and normal contact conditions is not well documented. It can be shown that the energy dissipated per unit area in one sliding cycle due to friction is significant under general loading conditions. Therefore from an energy dissipated standpoint the bond energies of the silane molecules should not be enough to withstand even a short number of cycles. An extension of this is the energy imparted to the surface through a normal loading cycle through a loss of kinetic energy. It can also be shown that this is enough to break the silicon oxygen bonds however this is over a longer time scale than in sliding. Also there is an open question on the role of mobile and non-mobile adsorbed species on friction. Is the mobility of a molecule/layer on a surface an indicator of the effectiveness

of the lubrication potential of the layer? Do submonolayer coverages of alcohols “lock-up” to contacting surfaces by disrupting non-corroged potentials? Is there a distinct lowering of frictional forces at the formation of a monolayer? Controlled adsorption of mobile and non-mobile species on rubbing contacts is necessary to elucidate this physical relationship. To accomplish this one must take into account that friction measurements are highly scale dependant. Therefore to ensure the accuracy of measurements relating to microsystem contact conditions experiments must be conducted on actual microdevices.

In the work presented here I have used microelectromechanical system (MEMS) tribometers to measure the friction and adhesive forces of SAM coated surfaces over the course of many sliding cycles as well as normal contacting cycles. It is shown that robustly adhered monolayer coatings degrade extremely rapidly and there is a direct correlation between the respective energies dissipated both in sliding and normal contacting cycles and the time it takes for the layers to degrade. Also it is shown that devices fail in two main modes: one where wear of the devices in the form of dislocation of polysilicon grains leads to a low/adhesion high wear regime and another where high adhesive forces are developed and the devices fail with little to no wear. In the studies of ultra low partial pressure lubrication of devices a clear correlation between lubricant mobility to device lubrication is observed even in the presence of a vapor, which should in principle be able to replenish removed lubricant in between sliding cycles. We show that ultralow partial pressures nominally corresponding to submonolayer coverages of ethanol and pentanol show a distinct decrease in coefficient of friction and lubricate MEMS microcontacts however this is only loosely correlated to their effectiveness as

lubricants. Pentanol was only shown to lubricate at the point at which it becomes mobile on the surface where as ethanol is mobile at all times and lubricates effectively at very low partial pressures. Trifluoroethanol is not mobile at any portion of its isotherm and does not effectively lubricate the contacts. We also show the ability of the surrounding SAM to act as a lubricant reservoir when vapors of ethanol are removed. The correlation of lubricant mobility to lubrication can be used to predict the effectiveness to new lubricants as well as allow for the tailoring of lubricants to specific applications.

Physical Mechanisms of Failure, Ultralow Partial Pressure Lubrication, and the Reservoir
Effect in MEMS

by
David Adam Hook

A dissertation submitted to the Graduate Faculty of
North Carolina State University
in partial fulfillment of the
requirements for the degree of
Doctor of Philosophy

Physics

Raleigh, North Carolina

2011

APPROVED BY:

Prof. Jacqueline Krim
Chair of Advisory Committee

Prof. Donald W. Brenner

Prof. Kenan Gundogdu

Prof. Hans Hallen

DEDICATION

To all of my family and friends, especially to my mom, dad, and little brother. I could not have done this without your love a support over these years. Thank you.

BIOGRAPHY

David Adam Hook was born in Gastonia, North Carolina to David and Susan Hook and grew up in Bessemer City, NC. He was always inquisitive and interested in how things worked. He constantly read science books and constructed things out of legos. Throughout his life he played baseball every summer up through high school and although he wasn't the most athletic of the teams he tried harder than most and became successful enough to be a starting pitcher his senior year. This taught him valuable lessons about work and accomplishing what you started. He grew up with a large extended family that still to this day travels to the beach together and has been a constant source of support and love. This provided a strong loving foundation to build upon. He played saxophone in the high school band and taught himself to play guitar. Math and science came easy to Adam and after spending two years in Montessori School prior to Junior High decided that he was going to study Physics in college. In his junior year of college he realized he had no idea what to do with a bachelors degree in physics and asked his classical mechanics professor Dr. Jacqueline Krim if he could come and work in her lab. After experiencing laboratory physics work Adam discovered his love and aptitude for experimental physics in particular surface analysis and surface physics. He loves working with his hands and designing and performing experiments and playing with big toys. He plans to stay in the surface analysis field and would like to remain working with the development of Microsystems and their applications.

ACKNOWLEDGEMENTS

I would like to thank my advisor, Professor Jacqueline Krim for her unending encouragement, support, positive attitude, boundless understanding for mistakes, and patience throughout all phases of research, my academic career, and development as a person. Allowing me to come and work in the lab as an undergrad is one of the keys to my success as a graduate student. The words fail to describe the respect and admiration I have for her.

I would like to thank Dr. Michael T. Dugger at Sandia National Labs for taking me under his wing during summer research at Sandia National Laboratories, allowing me to develop at my own pace, and providing me with a view of life and research that I would have otherwise been deprived of. I am indebted to him.

I am overwhelmingly grateful to all members of my family for their support and encouragement. My utmost thanks and deepest gratitude goes to my Mom and Dad. Their unconditional love and unwavering support have been essential to my completion of this monumental task. I would also like to thank my brother, my cousins, my grandmothers and late grandfathers for extending my support group to an extent that I have never in my life felt far from home.

I would like to acknowledge the members of the nanoscale tribology and thank them for all of their useful discussions and assisting in all of the issues that have arisen in the lab over the years. In particular I would like to thank Brendan Miller for his time since our projects were so closely linked.

I would also like to thank Dr Peter Taborek for housing me on my visit to UC Irvine and to Dr Jim Rutledge for his work on the capacitive ringdown technique and useful discussions.

This work was partially funded by Sandia National Labs and my time at NC State was fully funded by the AFOSR Extreme Friction MURI Grant No.

TABLE OF CONTENTS

LIST OF TABLES	ix
LIST OF FIGURES	x
CHAPTER 1: Introduction	1
1.1 History of Tribology and the Role of Contact Mechanics	1
1.2 Ploughing and Adhesive Friction.....	4
1.3 Atomic Lubrication.....	6
CHAPTER 2: MEMS	13
2.1 MEMS and Their Applications.....	13
2.2 Micromachining.....	14
2.3 Release Related Stiction	19
2.4 Summary and Research Objective	23
CHAPTER 3: Experimental Set-up	26
3.1 UHV and MEMS Mount.....	26
3.2 RS594 and Force Constants	30
3.3 Device Control	35
3.4 Ringdown and Failure Test Procedure.....	36
CHAPTER 4: Tribological Degradation of Fluorocarbon Coated Silicon Microdevice Surfaces in Normal and Sliding Contact.....	42
4.1 Introducion	43
4.2 Experimental	45
4.2.1 MEMS Tribometer Fabrication and Monolayer Treatment.....	45

4.2.2 MEMS Operation and Set-Up.....	48
4.2.3 Normal Cyclic Contact	50
4.2.4 Sliding Cyclic Contact	52
4.3 Results and Discussion	54
4.3.1 Normal Contact.....	54
4.3.2 Sliding Contact.....	58
4.4 Summary.....	61
4.5 Acknowledgements.....	62
CHAPTER 5: Wear of Polysilicon Surface Micromachines Operated in High Vacuum..	65
5.1 Introduction.....	66
5.2 Description of the Test Micromachine	69
5.3 Experimental Procedures	74
5.4 Results.....	76
5.5 Discussion.....	88
5.6 Conclusion	93
5.7 Acknowledgements.....	95
CHAPTER 6: Vapor-phase Lubrication at Ultra Low Partial Pressures of Ethanol	98
6.1 Introduction.....	99
6.2 Experimental Details and Results	101
6.3 Discussion.....	109
6.4 SAM Reservoir Experiment.....	115
6.5 Conclusion	117

6.6 Acknowledgements.....	117
CHAPTER 6 Supplemental Material: Methods and Materials.....	120
6.7 Device Description Operation and Chamber Preparation.....	120
6.8 SAM Effect.....	122
6.9 Quartz Crystal Microbalance Coverage and Slitptime Measurements.....	124
6.10 Vapor Flux Rates	126
CHAPTER 7: Evalutaion of Oxygen Plasma and UV Ozone Methods for Cleaning of Occluded Areas in MEMS Devices	129
7.1 Introduction.....	130
7.2 Experimental Setup.....	131
7.2.1 MEMS Flap Structure Fabrication and Monolayer Treatment	131
7.2.2 Cleaning Processes and ToF-SIMS Analysis	135
7.3 Results and Discussion	136
7.4 Summary.....	139
7.5 Acknowledgments.....	140
CHAPTER 8: Conclusions and Future Work.....	149
8.1 Summary of Results and Impact.....	149
8.2 Future Work.....	150

LIST OF TABLES

Table 3.1 Device 1 Bond Pad / Wired Pin Layout.....	33
Table 3.2 Device 2 Bond Pad / Wired Pin Layout.....	33
Table 3.3 Device 3 Bond Pad / Wired Pin Layout.....	33
Table 3.4 Device 4 Bond Pad / Wired Pin Layout.....	34
Table 3.5 Force Constants.....	34
Table 5.1 Chemical Composition	87
Table 6.1 Physical Properties of Test Lubricants.	111
Table 6.2 Results of Kelvin Equation Calculations	111

LIST OF FIGURES

Figure 1.1 Brenner Model.....	10
Figure 2.1 Bulk Micromachining.....	16
Figure 2.2 Surface Micromachining.....	19
Figure 2.3 Release Related Stiction.....	20
Figure 3.1 Experimental Chamber.....	28
Figure 3.2 Bonding Diagram.....	29
Figure 3.3 RS594 Chip.....	32
Figure 3.4 Dual Measurement Techniques.....	37
Figure 4.1 MEMS Sidewall Tribometer Chapter 4.....	45
Figure 4.2 FOTAS Reaction Process.....	47
Figure 4.3 Adhesion Measurement Waveform.....	50
Figure 4.4 AFM Image of Sidewall Roughness.....	52
Figure 4.5 Oscillation Waveform.....	53
Figure 4.6 Adhesion Force Data.....	55
Figure 4.7 SEM Image 300,000 Normal Cycles.....	57
Figure 4.8 Amplitude versus Cycles.....	59
Figure 4.9 SEM Image 800 Sliding Cycles.....	60
Figure 5.1 MEMS Sidewall Tribometer Chapter 5.....	70
Figure 5.2 SEM Micrograph Critical Points of Device.....	73
Figure 5.3 Adhesion Force Versus Sliding Cycles.....	78
Figure 5.4 SEM Micrograph High Adhesion Low Wear Device.....	80

Figure 5.5 SEM Micrograph Low Adhesion High Wear Device Wear Debris	82
Figure 5.6 SEM Micrograph Low Adhesion High Wear Device Smeared Material.....	84
Figure 5.7 TEM and SAD Pattern of Smeared Material.....	86
Figure 5.8 Bright Field TEM of Wear Debris.....	88
Figure 6.1 Custom Vacuum Chamber and Measurement Device.....	102
Figure 6.2 Ultra Low Coverage Ethanol Lubrication	107
Figure 6.3 Lifetimes of Devices in Vapors of Alcohols	114
Figure 6.4 SAM Reservoir Effect	116
Figure 6.5 GAB fit of Ethanol Isotherm	125
Figure 6.6 Friction Coefficient Versus Coverage.....	127
Figure 7.1 SEM Device 1 and 3.....	141
Figure 7.2 SEM Device 2 and 4.....	142
Figure 7.3 Microengine and RF MicroSwitch	143
Figure 7.4 FOTAS Reaction Process	143
Figure 7.5 Optical Micrograph of Devices Prepared for Analysis	144
Figure 7.6 ToF-SIMS Mean Ion Image	145
Figure 7.7 AXSIA Analysis of FOTAS Component	145
Figure 7.8 AXSIA Analysis of Aluminum Component.....	146

Chapter 1: Introduction

1.1 History of Tribology and the Role of Contact Mechanics

Man has long had a varying relationship with friction. Looking back to prehistory, early man's working knowledge of friction led to the creation of fire by rubbing sticks together and use of wear to fashion tools. It is also known that man's working knowledge of the negative affects of friction led to the Egyptian's using water to reduce friction between wooden sleds and wooden platforms on which they were sliding and the use of lubricants in the construction of the pyramids.¹ However it has been stated that the lack of thorough understanding of the fundamental science behind friction has cost industrialized countries between 2% and 9% of their gross national product. For the United States in 2000 that amounted to nearly \$420 billion dollars.² In fact it wasn't until 1966 that the science of studying friction, wear, and lubrication officially had a name in the scientific community. In that year the English government reported that industry could save £515 million per annum by better knowledge of the subject of friction however unification of the field was required for technology to move forward. It determined that the term "tribology", coined by H. Peter Jost, be used.³ The word being derived from the greek root word *tribos*, meaning "rubbing" and -ology meaning "the study of".

The first officially recorded scientific study of friction was conducted by Leonardo Da Vinci 200 years prior to Isaac Newton describing the phenomenon of force. In his notebooks Da Vinci states "The friction made by the same weight will be of equal

resistance at the beginning of its movement although the contact may be of different breadth and length.” And, “Friction produces double the amount of effort if the weight be doubled.” These findings were however never published and in 1699 Guillaume Amontons independently published a work describing the exact same phenomena however in terms of force giving the equation:

$$F = \mu N \quad (1.1)$$

known now as Amontons’ Law.⁴ Here F is the force of friction opposing motion, μ is the coefficient of friction, and N is the normal force. This implies as Da Vinci stated the friction is directly proportional to the applied load and is seemingly independent of the area of contact. This result is purely phenomenological and gives no indication of the fundamental science behind friction. In fact Amontons’ results immediately provoked controversy about the microscopic origins of friction.⁵ It was well known at the time that surfaces are not perfectly smooth. In fact they are covered in microscopic asperities. Amontons came up with the idea that friction was due to the force required to lift the load up the slopes of the asperities. This theory was mathematically examined by Leonard Euler in the mid the 1700’s. It gives a simple block on an inclined plane model of friction with no necessary fundamental interacting forces between the two bodies and the coefficient of friction $\mu = \tan \alpha$, where α is the slope of the triangular asperities and is independent of contact area. Desangulier proposed another idea about the origins of friction. He described the adhesion or cohesion of the surfaces as the fundamental mechanism not the roughness. This idea however was widely discounted since adhesion

is dependant on surface area and therefore the resulting friction must be dependant on surface area.

In the late 1800's Heinrich Hertz discussed the deformation of bodies in contact and solved the problem of two elastic curved bodies in contact. It was Bowden and Tabor in the 1930's and 1940's who began to discuss the deformation of curved surface asperities in contacting bodies building on Hertz's contact mechanics theory.⁶

In the 1950's they conducted experiments that showed friction is in fact dependent on real surface area given by the equation

$$F = \sigma A_r \quad (1.2)$$

where again F is the force of friction, σ is the shear stress, and A_r is the real area of contact.⁷ Thus friction is linearly dependant on real contact area. In 1957 Archard began to bridge the gap between the results of Da Vinci and Amonton by showing that on a macroscopic level with a multitude of asperities in the apparent contact area, the real contact area scales approximately linearly with normal load.⁸ In 1966 Greenwood and Williamson using a Gaussian distribution of asperity heights showed that the real area of contact can be approximated by

$$A_r \approx 3 \left(\frac{R}{\sigma} \right)^{\frac{1}{2}} \frac{N}{E_c} \quad (1.3)$$

where R is the average radius of curvature of the summits, σ the standard deviation of summit heights, N the loading force, and E_c the composite elastic modulus. Which all simply states that as the loading force between the two surfaces increases the tallest peaks deform and more and more of the peaks come into contact.⁹ If however the number of

asperities in the contact area becomes small or the normal load is low (resulting in contact pressure below the composite hardness of the contacting surfaces) the statistical approach to the contact mechanics falls apart and the real contact area will scale as either $N^{2/3}$ for spherical asperities or $N^{1/2}$ for cylindrical asperities following Hertz's general formulation.¹⁰ In these cases Bowden and Tabor's more fundamental equation still holds true.

1.2 Ploughing and Adhesive Friction

Another result of Bowden and Tabor's work was to separate the resistance to sliding (friction force) into two components: the adhesion term exerted at the interface of real contact defined by the shear stress in equation 1.2, and the ploughing (plowing) term which arises from the inelastic (plastic or viscoelastic) deformation of the surface asperities as they plough into one another. The ploughing term of friction can also arise from the dragging of a hard material through a softer material. The ploughing term at this point presents no real enigmas. It has been modeled using continuum theories of plasticity¹¹ or viscoelasticity¹². Moreover the experiments by Bowden and Tabor, even with soft ductile metals, showed that the adhesion term is the dominant one. This difference becomes even greater with hard materials such as diamond and is completely eliminated if the deformation of the solids, including surface asperities, is perfectly elastic or the surfaces are perfectly smooth. The elastic condition is met if the mean elastic contact pressure, N/A_r where N and A_r are defined above, is below 25% of the contacting material hardness.¹⁰ The adhesive term of friction is much more difficult to

theoretically predict and remains a major portion of fundamental tribological research.¹³ In general adhesion between dry surfaces results from a few fundamental forces: van der Waals, electrostatic, and hydrogen bonding. The van der Waals attraction results from the interaction between instantaneous dipole moments of atoms. For two flat parallel surfaces, and for separations less than 20 nm, the attractive force per unit area is given by

$$F = \frac{A}{6\pi d^3} \quad (1.4)$$

where A is the Hamaker constant which is determined by the particular interacting atoms) and d is the separation of the surfaces.¹⁴ Electrostatic forces can arise due to surface charge accumulation from the atmosphere. Also electrostatic attraction may also arise due to a difference in the work function of the approaching surfaces. The electrostatic force per unit area for two surfaces separated by an air gap can be given by

$$F = \frac{\epsilon_0 V^2}{2d^2} \quad (1.5)$$

where ϵ_0 is the permittivity of free space, V is the potential difference, and d is once again separation.¹⁵ Surfaces having a large number of hydroxyl groups can form strong hydrogen bonds as the separation between both surfaces becomes small and will dominate that of the above two forces around a separation of 10 Å.¹⁶ It must also be noted that adhesion may arise from covalent bond formation ie cold welding however once a covalent bond between the two surfaces has been established the question of the interfacial friction becomes one of shear properties of the material itself. Although it is difficult to use the above forces to predict the actual adhesive shear stress of any interface

it is evident that modification of the surface adhesive energies ie attractive potentials should have a profound impact on the friction force.

1.3 Atomic Lubrication

In general lubrication schemes used in macroscopic contacts are at best ineffective and at worst can cause the failure of nano- and microscale applications in particular microelectromechanical systems (MEMS), which will be discussed in the next section.¹⁷ Some very elegant approaches have been proposed to control friction in these systems. Orientation of surfaces in an atomically incommensurate fashion which leads to a continuous phase difference between successive atomic interactions has been shown to minimize friction in mica interfaces¹⁸ and has been shown to virtually eliminate it in graphite¹⁹. Reduction of normal forces and/or sliding speeds has also been proposed and shown experimentally to lead to an ultralow dissipation state. This is a result of a change in the atomic corrugation felt by the contact.²⁰ Another interesting approach to the mitigation of dissipation is the modulation of the normal force acting between two contacting bodies at well-defined frequencies corresponding to normal resonances of the combined system. This method has been shown to reduce friction below the detectable limit of an atomic force microscope.²¹ Although the results of these experiments are impressive they are difficult to apply in actual microsystem applications. Also these approaches were not tested on contacts representative of actual MEMS contact conditions. In fact most of the fundamental studies of atomic scale friction have been investigated by atomic force microscopes, surface forces apparatus, and quartz crystal microbalances of

which none represent actual MEMS contact conditions. Although all of these approaches lead to insight into atomic scale friction and lubrication it has been noted that measurements of friction between ostensibly similar smooth surfaces, using these different types of apparatus, could differ by orders of magnitude.²² Shear strengths measured by surface forces apparatus are tens of megapascal and AFM shear stresses are on the order of gigapascal. Shear stresses for microsystems tend fall in between these two values. Therefore any fundamental friction/lubrication studies with application to microsystems need to be conducted with actual MEMS devices. Some major questions in the fundamentals of lubrication in microsystems are first ones that arise from the manufacturing process and operation. Are covalently bonded self-assembled monolayers used in the microsystem fabrication process to lower surface energies (adhesion) robust enough to withstand the energies dissipated in sliding and normal contacting conditions, and if not how quickly do they degrade under each condition? Also what are the failure modes of microsystems? Finally a question that arises from theories of atomic lubrication with adsorbed species what is the impact of mobile adsorbed molecules on atomic-scale friction as it relates to microsystems.

Films are present at virtually all surfaces. They can be either adsorbed from the atmosphere as trace levels of contaminants or intentionally applied.^{23,24} These films are expected to have significant impacts. It has been predicted that mobile molecules in submonolayer coverages would increase friction by moving into positions that increase the adhesive friction force and lock the opposing surfaces together.²⁵ The superlubricity effects associated with incommensurate contacts as discussed above would be negated by

this mobility. It has been shown however that at the formation of a monolayer of adsorbed molecules is sufficient to drop the measured friction force in a variety of contacts that showed no effect from submonolayer coverages.^{26,27}

It is also possible however that the mobility of an adsorbed species could have a positive effect on friction. If in fact the presence of the molecules on the surface reduced interfacial adhesion then the mobility of the molecules would provide a mechanism of replenishment if they are worn away and not surrounded by a vapor. This becomes highly important in lubrication of microsystems with rubbing contacts in highly occluded areas where the partial pressure of a surrounding vapor approaches zero. Moreover the mobility of the adsorbed molecules may be an indication that they will in fact reduce surface adhesive forces. The mobility of submonolayer coverages of molecules is in principle governed by the mass of the molecule/atom, the temperature, and the energy barrier for diffusion (E_{diff}). At temperatures where $k_B T \gg E_{diff}$ the adsorbate acts as a 2D gas where individual surface potentials do not affect the adsorbate's motion. Although an adsorbate's mobility is highly dependent on the mass of the particles it is always dependent on the cluster size. As discussed earlier commensurate surfaces exhibit high frictional forces, along the same lines individual particles are easily trapped in individual potential wells on the surface.²⁸ As cluster size increases the particles are lifted out of the potential wells by adhesion to their neighbors and therefore are more free to move along the surface as a unit. In fact diffusion coefficients of gold islands (250 atoms) on a graphite surface have been observed to be 6 orders of magnitude larger than those compared to single atoms ($1000 \text{ cm}^2/\text{s}$ versus $0.002 \text{ cm}^2/\text{s}$).²⁹ For mobile alcohols on

microsystems diffusion rates of clusters have been calculated to be on the order of 1×10^{-8} m^2/s .³⁰ For a typical microsystem contact area of 1×10^{-15} m^2 and a reciprocating rate of 200Hz the cluster travels over an area of 5×10^{-11} m^2 virtually assuring that a cluster would be able to move into the contact area. The phenomena of a mobile surface adsorbate being worn away by a reciprocating contact moving too fast to return is known as the “windshield wiper” effect.³¹ Brenner et al developed a multiscale expression for effective liquid lubrication of reciprocating contacts by surface flow.³² The expression calculates the steady-state center concentration of a lubricated contact as a function of surface diffusion D , oscillation frequency f , contact area A_c , and two factors, A and B , associated with fraction of lubricant removed per cycle. The expression takes the form

$$C(S) = \frac{1}{e^{AS+B}} \quad (1.6)$$

where

$$S = \frac{fA_c}{D}. \quad (1.7)$$

Figure 1.1 shows center concentration as a function of the $\log(S)$ for 0.1% and 10% of the lubricant removed per cycle. Realistic values as stated above for microsystem removal rate parameters (fA_c) are 2×10^{-13} m^2/s . Therefore cluster self diffusion coefficients of 1×10^{-8} m^2/s are sufficient to refill the area scrapped free in one cycle.

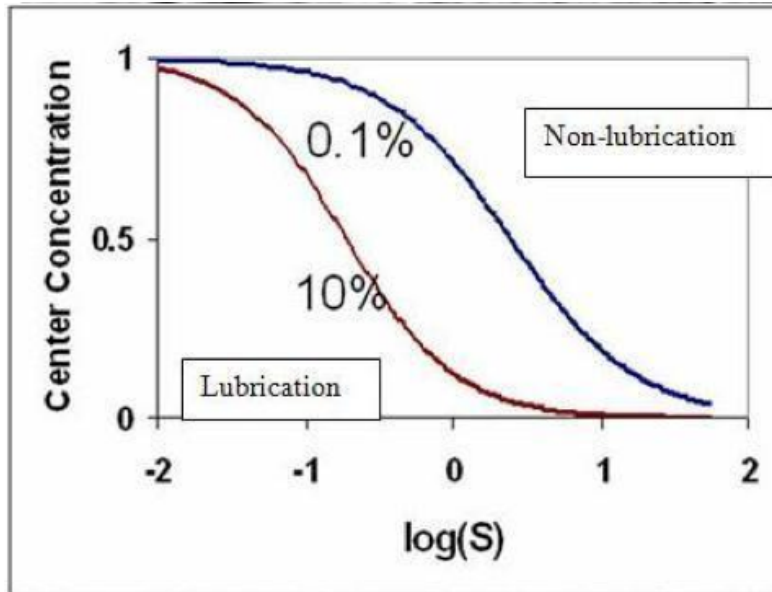


Figure 1.1 The lubricant steady-state concentration as a function of $\log(S)$ for 0.1% and 10% lubricant removed per cycle.³²

It would therefore be interesting to observe the impact of mobile and non-mobile molecules on friction in microsystems at monolayer and submonolayer levels. One last question that is more along the lines of sample preparation is how do we remove contaminants from MEMS structures? Are there differences in standard techniques of UV-Ozone and Oxygen plasma cleaning as it pertains to cleaning of microdevices with highly occluded areas?

References

- [1] D Dawson History of Tribology, Logman, London, 1979
- [2] BNJ Persson, Sliding Friction, Physical Principles and Applications 2000
- [3] H Peter Jost TLT March 2006 pp 24 – 29
- [4] G Amontons, Mem Acad Roy Sci 206 1699

- [5] CM Mate, Tribology on a Small Scale, Oxford, Oxford Press, 2008
- [6] FP Bowden and D Tabor, Proceedings of the Royal Society of London. Series A, Mathematical and Physical Sciences, 169(938) 1939
- [7] FP Bowden and D Tabor, Friction and lubrication of Solids, Part I, Oxford Press, Oxford 1954
- [8] JF Archard, Proceedings of the Royal Society of London. Series A, Mathematical and Physical Sciences, 243(1233) 1957
- [9] JA Greenwood and JBP Williamson, Proceedings of the Royal Society of London. Series A, Mathematical and Physical Sciences, 1966
- [10] NR Tas, C Gui, and M Elwenspoek, J Adhesion Sci Technol. Vol 17 No 4 2003
- [11] A Kapour, KL Johnson, and JA Williams. Wear 200 1996
- [12] JA Greenwood and D Tabor. Proc. Phys. Soc., 71, 1958
- [13] KL Johnson. Proc Instn Mech Engrs 214 part C 2000
- [14] JN Israelachvili. Intermolecular Surface Forces Academic London 1985
- [15] R Maboudian and R Howe J Vac Sci Technol. B 15(1) 1997
- [16] R Legtenberg, AC Tilmans, J Elders, and M Elwenspoek Sens and Actuators A 43 1994
- [17] J Krim Surface Science 500 2002
- [18] H Hirano, K Shinjo, R Kaneko, and Y Murata Phys Rev Lett 67 1991
- [19] M Dienwiebel et al. Phys Rev. Lett 92(12) 2004
- [20] A Socoliuc, R Bennewitz E Gnecco, and E Meyer Phys. Rev Lett 92(13) 2002
- [21] A Socoliuc et al Science 313 2006

- [22] J Krim *Scient. Am.* 275 1996
- [23] V panella, R Chiarello, and J Krim, *Phys. Rev Lett* 76 1996
- [24] KR Mecke and J Krim *Phys Rev B* 53 1996
- [25] G He, M H Muser, and M Robbins *Science* 284 1999
- [26] A Gellman *JS Ko Trib. Lett* 10 2001
- [27] D. Xu K Ravi-Chandar, and K Lietchi *Jour. Coll. Inter. Sci.* 318 2008
- [28] C.DeW Van Siclen, *Phys. Rev. Lett* 75, 1574 (1995)
- [29] S.C. Wang, G. Erlich, *Phys. Rev. Lett* 79, 3835 (1999)
- [30] B. P. Miller, J. Krim, *J. Low Temp. Phys.* 157, 252 (2009)
- [31] B. Borovsky, B.L. Mason, J. Krim, *J. Appl. Phys.* 88, 4017 (2000)
- [32] M. Abdelmaksoud, S.M. Lee, C.W. Padgett, D.L. Irving, D.W. Brenner, J. Krim. *Lang.* 22, 9606 (2006)

Chapter 2: MEMS

2.1 MEMS and their Applications

In 1959 Feynman in his lecture, *There's Plenty of Room at the Bottom*, predicted the invention and development of micro systems to scale down the larger and continually growing world. MicroElectro Mechanical Systems (MEMS) are the realization of this prediction. They are typically no larger than a grain of sand and act as the interface between the world of electrical signals and physical manipulation. This allows integration on an extremely small-scale mechanical motion and electronic elements on one chip. Applications are far reaching from the medical/biological fields, to the automotive industry, aeronautics, communication and defense.

The largest commercial applications to date are pressure sensors¹, accelerometers², and micromirror arrays³. These devices exhibit low power consumption, small size, and low cost manufacture. The automotive industry was one of the first major commercial industries to use MEMS in high volume units. The MEMS manifold absolute pressure (MAP) sensor was the first being brought to market in the early 1980's and the MEMS accelerometer was the second arriving in the early 1990's. Another growing area in commercial MEMS technology is Radio Frequency MEMS (rfMEMS). Studies are beginning to elucidate the mechanics of these devices⁴ and they are quickly becoming the state of the art technology for cell phones and other wireless technology devices. BioMEMS are becoming another important class of MEMS devices. They can

be used to detect specific ions and molecules, sense pressure within arteries, and help detect defective DNA in vivo.⁵

The use of these devices in actual commercial applications shows that the manufacturing technology has progressed out of the research phase. Meaning that design and application of devices is no longer limited by micromachining technology.

2.2 Micromachining

Micromachining of Silicon based MEMS devices can be broken up into two main technologies, *Bulk Micromachining* and *Surface Micromachining*.

Bulk micromachining is the oldest paradigm of silicon based MEMS. In this case the entire thickness of a silicon wafer is used for building the micromechanical structure. Bulk micromachining starts with a silicon wafer or other substrates, which is selectively etched, using photolithography to transfer a pattern from a mask to the surface. Bulk micromachining can be performed with wet or dry etches, and can be isotropic or anisotropic. Isotropic etchants remove silicon equally in all directions and is the simplest form of bulk micromachining. The most common etchant in this case is a mixture of hydrofluoric acid, nitric acid and acetic acid known as "HNA".⁶ This works in a process of oxidation of the silicon and reaction of the resulting silicon oxide with the hydrofluoric acid. This produces a soluble silicon compound, which is carried away from the surface. The anisotropic wet etch is used to create structures by taking advantage of the fact that silicon has a crystalline structure, which means its atoms are all arranged periodically in lines and planes. Certain planes have weaker bonds and are more susceptible to etching.

Thus the crystal etches much more quickly along those planes. Classic papers describing these anisotropic crystal plane dependant etches are Bean⁷ and Bassous⁸. The most widely used anisotropic wet etchants are the alkali hydroxide etchants such as KOH, NaOH. These reaction processes can be quite complicated and are still under some debate. However the generalized process can be found here.⁹ The etch results in pits that have angled walls, with the angle being a function of the crystal orientation of the substrate. This type of etching is inexpensive was the basis for early designs of MEMS accelerometers and pressure sensors and is still the most common etch in single crystal silicon. An example of the bulk etch process can be seen in figure 2.1. Here a boron implant prevents the etchant from clearing the bottom of the wafer creating a simple membrane. The bulk micromachining technique has a few drawbacks. Firstly it is difficult to integrate the bulk micromachining process into standard Complimentary Metal-Oxide-Semiconductor (CMOS) processes used for fabrication of integrated circuits, secondly the devices created have limited complexity with no moving parts, and thirdly the surface areas required for bulk micromachined pressure sensors, due to the sloped sidewalls of recesses made using anisotropic etchants, is much larger than the membrane area. This last drawback means that the yield per wafer is reduced over what could be obtained if the membrane size was the limiting factor. Surface micromachining was developed in the 1980's to address these shortcomings of the bulk process.

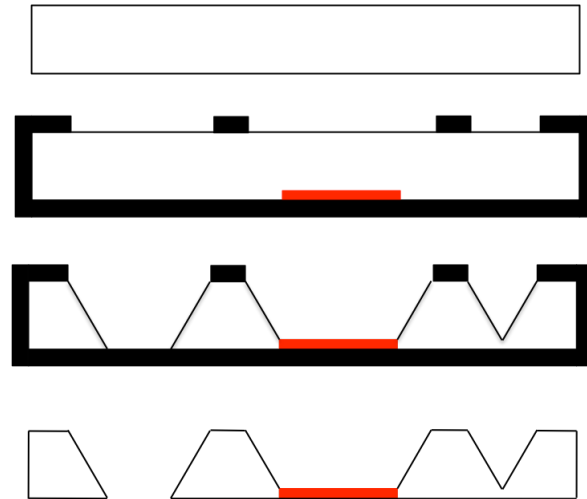


Figure 2.1 Bulk micromachining process for production of a hole, a membrane and a trough in a silicon wafer.

Surface micromachining takes place on the surface of a silicon wafer where films used for structures are deposited using techniques such as low pressure chemical vapor deposition (LPCVD). These structures can be made with several deposited layers and the parts can be “released” to allow them to move laterally as well as vertically making MEMS actuators (MEMS devices with moving parts) possible.¹⁰ The surface micromachining technique follows the CMOS technology leading to easy integration creating monolithic microsystems in which the electronic and mechanical components are built onto the same substrate. There are two key process steps in surface micromachining. The first is the deposition of low stress thin films that can be used for structural elements and the second is the deposition of sacrificial layers that can be removed to allow the structural layer to be detached from the substrate. Polysilicon is commonly used as the structural layer although other materials such as gold and aluminum have been developed as structural layers for MEMS. Polysilicon (polycrystalline silicon) is composed of many

small silicon crystals (grains) randomly oriented throughout the material. Through careful deposition processes it can be deposited with well-controlled, repeatable film stress which is a necessity in surface micromachined devices.¹¹ The high aspect ratio structures possible in surface micromachining (long and thin) mean that uncontrolled film stresses will deflect the structures and make them useless. Polysilicon itself is nonconductive and therefore needs to be doped to be used in devices that need to be actuated.

The second key step for surface micromachining is the use of a sacrificial layer that can be removed to release the structural layer and allow motion.¹² A variety of materials have been used as sacrificial layers in surface micromachining such as photoresist and metals such as aluminum. However when it comes to devices made from polysilicon, silicon dioxide (SiO_2) is preferred because it can better withstand the high temperatures required of LPCVD deposition of polysilicon approximately 600°C ¹³. The key to any sacrificial layer is that it must be able to be preferentially etched with respect to the structural layer. Hydrofluoric acid is generally used as the release etchant in polysilicon based MEMS devices due to its high etch rate of SiO_2 compared to that of the structural polysilicon. Figure 2.2 describes the process of creating a cantilever beam on top of a silicon wafer. The first step is the deposition of a silicon dioxide layer onto the top of the wafer. A mask is placed onto the top of the wafer and the uncovered SiO_2 is removed with a process known as reactive ion etching (RIE). RIE is a combination of physical and chemical processes. Here a plasma is exposed to the surface at low pressure. The reactive species react with the material only when the surface is activated by the collision of incident ions from the plasma (e.g., by breaking bonds at the surface). The directionality

of the ion's velocity produces much more collisions on the horizontal surfaces than on the walls, thus generating faster etching rates in the vertical direction. The typical chemistries used in etching of SiO_2 are plasmas of CF_4/H_2 , C_2F_6 , C_3F_8 and CHF_3/O_2 . Typical etch chemistries used for polysilicon are plasmas of CF_4/O_2 , CF_2Cl_2 , CF_3Cl , and $\text{SF}_6/\text{O}_2/\text{Cl}_2$ although many more chemistries have been developed.¹⁴ After the exposed SiO_2 has been etched a layer of doped polysilicon is deposited. A mask is then placed onto the polysilicon layer and the exposed polysilicon is removed. Finally the sacrificial SiO_2 layer is removed by immersion in HF leaving a freestanding cantilever. The HF is then removed in a final rinse step in H_2O . This final release and rinse step that was a major hurdle in the mass production of surface micromachined MEMS actuators.

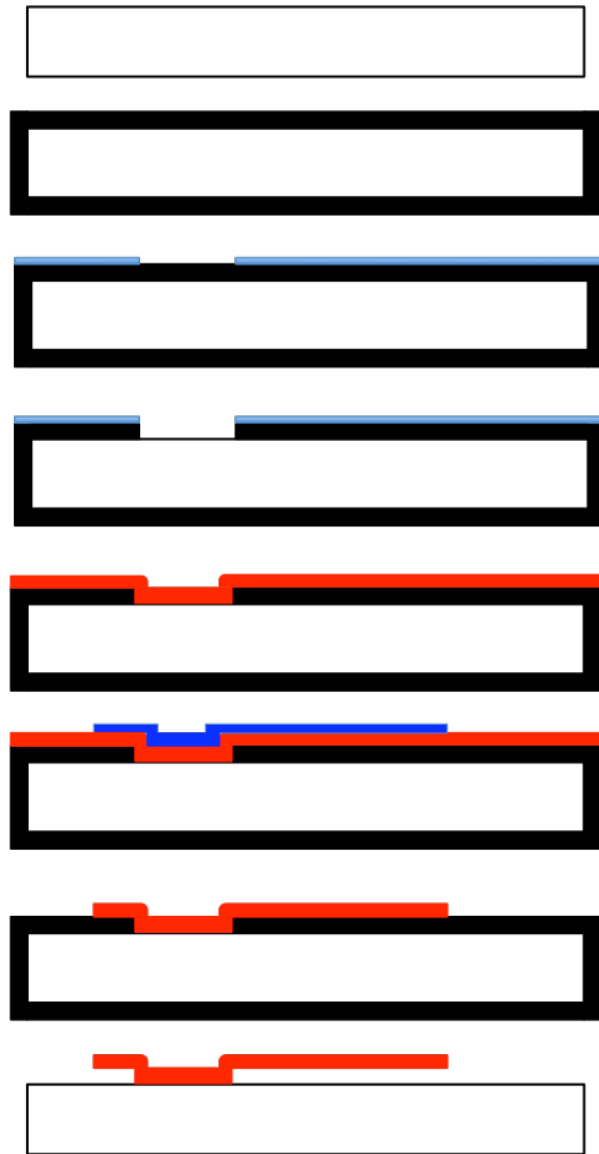


Figure 2.2 Surface micromachining process for production of a long polysilicon cantilever on top of a silicon wafer.

2.3 Release Related Stiction

After performing a sacrificial etch, surface tension of the liquid etchant or final rinse can cause a phenomena known as release related stiction. As the etchant removes the sacrificial material it fills the space left between the structure and the substrate. The etchant is then replaced with an inactive rinse usually H₂O. As polysilicon is hydrophilic

water wets the surface readily and completely displaces all of the etchant material. This hydrophilic wetting creates capillaries as the water evaporates. As the volume of the fluid decreases, the surface tension acts to pull the polysilicon and the underlying silicon substrate together.^{15,16} Since, dimensionally, area depends upon L^2 and volume depends upon L^3 volume decreases more quickly than surface area. Therefore as MEMS devices get smaller and smaller the ratio of surface area to volume increases. This increasing surface area to volume ratio creates highly compliant structures that do not possess the necessary spring constant to overcome the capillary force and the structures deflect towards the surface and permanently adhere. This adhesion of the structural layer to the substrate is known as release related stiction. An illustration of this process is shown in figure 2.3

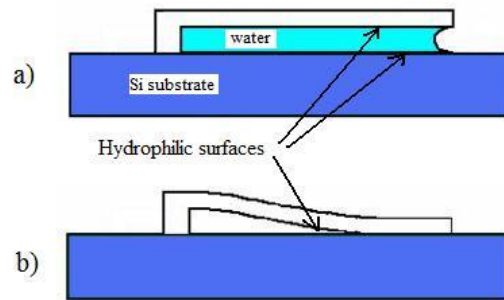


Figure 2.3 Visualization of release related stiction due to capillary forces of a trapped volume of water underneath a compliant cantilever.

There are several ways to prevent this release related stiction. The first is the use of dry or vapor phase etchants such as a mix of HF/Methanol or plasmas of fluorine based molecules.¹⁷ In the case of vapor phase release condensation and capillary adhesion is still possible and the etch rate is much slower than in the wet release. Many of the

plasma etch processes use fluorine containing gases or gas mixtures. These fluorine atoms produced by the plasmas form the main reactants to perform isotropic etching. But the ions and molecular radicals produced by the plasma environment can adversely affect the substrate in some device applications. The second method is to use low surface tension solvents as the final rinse step to reduce the capillary force. The techniques generally involve a final methanol rinse and rapid evaporation of the methanol on a hotplate. This method has shown some success in devices with lower compliance however it is not optimal nor is it reliable. A third method is to affect geometric modifications to the underside of the structures to lower the surface area that can come in contact with the substrate. This can be accomplished by the addition of dimples to the bottom of a cantilever. This technique has shown to be a good addition to most device designs however it alone is still not enough to reliably prevent release related stiction. The fourth technique involves removing the capillary by supercritical drying or by freezing and then sublimating the rinse solution. The major drawback to freeze-drying techniques is the sometimes large volume change of the rinse solution. This large volume change can cause stress in the structural material causing device destruction.¹⁸ Supercritical CO₂ drying has had significant success in the overall reduction of release related stiction. After devices have been rinsed in methanol to remove the release etchant they are exposed to liquid CO₂ in a pressurized chamber, which displaces the methanol. The CO₂ is then brought through its critical point to remove the capillary. Finally the chamber is depressurized and freestanding structures remain.¹⁹ The only drawback to this technique is that it leaves the device surfaces exposed to the environment and therefore

water vapor in the atmosphere can adsorb onto the surface and eventually result in device adhesion (dormancy related stiction). The fifth and by far the most successful solution to release related and dormancy related stiction is the deposition of self-assembled monolayers (SAMs) or organic thin films directly after the release process prior to rinsing or after a supercritical drying step. This deposition reduces the surface energy and virtually eliminates the capillary forces.²⁰ A number of well-known hydrophobic SAMs have been grown on Si surfaces with good results. They create ordered monolayers with low surface energies due to their tight packing and either methyl or trifluoromethyl termination. SAMs of alkylchlorosilanes, alkylalkoxysilanes, and alkylaminosilanes require hydroxylated substrates for their formation. The *in-situ* formation of polysiloxane, which is connected to the surface silanol groups (-SiOH) via Si-O-Si bonds, is the driving force for self-assembly. This procedure first involves the replacement of the aqueous rinse solution with an organic solvent through a series of steps. The devices are then placed in a mixer of the monolayer precursor and solvent. The solvent is then replaced by water through a series of reverse dilution steps. Since these silanized surfaces have a water contact angle of approximately 114°, rendering the surface hydrophobic, the surface tension of the water causes it to recede from the surface resulting in a dry sample. Perfluorinated alkyltrichlorosilanes and alkylaminosilane SAMs formed using perfluorodecyl trichlorosilane (FDTS) and tridecafluorotris(dimethylamino)silane (FOTAS), have been shown to have better thermal stability compared to longer chain hydrocarbon based chlorosilanes such as octadecyltrichlorosilane (OTS).²¹ These SAMs have also been successfully deposited in

the vapor phase, which is more compatible to assembly line type processes and better integrated into the CMOS process.²² The application of self-assembled monolayers mixed with the use of dimples and supercritical drying has almost completely eliminated the release and dormancy related stiction issue in the production of MEMS devices. However devices with actuated rubbing parts are still being plagued by failures due to friction between the rubbing contacts. The chemically attached self-assembled monolayers are still subject to wear through rubbing and will eventually wear away.

2.4 Summary and Research Objectives

The application of many moving structures is now limited by friction and adhesive forces. The miniaturization that makes these devices so useful also has drawbacks. As structures are made smaller and smaller the surface area to volume ratio increases. Thus forces that depend on surface area like adhesion become more and more important the smaller you go. Frictional forces generated at these interfaces have been the major limiting factor in the development of high stress contacts such as micromotors and microturbines²³. The high surface area to volume ratio of these devices can cause the surface forces to be orders of magnitude larger than the available inertial forces thus immobilizing the interfaces causing the devices to fail. The application of self-assembled monolayers and techniques to reduce surface area has proved valuable in the reliable production of MEMS devices however the wear rate of these layers under mechanical stress has never been documented and related to the energies dissipated in sliding and normal contacting conditions. Furthermore elucidation of failure regimes in rubbing

devices has also been lacking and will answer the question of what specific conditions lubricants must prevent. Lastly the application of bound plus mobile phase lubricants and vapor phase lubrication have been the cutting edge of device development in the past 10 years however the actual mechanisms of this lubrication or whether there is a correlation to adsorbate mobility are still not currently understand. This dissertation is structured to address these issues by developing a specialized ultra clean environment for device testing, a methodology for assessing device performance and friction measurement, adsorbing molecules with differing surface mobility to address it's role in MEMS lubrication, and developing cleaning techniques to assure surface reliability.

References

- [1] WP Eaton Smart Mater. Struct. 6 1997
- [2] N Yadzi, F Ayazi, and K Najafi Proc. of the IEEE Vol 86(8) 1998
- [3] LJ Hornbeck, MRS Bull. 26 2001
- [4] C Brown, PhD Thesis, North Carolina State University 2008
- [5] DL Polla et al. Annu. Rev. Biomed. Eng 2 2000
- [6] H Robbins and B Schwartz J. Electrochem. Soc. 107(2) 1960
- [7] KE Bean IEEE Trans Elec Devices ED-25(10) 1978
- [8] E Bassous IEEE Trans Elec Devices ED-25(10) 1978
- [9] H Seidel, L Csepregi, and A Heuberger J. Electrochemi. Soc. 137(11) 1990
- [10] RW Johnstone and M. Parameswaran An Introduction to Surface-Micromachining, Kluwer Academic 2004
- [11] JM Bustillo, RT Howe, and RS Muller Proc. IEEE 86(8) 1998

- [12] SA Campbell The Science and Engineering of Microelectronic Fabrication Oxford University Press, USA 2001
- [13] PJ French and AGR Evans Electron. Lett. 22(13) 1986
- [14] B Bhushan ed. Springer Handbook of Nanotechnology Springer New York 2003
- [15] N Tas, T Sonnenberg, H Jansen, R Legtenberg, and M Elwenspoek J. Micromech. Microeng. 6 1996
- [16] R Maboudian and R Howe J Vac Sci Technol. B 15(1) 1997
- [17] Y Lee et al. JMEMS 6(3) 1997
- [18] N Takeshima et al Tech. Dig. Int. Conf. Solid-State Sensors and Actuators(Transducers '91) 1991
- [19] I Jafri, H Busta, and S Walsh SPIE Conf Vol 3880 1999
- [20] R Maboudian, WR Ashurst, and C Carraro Sens Act. 82 2000
- [21] U Srinivasan, MR Houston, RT Howe, and R Maboudian JMEMS 7 1998
- [22] YX Zhuang et al JMEMS 16(6) 2007
- [23] N Savoulides PhD Thesis Massachusetts Institute of Technology 2004

Chapter 3: Experimental

In this chapter I will give a thorough description of the experimental test set-up at North Carolina State University, a description of the device layout, the procedure for controlling the devices, and the data taking procedures for both the failure measurements and the ringdown measurements .

3.1 Ultra-High Vacuum (UHV) Experimental Chamber and MEMS Mount Description

A schematic of the experimental chamber is shown in figure 3.1. The components of the stainless steel chamber consist mostly of UHV compatible materials however the vacuum seals on the mount holding the MEMS chip in the chamber and the two capacitance manometer connections are made with viton o-rings which are only capable of 1×10^{-9} Torr. Therefore the minimum pressure capable with the current set-up is 1×10^{-9} Torr. Conversion to conflat type connections would change the chamber to true UHV ie $< 1 \times 10^{-9}$ Torr. Vibration isolation, when required, was established by hanging the chamber from a steel support by bungee cords. However for the measurement techniques used in this thesis vibration isolation was not a concern so the chamber was rested on blocks to prevent degradation of the bungee system. Low pressure is established via three pumps. For roughing the system to approximately 1×10^{-3} Torr a dry mechanical pump is used which is connected to the chamber through a turbomolecular pump. Once one millitorr is established the turbomolecular pump is used to reach 1×10^{-6} Torr at which time a valve to the ion pump can be opened to bring the chamber (with vacuum baking) to an ultimate pressure of 1×10^{-9} Torr. The chamber is outfitted with a residual gas

analyzer to determine the constituent molecules floating in the chamber. This provides a leak detection mechanism as well as a way to ensure the chamber has no hysteresis from experiment to experiment, i.e. no residual hydro/fluorocarbons. The chamber is outfitted with two Baratron capacitance manometers capable of pressure measurements in a range of $1000 - 1 \times 10^{-3}$ Torr and a cold-cathode gauge with a range of $1 \times 10^{-3} - 1 \times 10^{-10}$ Torr. The chamber is fitted with multiple feedthroughs to allow independent filling of the chamber with test lubricants or ultra-pure nitrogen gas. A quartz-crystal microbalance is used to monitor and approximate the uptake of test lubricants onto the MEMS chip. The top of the chamber is fitted with a glass viewport so that a long focal length microscope/CCD camera combination can be used to monitor the MEMS device as it is operated. Finally the chamber is outfitted with two separate electrical feedthroughs for operation of the devices and capacitive ringdown measurements. The ringdown connections are made via coaxial cables directly to the chamber to completely eliminate electrical noise generated outside of the chamber. The control connections are made with a multistrand cable to a BNC connection control box since electrical noise voltage variations are negligible when compared to drive voltages.

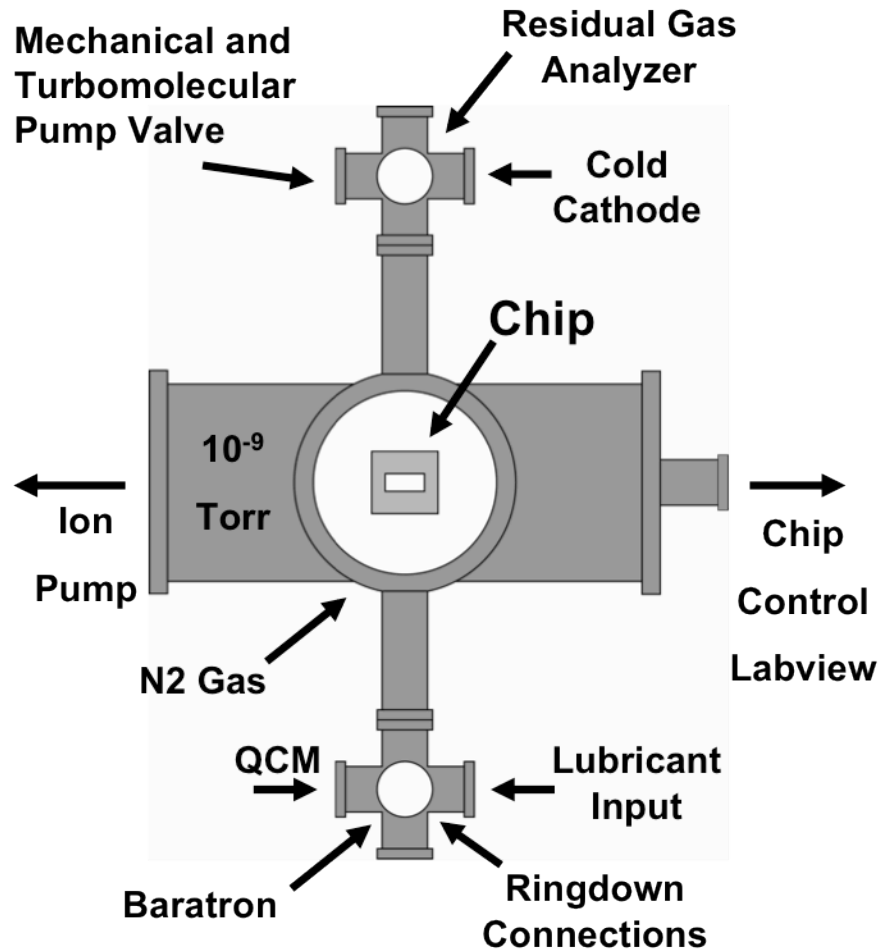


Figure 3.1. Schematic description of the experimental set-up with the constituent connections.

The MEMS chips are mounted in 24 pin gold ceramic dual inline packages from Kyocera. A bonding schematic is shown in figure 3.2 for the RS594 MEMS chip. This is the device design used in all of the experiments conducted at NCSU in this thesis. The devices are mounted and wirebonded at Advotech via thermally/electrically conductive epoxy and aluminum wedge wirebonding. The chips are pressed into the chip holder in

the chamber with a face-plate and electrical connections to the chip are made with spring topped posts. However damage to the springs over time has necessitated the use of copper grains to fill in the gaps and maintain electrical connection.

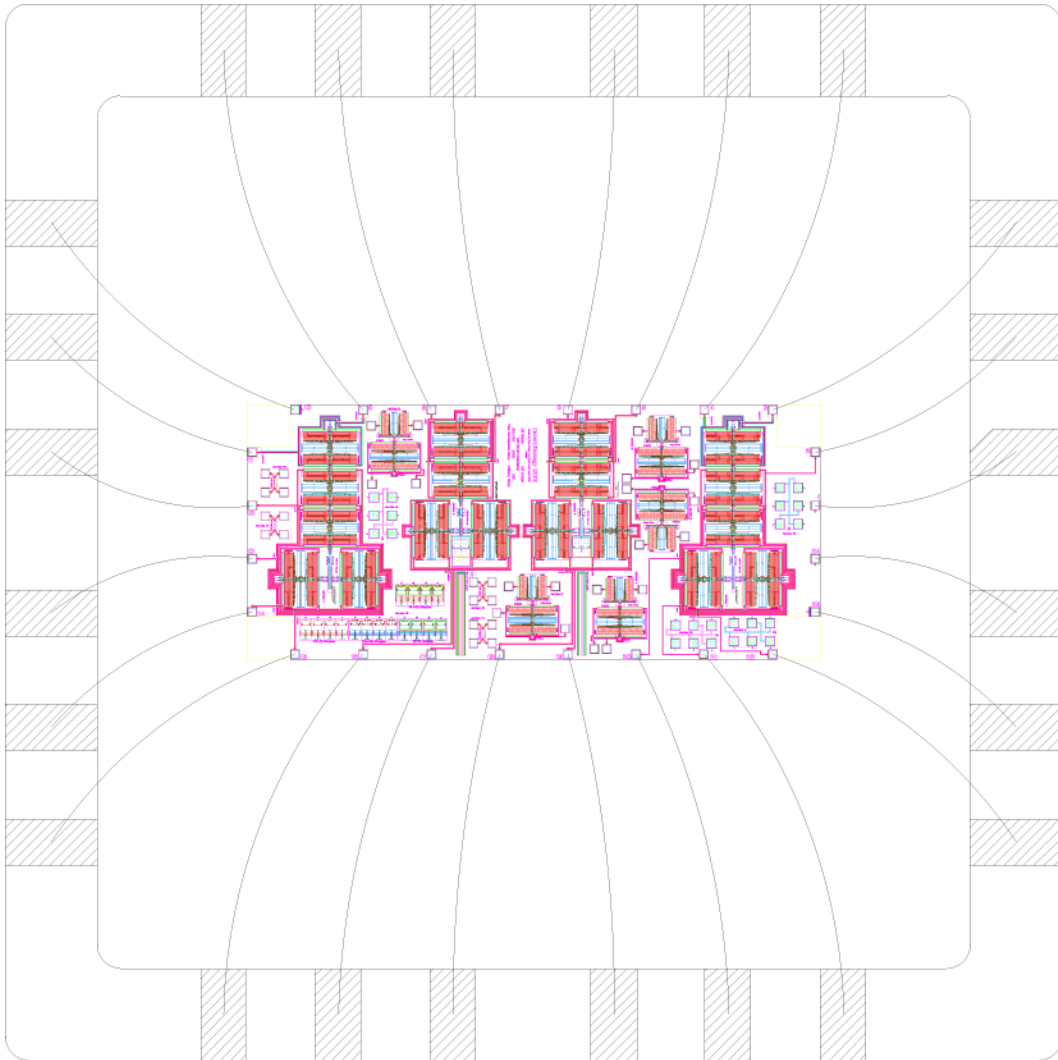


Figure 3.2. Bonding diagram of chip RS594 in 24 pin Kyocera package. Pin 1 begins as the notched rectangle and increases counterclockwise to pin 24.

3.2 RS594 Chip Layout and Force Constants

The RS594 MEMS Tribometer chip designed by Michael T Dugger and D. Adam Hook consists of 4 large pinch type capacitively driven MEMS tribometers and multiple other structures shown in figure 3.3. The pinch type tribometers will from now on be referred to as Devices 1-4 and are controlled by the bond pads on the periphery of the chip and are the only devices wired to the Kyocera package. Devices 1 and 4 have an extra bank of combs specifically designed for the capacitive ringdown friction measurement briefly described in Chapter 6 supplemental material. The capacitive drive technique for applying drive and pinch forces to these devices has been thoroughly described earlier in this thesis however the RS594 chip layout has not specifically been addressed. Two things should be addressed about RS594. The first is that pads 1 and 24 are unused and two is that there is an error in the design of device 1. The connection from bond pad #3 to the comb drive was unintentionally connected to the shielding above it and therefore is permanently grounded and unusable. The grounding planes and all shuttles are connected to pins #10 and #23. A full bondpad/pin layout for each device is presented as Table 3.1-3.4. All of the purposes included in the following tables refer to directions on figure 3.3; push moves the main shuttle to the left, pull moves the main shuttle to the right, load pinches the load posts into the main shuttle (moving the top load shuttle down and the bottom load shuttle up) and unload moves the load shuttles away from the main shuttle (reversing the directions described for load). For the capacitive sense pads sense B refers to the comb bank to the far left of the device and sense A refers to the comb bank directly to the right of that. There really is no difference in using sense

A or B for the ringdown measurements other than the current flow is exactly opposite when sense A is biased versus sense B for the same measurement conditions. For reference, whenever a voltage is applied to a particular group of combs the shuttle moves TOWARDS that group, ALWAYS, regardless of whether the applied voltage is positive or negative. This can be seen mathematically in equations 6.6 and 6.7 where the force is always positive.

Table 3.1 Device 1 Bond Pad / Wired Pin Layout

Device 1 Pad/Wired-Pin #	Purpose
Pin #2	Push
Pin #3	Grounded/Unused
Pin #4	Capacitive Sense A
Pin #20	Pull
Pin #21	Load
Pin #22	Unload

Table 3.2 Device 2 Bond Pad / Wired Pin Layout

Device 2 Pad/Wired-Pin #	Purpose
Pin #5	Pull
Pin #6	Push
Pin #18	Unload
Pin #19	Load

Table 3.3 Device 3 Bond Pad / Wired Pin Layout

Device 3 Pad/Wired-Pin #	Purpose
Pin #7	Pull
Pin #8	Push
Pin #16	Unload
Pin #17	Load

Table 3.4 Device 4 Bond Pad / Wired Pin Layout

Device 4 Pad/Wired-Pin #	Purpose
Pin #9	Capacitive Sense B
Pin #11	Capacitive Sense A
Pin #12	Push
Pin #13	Pull
Pin #14	Load
Pin #15	Unload

The force constants described in equations 6.6 – 5.9 are listed in table 3.5 for devices 1 through 4. As you will notice the spring constants for the main shuttle of devices 2 and 3 are 2/3 that of devices 1 and 4. That is because devices 1 and 4 have one more identical set of folded springs on the main shuttle than that of devices 2 and 4. Also devices 1 and 3 have a extra column for sense capacitance which will be used in the ringdown measurement analysis.

Table 3.5 Force constants for the RS594 Chip subscripts correspond to the main shuttle (m) and the load shuttle (l).

	Device 1 and 4	Device 2 and 3
C_m	$6.725 \times 10^{-9} \text{ F/m}$	$6.725 \times 10^{-9} \text{ F/m}$
C_l	$3.363 \times 10^{-9} \text{ F/m}$	$3.363 \times 10^{-9} \text{ F/m}$
k_m	0.384 N/m	0.256 N/m
k_l	0.128 N/m	0.128 N/m
C Sense A and B	$3.363 \times 10^{-9} \text{ F/m}$	-

3.3 Device Control Electronics

All devices 1-4 on RS594 require 4 voltage connections to operate properly, push, pull, load, and unload. Devices 1 and 4 require an additional 2 connection for sense a and b. For the purposes of the drive electronics and connections however they do not matter. In device operation however they must either have a constant voltage (for ringdown) or be grounded (for failure measurements). The experimental set-up has a dual output GPIB controllable high voltage power supply, a national instruments data acquisition (NI-DAQ) card with two 0 – 10V analog outputs, an arbitrary function generator, and a dual input/output 50 gain voltage amplifier. Only one of the NI-DAQ card analog outputs is low noise therefore it is used to control the device. The voltage from the function generator is sent to the 50 gain voltage amplifier and from there to the device. The voltage from the NI-DAQ card is run through an ultra low noise unity gain operational amplifier and that output is run to the device. The purpose of the unity gain amplifier is to supply the necessary current required by the 50 gain voltage amplifier since it exceeds the NI-DAQ current limit. Each individual measurement technique requires a different device connection configuration however in general two voltage supplies are for static offsets and two are for device control. The necessity to amplify the output voltages of the NI-DAQ and the arbitrary waveform generator requires a precise measurement of the gain of the amplifier and any voltage offset. Therefore at the beginning of each day once the equipment has been turned on and given an opportunity to warm up a plot of the output of the high voltage amplifier versus requested NI-DAQ voltage is constructed from -1 – 1 V manually by stepping the NI-DAQ voltage in Measurement and

Automation explorer (MAX). The slope and intercept can then be entered into the labview program for ringdown measurements. For failure measurements the NI-DAQ output is used for static offset and is controlled manually via MAX so the slope and intercept are used to calculate the true output voltage. Second a plot of the high voltage amplifier versus waveform generator voltage is constructed from -1 – 1V DC voltage. No dc offset voltage has ever been seen here and the gain is always 49.99 however this is always tested for completeness.

3.4 Ringdown and Failure Test Set-Up and Control Software Description

Figure 3.4 shows a schematic representation of the two measurement techniques used at NCSU.

Dual Measurement Techniques

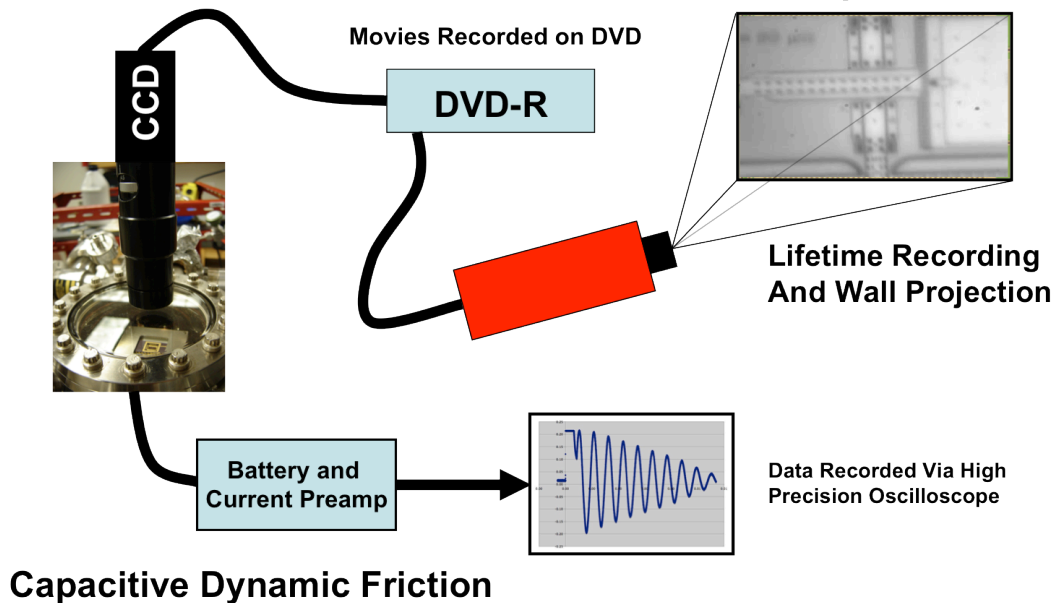


Figure 3.4. Schematic description of the device lifetime and ringdown measurement techniques.

The device failure/lifetime measurement technique consists of a microscope/CCD camera, a DVD recorder and a projector. The device is observed through the microscope and the output of the CCD camera goes to the DVD recorder. The external output of the DVD recorder is then sent to a projector for observation. Oscillation amplitude of the devices is controlled by the arbitrary waveform generator which is connected to either the push or pull connector for the test device. If a sine wave is used it should be noted that since the force equation contains V^2 and that is related to linearly to displacement, equations 5.9 and 5.10 the actual oscillation frequency is twice what the waveform generator reads and the motion of the device is from $x = 0$ to some maximum and back not $+x - x$ depending on the amplitude of the sine wave. However to limit the vertical

motion due to levitation forces a static 20 volts is applied opposite that of the waveform generator i.e. if the waveform is applied to the push connector then the DC voltage is applied to the pull. The equation for the position of the main shuttle if observed as in figure 3.3 with negative x being to the left is then

$$x = -\frac{C_m}{2k_m} \left((A_0 \sin(2\pi ft))^2 - 20^2 \right) \quad (3.1)$$

where A_0 is the amplified sine wave amplitude, f is the oscillation frequency, t is time, and the other components are those described in chapter 5 supplementary material for equations 5.9 and 5.10. The drive voltage amplitude is then chosen so that the oscillation amplitude is even around $x = 0$. A higher DC voltage can be chosen for higher drive amplitudes. To connect the waveform generator to the device without applying a large impulse to the device the waveform generator is set to its lowest frequency and drive amplitude. After connection the amplitude is slowly increased to the desired level and then the frequency is increased. A Labview program is used to control the load and unload shuttle. The program controls the dual output high voltage power supply. A 20 volt DC offset is used on the unload pin connected to output 2 on the power supply. Output 1 is connected to the load pin and the Labview program ramps that voltage from 20 to the desired load voltage. Once the experiment is finished a button is clicked and it goes from the load voltage to 0 volts to completely pull the load shuttle out of contact with the oscillating shuttle. If the loading posts are still in contact with the oscillating shuttle the program increases the unload voltage until the user stops the sequence or the power supply reaches 60 volts. At that point the program returns the unload voltage to 20 volts then returns the load voltage to 20 volts. For experiments with failure times on the

order of seconds to a few hours the DVD recorder is used in normal recording mode, continuously. For longer failure measurements the recorder is set up to intermittently record clips so that more than the standard maximum continuous DVD recording time can be covered with one dvd with a minimal error in oscillation number. A possible sequence could be one minute recordings every 10 minutes etc.

The capacitive ringdown technique consists of a standard 9V battery with the positive side connected to one of the sense comes of either device 1 or device 4. The negative side is connected through a current preamplifier to ground. The output of the current preamplifier is connected to a high-resolution digital oscilloscope. A labview program controls the voltages to the device and also controls the digital oscilloscope. The general process for the technique follows thusly. First the program initializes the oscilloscope sets the trigger level, the number of averages the oscilloscope goes through before generating an output and initializes the waveform generator setting it to dc mode. It then pulls/pushes the main shuttle to a set distance by applying a positive voltage to either the pull or push shuttle. Next it applies a voltage to the load shuttles through the waveform generator. It finally drops the voltage on the main shuttle. The voltage drop triggers the digital oscilloscope and it records the output of the current preamp. Finally the program reduces the voltage on the loading shuttle. It repeats this process corresponding to the number of averages to which the oscilloscope is set. Next it runs through the whole process again through initialization through all of the averages with a negative voltage applied to the main shuttle. The two generated ringdown averages are then averaged together once more. This gets rid of any crosstalk error generated by the

negative/positive drop in voltage. If no levitation compensation is used the output of the ringdown technique will have a vertical oscillation signal out top of the horizontal ringdown signal. This signal can be significant in vacuum however is damped out when in an atmosphere of gas. To diminish this signal the comb drive opposite the pull/push comb drive, whichever is used to move main shuttle for ringdown, is given a static voltage of 20 V and the output of the ringdown pulse drops from its maximum voltage to 20 V when conducting a ringdown measurement. To keep the load shuttle at the same height as the main shuttle a static 20 V is applied to the unload combs and the load voltage goes from 20 voltage to maximum load and then returns to 20 volts. The program does not control these two voltages however so they must be manually applied with the high voltage power supply. The trigger on the oscilloscope is controlled by the output of the DAQ card prior to being amplified and sent to the device therefore the signal is split after the unity gain operational amplifier with one side going to the 50 gain amplifier then to either the push or pull combs and the other going to the oscilloscope. The gain of the current preamplifier is set to 20×10^{-9} Amps/Volt (the real gain is 20.9239×10^{-9} Amps/Volt), which provides a high signal to noise ratio with little variation in gain between signals of 1775 and 1825 Hz which is the general resonant frequency of devices 1-4. An example of how the device can be connected for ringdown measurements follows: Pin #9 connected to battery, Pin #10 grounded, Pin #12 50 gain amplifier output corresponding to the DAQ card, Pin #13 20V from output 1 of the high voltage power supply, Pin #14 connected to 50 gain amplifier output corresponding to waveform generator, and finally Pin #15 20 V from output 2 of the high voltage power supply. To

process the output of the oscilloscope and generate a coefficient of kinetic friction a Mathematica program was written which has the capability of either fitting the peaks of the ringdown signal or fitting the entire signal. Prior to fitting however the gas-damping coefficient must be known. Therefore when the pressure in the chamber is increased prior to a contact ringdown experiment a noncontact ringdown experiment must be conducted. This is done simply by setting the load voltage in the labview program to the levitation voltage i.e. 20 volts and conducting the experiment as you would a contact ringdown measurement.

Chapter 4

Tribological Degradation of Fluorocarbon Coated Silicon Microdevice Surfaces in Normal and Sliding Contact

D. Adam Hook, Shannon J. Timpe, Michael T. Dugger and Jacqueline Krim

Article Published: Journal of Applied Physics Vol. 104 2008

Abstract - Reported here is a study of the tribological degradation of the contact interface of a fluorocarbon monolayer-coated polycrystalline silicon microdevice. A surface micromachined silicon tribometer is employed to track changes in the adhesion and friction properties during repetitive normal and sliding contacts. Evidence for tribological degradation commences immediately for parallel sliding contact motion, and is slightly delayed in the case of repetitive impact loading normal to the surface. The observed changes in interfacial behavior indicate dramatic changes in the chemical (i.e., surface energy) and physical (i.e., roughness, real contact area, etc.) nature of the contacting surfaces. Results from microscale sliding and impact experiments are interpreted in light of the primary physical and chemical degradation mechanisms of monolayer-coated silicon microdevices.

4.1 Introduction

Microelectromechanical Systems (MEMS) represent an emerging technology that relies on the microfabrication of small-scale mechanical components (gears, latches, mirrors, etc.) and the integration of those components with on-board actuators. From microgears to radio frequency microswitches, some of the most exciting, but unrealized applications of mechanical micromachined devices involve surfaces in sliding or impact contact. In addition, materials processing constraints frequently result in the fabrication of mechanical contacts between similar materials with high surface energies. These characteristics, combined with high surface area to volume ratios, make MEMS devices highly susceptible to the detrimental effects of surface forces including liquid capillary and van der Waals forces. Therefore, the tribological forces of adhesion and friction at this scale become comparable to, or even larger, than forces arising from gravity, inertia, or on-chip actuators.¹⁻⁴

One of the most common methods to mitigate the detrimental effects of these relatively high tribological forces is the application of monolayer coatings. The application of self-assembled or vapor deposited monolayers has become routine for reduction of tribological forces and a number of surface treatments have met with varying degrees of success for alleviation of MEMS contact issues. However, the wear attributes and durability of surfaces in sliding or intermittent contact remains problematic and physical and chemical degradation mechanisms at the contact interface can significantly reduce the effectiveness of such coatings.⁵⁻⁷ Tribological issues have thus emerged as the limiting factors in the development and commercialization of a wide variety of MEMS

devices, with surface treatments being the weakest link in overall system reliability and performance.

The current research focuses on the chemical and mechanical durability of the contact interface of a microdevice coated with a chemisorbed monolayer [FOTAS, tridecafluorotris(dimethylamino)silane, $\text{CF}_3(\text{CF}_2)_5(\text{CH}_2)_2\text{Si}(\text{N}(\text{CH}_3)_2)_3$]. Repetitive contact is investigated using a MEMS diagnostic structure designed to quantify normal and lateral forces. Degradation is examined in both normal (no gross sliding) and sliding repetitive contacts on MEMS sidewall surfaces. Both types of contacts are of importance for understanding and extending device lifetimes for systems that involve mechanical contact.

4.2 Experimental

4.2.1 MEMS Tribometer Fabrication and Monolayer Treatment

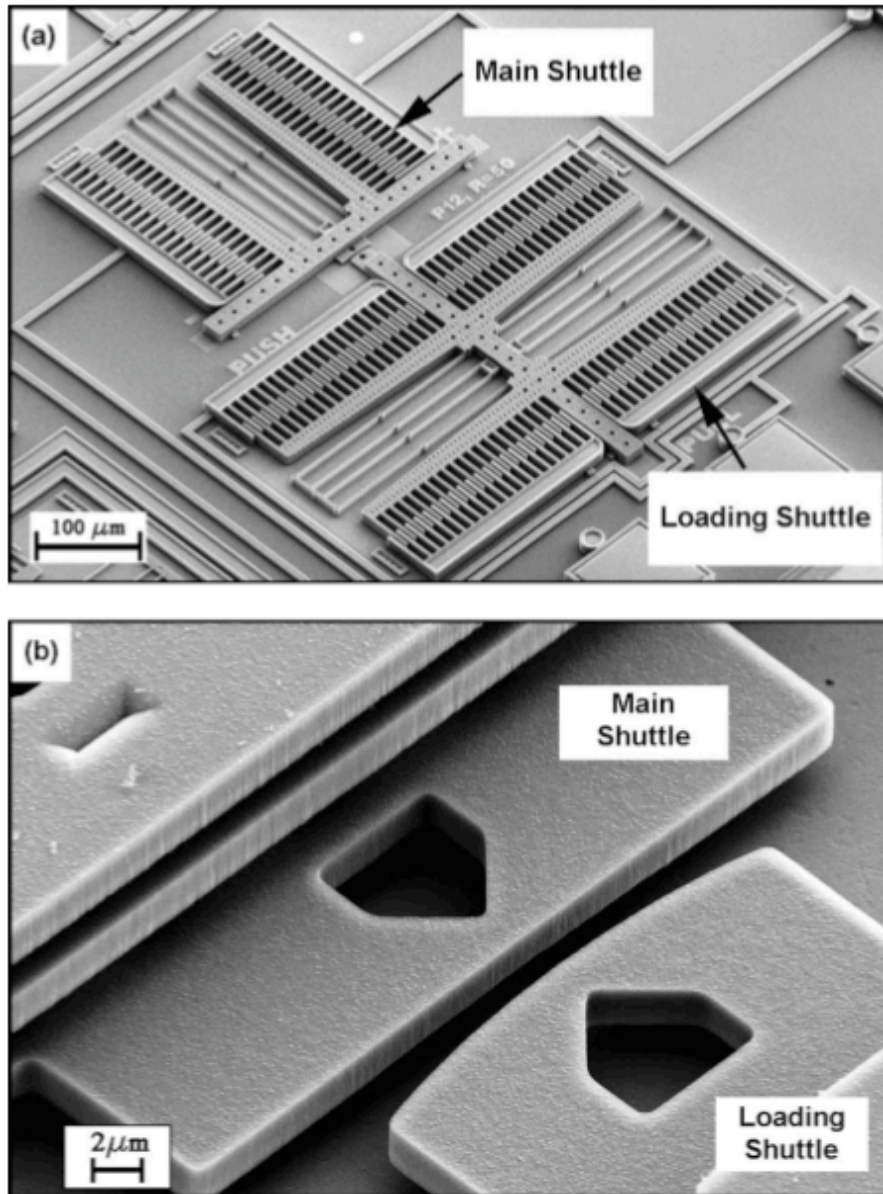


Figure 4.1 Scanning electron microscope images of the MEMS sidewall tribometer showing (a) the entire test structure used to characterize tribological degradation and (b) a high magnification image of the contact area.

The device used in these experiments is a compact MEMS sidewall tribometer modified from the design by Timpe and Komvopoulos⁸ and fabricated at Sandia National Laboratories. Figure 4.1 shows a scanning electron micrograph of the overall device, and a high magnification image of the contacting surfaces. The MEMS tribometer allows for the evaluation of a wide range of surface treatments and contact conditions and consists of two perpendicularly driven shuttles whose motions are controlled using electrostatic comb drive actuators. One shuttle (referred to as the loading shuttle and driven by the load and unload actuators) is used to move a curved protrusion (50 micron radius) normal to the sidewall contact interface, while the other shuttle (referred to as the main shuttle and driven by the push and pull actuators) produces motions parallel to the sidewall contact interface. Adhesion data is obtained by determining the critical force to separate the contacting shuttles. Dynamic friction data for lateral motion is obtained by comparing the amplitude of the oscillating main shuttle while the loading shuttle is in contact to that when it is out of contact. Tribological degradation can be evaluated in terms device lifetimes and changes in friction coefficient and force of adhesion.

The devices are fabricated using Sandia National Laboratories' SUMMiT V surface micromachining technology⁹ and are constructed from layers of polycrystalline silicon separated by layers of silicon dioxide. Each layer can be patterned and etched, allowing complex structures to be fabricated. After fabrication, the sacrificial oxide is removed using an aqueous HF etch. The die are then rinsed in deionized water, and transferred to methanol. The methanol is supercritically extracted in CO₂ to avoid collapse of the structures due to capillary forces. The devices are then transferred to a

vacuum chamber where they are plasma-cleaned and oxidized in-situ prior to monolayer deposition.

Monolayer deposition consists of exposing the cleaned die to a low pressure of amino-functionalized silanes. The molecules react with surface hydroxyl groups to form a hydrophobic film, as illustrated schematically in Figure 4.2. This process results in a water contact angle by sessile drop of approximately 110 degrees. A complete description of the monolayer treatment process can be found elsewhere.¹⁰ Time-of-flight secondary ion mass spectrometry (ToF-SIMS) indicates that this coating process results in a surface coverage of approximately 2.5×10^{14} molecules/cm².¹¹ Of the available chemistries for chemisorbed organic molecules on silicon, the linkage via Si-O bonds in FOTAS represents the strongest possible attachment chemistry (Si-O = 799.6 ± 13.4 kJ/mol).¹²

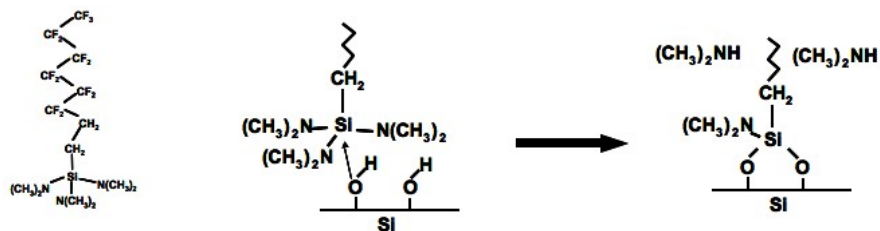


Figure 4.2. Schematic representation of the FOTAS reaction with a hydroxylated silicon surface. Vapor phase FOTAS is introduced into a vacuum chamber and upon collision with the surface reacts to form silicon oxygen bonds.

Furthermore, FOTAS has three available bond sites on the head group available for reaction with surface hydroxyl bonds or cross-linking within the layer, further strengthening the attachment of the molecule to the surface.

4.2.2 MEMS Operation and Set-Up

The two shuttles are driven by perpendicular sets of electrostatic comb drive actuators.¹³ The force output of the comb drives is calculated using a parallel plate approximation and is given by the equation

$$F_{el} = \alpha V^2 \quad (4.1)$$

where α is a constant determined by the particular actuator geometry ($= 1.114 \times 10^{-9}$ N/V²) for the main shuttle actuators and 2.228×10^{-9} N/V² for the loading shuttle actuators) and V is the voltage applied between the fixed and movable comb fingers.

The shuttles are suspended off the substrate using conventional folded flexure suspension systems. The mechanical restoring force generated by these suspension beams is given by

$$F_r = kd \quad (4.2)$$

where k is the suspension stiffness ($= 0.11935$ N/m for the main shuttle and 0.2287 N/m for the loading shuttle) and d is the displacement from equilibrium.

The external normal force is dictated by a force balance between the mechanical restoring force in the suspension system of the loading shuttle and the electrostatic forces generated by the load and unload actuators:

$$F_N = \alpha_L (V_L^2 - V_U^2) - k_L x_c \quad (4.3)$$

where α_L is the proportionality constant of the loading shuttle, V_L and V_U are the voltages applied to the load and unload actuators, k_L is the suspension stiffness of the loading shuttle, and x_c is the displacement at contact.

The lateral, or friction force, is determined from a balance between the electrostatic force generated by the push and pull actuators of the main shuttle and the restoring force of the suspension springs

$$F_f = \alpha_M (V_{push}^{\max 2} - V_{pull}^{\min 2}) - k_m y_{\max} \quad (4.4)$$

where α_M is the proportionality constant of the main shuttle, V_{push}^{\max} and $V_{pull}^{\min 2}$ are the maximum push drive voltage and the minimum pull drive voltage voltages, k_M is the suspension stiffness of the main shuttle, and y_{\max} is the maximum main shuttle displacement.

The voltage supplied to produce lateral motion causes an electric field imbalance in the vertical direction that results in a lifting, or “levitation force” that causes the shuttle height to vary with lateral shuttle distance.¹⁴ This undesirable effect can be significantly reduced through the use of tailored waveforms applied to the actuators.¹⁵ Two programmable arbitrary waveform generators (Pragmatic Instruments model 2414A) and two DC power supplies were used here to reduce the effects of levitation on contact height variation.

The device was operated in a custom-made environmental chamber of UHV compatible components containing a viewport, so that the device motion could be recorded during operation in a controlled environment. Before testing, the experimental chamber was connected to a constant dry nitrogen flow at ~0.5 L/min and purged until a concentration of less than 20 ppmv O₂ and less than 150 ppmv H₂O was achieved.

4.2.3 Normal Cyclic Contact

To quantitatively measure the tribological degradation arising from normal impact contact, the force required to separate the contacting surfaces (i.e., the adhesion force) was measured as a function of normal loading cycles. In order to measure the adhesion force, the main shuttle was levitated to a desired height by applying equal DC voltages to the push and pull actuators. The waveform shown in Figure 4.3 was then applied to the load and unload actuators of the loading shuttle at a frequency of 1 Hz.

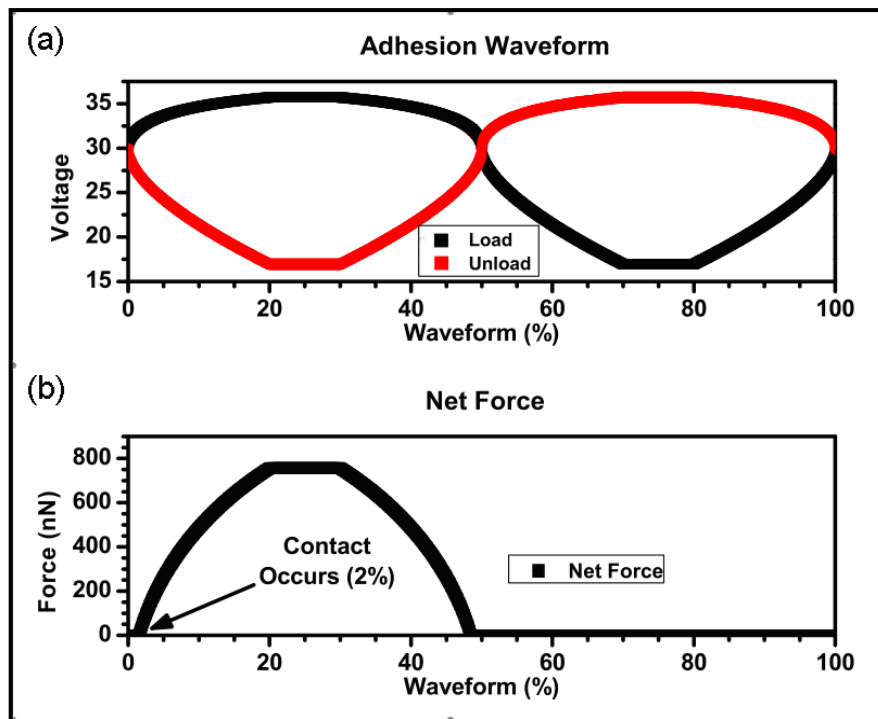


Figure 4.3 (a) The waveform used to control the loading shuttle during the adhesion force measurements and during impact loading and (b) the net applied force at the contact location.

This waveform was designed to reduce the vertical motion associated with bringing the surfaces into contact. The maximum load reached was 750nN. Images were acquired throughout the entire waveform at 50 frames per second and the adhesion force was dictated by the instant at which the two shuttles separated. At this instability point, the adhesion force is calculated through a force balance between the electrostatic forces in the load and unload actuators and the mechanical restoring force in the suspension system:

$$F_{ad} = k_L x_C - \alpha (V_L^{s2} - V_U^{s2}) \quad (4.5)$$

where the superscript of the voltage values indicate that the measurements are taken at the instant of surface separation. During testing, each adhesion measurement was repeated 10 times for statistical analysis.

At the start of testing, an initial adhesive force measurement was made to quantify the initial tribological behavior. The loading shuttle was then oscillated in and out of normal contact at 100 Hz with a maximum applied load of 750nN and a contact velocity of approximately 2 mm/s. This corresponds to a kinetic energy 1.46×10^{-15} J. With an estimated contact area of 7.4×10^{-14} m² (assuming Hertzian contact of a smooth cylinder on a flat),¹⁶ the work done per unit area for one cycle is approximately 2.01×10^{-2} J/m². The normal cyclic contact at 100 Hz was stopped periodically and the low frequency adhesion force measurement repeated to monitor changes in the tribological behavior of the contact interface. It should be noted that the reactive ion etch process leaves the polycrystalline silicon surfaces with vertical etch striations. Figure 4.4 shows a 2 x 8

micron AFM image of a typical polycrystalline sidewall surface created in the Summit V process.

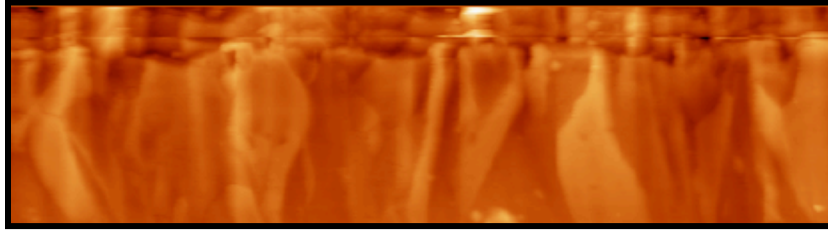


Figure 4.4 A 2 x 8 micron AFM image of a typical flat polysilicon sidewall surface created by the Summit V manufacturing process. A line scan across the entire width gives a rms roughness of 11nm.

A line scan across the entire 8 micron width gives a RMS roughness of 11nm and a striation period of approximately 100 nm. However RMS roughness measurements are length dependant and the roughness for the sidewall contacts has been reported elsewhere as being as high as 20 nm.¹⁷ Therefore as the shuttles come into contact during the normal impact experiments, there may be a slight translation of 0 to 25 nm as the surfaces slip into registry. In addition, due to the inefficiencies in the levitation compensation waveform, there is a residual vertical motion and therefore possible vertical slip of the contact of up to 50 nm.

4.2.4 Sliding Cyclic Contact

To probe tribological degradation in sliding contact, the amplitude of shuttle oscillation was measured as a function of cycle number for a constant load of 750 nN. Before testing, an initial adhesion measurement was recorded using the method described in Section 4.2.3. The push and pull actuators of the main shuttle were then connected to the arbitrary waveform generators, and a levitation-compensated waveform was applied

to yield a non-contact oscillation amplitude of approximately 18 microns. Figure 4.5 shows the applied waveform and corresponding free oscillation profile as a function of waveform percent. Images were acquired at 28% and 78% of the waveform, where the maximum lateral displacement from equilibrium is reached and the shuttle is momentarily stationary. The amplitude of oscillation is then determined as the difference in lateral position between these two endpoints.

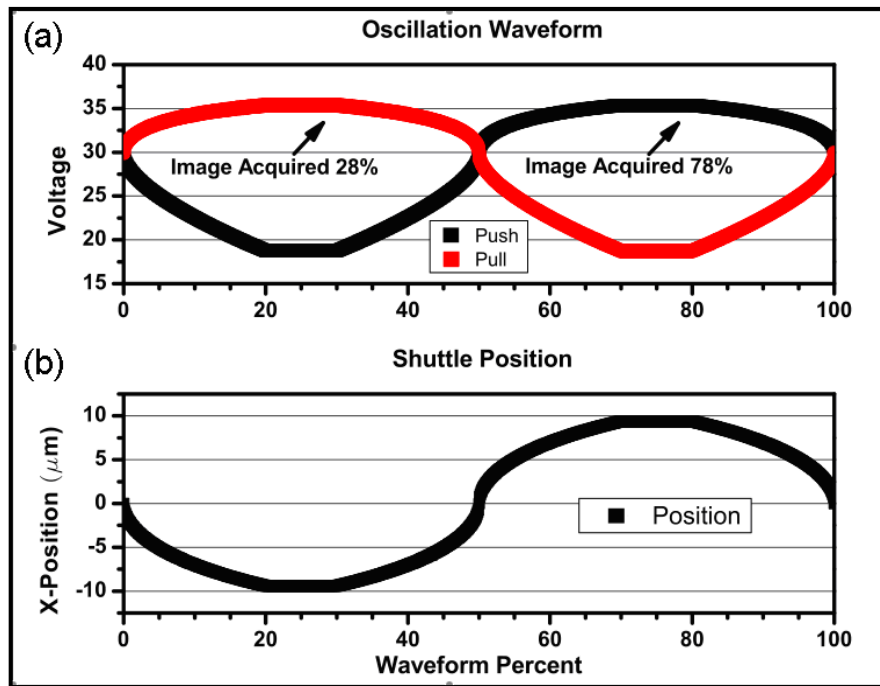


Figure 4.5 (a) The waveforms applied to the push and pull comb drive actuators of the main shuttle during the dynamic sliding experiments and (b) the corresponding theoretical free oscillation shuttle position.

For sliding contact measurements, the load and unload combs were controlled by separate DC power supplies. Before being brought into contact, the loading shuttle was elevated to the same height as that of the shuttle by applying equivalent voltages to the load/unload combs. The main shuttle was then oscillated at a frequency of 20 Hz and a

baseline measurement of the oscillation amplitude without contact was taken for five minutes. Once the baseline was established, the post was brought into contact and the load increased over the course of approximately 10 seconds. The amplitude was then monitored as a function of oscillating cycles throughout testing until device failure as defined by a cessation of motion. The dynamic friction coefficient was calculated using the method described by Srinivasin et al.¹⁸ where the change in driven oscillator amplitude is linearly related to the coefficient of kinetic friction. After failure the contact was separated and the load reapplied to verify that a reproducible failure had occurred. A final adhesion measurement was then taken.

4.3 Results and Discussion

4.3.1 Normal Contact

Figure 4.6 shows sequences of adhesion force versus normal loading cycles for two different devices (referred to as device one and device two). The data points represent the average of ten measurements and the error bars represent one standard deviation above and below the corresponding average. Results indicate that there are three primary stages of degradation. The first stage can be referred to as the “run-in period” and displays relatively stable tribological behavior.

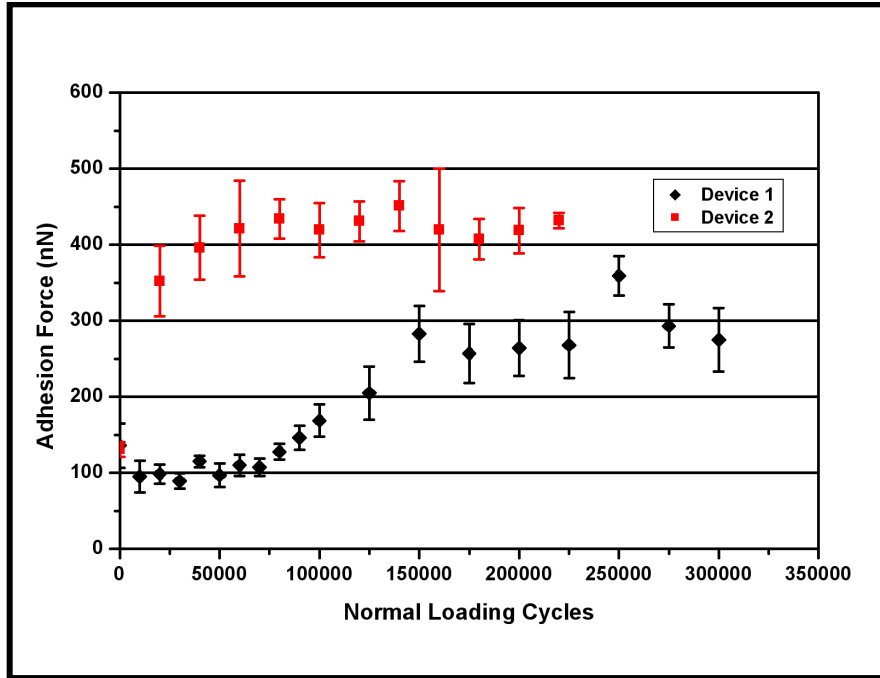


Figure 4.6. The measured adhesion force between the shuttles as a function of normal loading cycles. Results are shown for two individual devices.

For device one, this run-in period occurred during the first 70,000 impact cycles. For device two, the run-in period was unobservably small. Differences in run-in time between the two devices can be attributed to variations from device to device in surface roughness, monolayer coverage, and surface contamination by water. After the run-in period, the contact interfaces underwent a rapid degradation in tribological properties over the course of 50,000 to 100,000 cycles. During the final stage of tribological degradation, relatively less change was observed in the measured adhesion force and the experiments were halted. Another significant observation which can be drawn from Figure 4.6 is the increase in the standard deviation with tribological degradation of the contact interface. This suggests a heterogeneous physical and chemical degradation,

which is consistent with the non-uniform pressures and real contact variability in sidewall MEMS contacts.

The observed changes in the tribological behavior can be attributed to various physical and chemical degradation mechanisms. Physical degradation mechanisms such as the generation of wear debris (i.e., fracture of surface asperities) and roughness reductions (i.e., deformation of surface asperities) could contribute to the changes in properties through reduction of the relative surface separation and increase in the real contact area. At the conclusion of testing, high resolution SEM images of the contact area of device one (Figure 4.7) showed no visible wear particle accumulation or visible change in surface topography. However, the presence of wear debris or surface roughness changes below 50 nm is difficult to detect with scanning electron microscopy. Furthermore, the presence of sidewall striations would require sidewall imaging before and after wear to conclusively detect surface topographic changes of this size. Therefore, changes of this order or smaller cannot be detected nondestructively on sidewall surfaces. It is then necessary to state that the effects of physical degradation mechanisms cannot be discounted and changes in adhesion of a device without a monolayer coating have previously been reported with no SEM observable surface changes.¹⁹

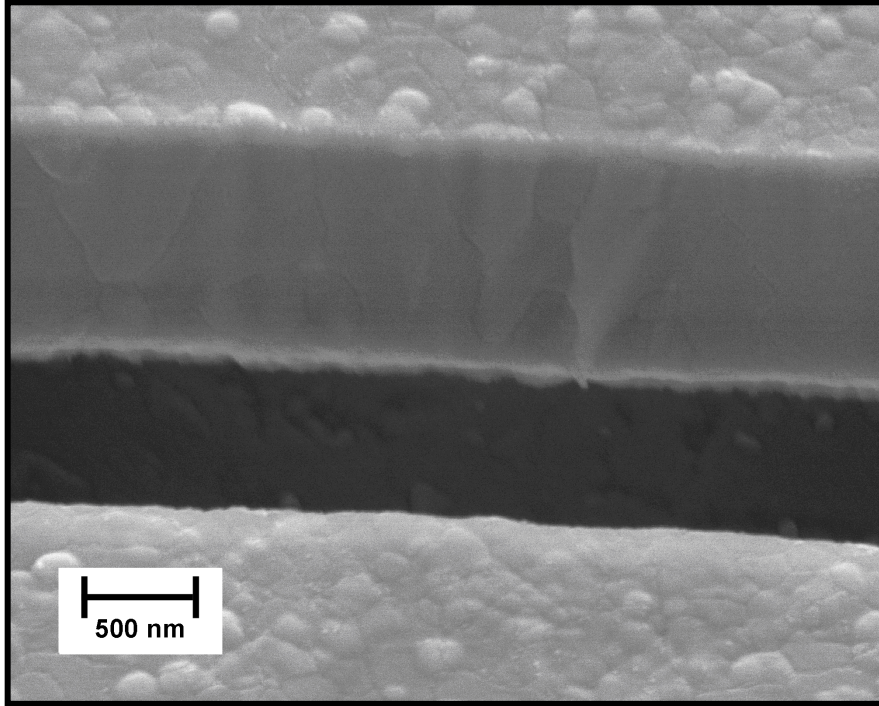


Figure 4.7 SEM image of the contact area of device one in after approximately 300,000 normal loading cycles.

In addition to the physical mechanisms that change the roughness and surface debris at the contact interface, chemical degradation mechanisms can also contribute to the measured changes in the adhesion force. This is of particular relevance given the fact that the tested microdevices are coated with the hydrophobic, low surface energy FOTAS monolayer. When this monolayer is removed at local contact points during impact loading, the hydrophilic, high surface energy SiO_2 layer underneath will be exposed thereby increasing the measured adhesion force. The reasonableness of monolayer removal can be examined through a simple energetic comparison. If the number of siloxane bonds per unit area on the surface is examined, having a bond energy of $799.6 \pm 13.4 \text{ kJ/mol}$,¹² a surface density of $2.5 \times 10^{14} \text{ molecules/cm}^2$,¹¹ and assuming two siloxane bonds per molecule, the energy per unit area required to sever all of the bonds is

3.5 J/m². The simple calculation in Section 4.2.3 yielded a value of 2.0×10^{-2} J/m² for the work done per unit area under the normal impact loading conditions. However, a closer look at the real area of contact using the Greenwood-Williamson model,²⁰ approximating the surface asperities as uniform spheres with an rms roughness minimum of 11 nm and a maximum of 20 nm gives a real contact area between 5.95×10^{-17} m² and 4.73×10^{-17} m² respectively. If this real area of contact is used to estimate the energy imparted to the surface in normal contact, the energy per unit area increases to a range of 24.5 J/m² to 30.6 J/m². Therefore, the current impact loading is easily severe enough to remove the chemisorbed FOTAS molecules within the real contact area.

4.3.2 Sliding Contact

A sequence of oscillation amplitude versus cycles for an external contact load of 750 nN is shown in Figure 4.8. The free oscillation amplitude for the current waveform is equal to 18 ± 0.2 mm. As the contact force is ramped up, there is a drop in oscillation amplitude of approximately 7 mm. This corresponds to a kinetic friction coefficient of 0.43. This is significantly higher than static friction coefficients reported for other similar surface treatments and appears to be closer to that of SiO₂ contacts.¹⁸

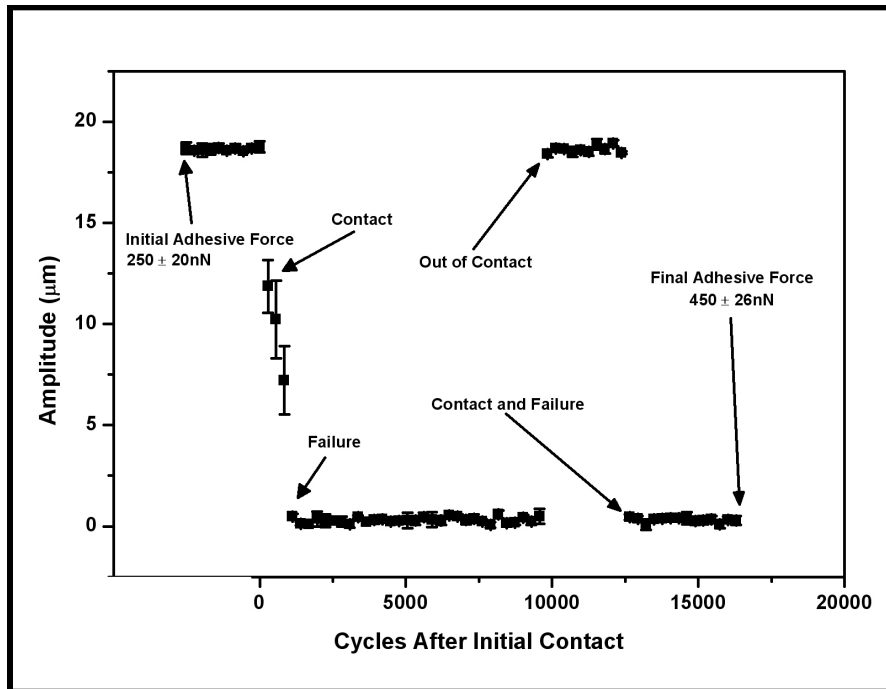


Figure 4.8 Oscillation amplitude versus sliding cycles for a normal load of 750nN. Also shown are the measured adhesion force values before and after testing.

The relatively high dynamic friction coefficient can be attributed to tribological degradation that occurs between successive displacement amplitude measurements. As can be seen by the subsequent amplitude measurements, in which the average amplitude of oscillation quickly decreases to zero over the course of 800 cycles, the rate of degradation for this particular test structure is extremely fast. Therefore, significant surface damage during the loading time can be responsible for the high friction measurement. In addition to the tribological degradation rate, the time to failure is also a strong function of the magnitude of the normal load and the inputted driving waveform. Therefore, even in the face of similar tribological degradation, longer lifetimes have been reported for device operating under lighter load and higher driving force conditions.^{21,22}

Further evidence of tribological degradation can be seen from changes in the adhesion force. The adhesion force was measured as described in Section 4.2.2 before and after the sliding experiments. The initial average adhesion force was 205 nN and the average post-failure adhesion force was 423 nN.

As in the normal contact experiments, the observed tribological degradation can be attributed to various physical and chemical mechanisms. While SEM images of the test surfaces revealed no observable changes in surface topography or generation of wear debris (see Figure 4.9), nanoscopic changes in the real contact area and decreases in the relative surface separation could have significant impact on the measured dynamic friction coefficient and the adhesion force.

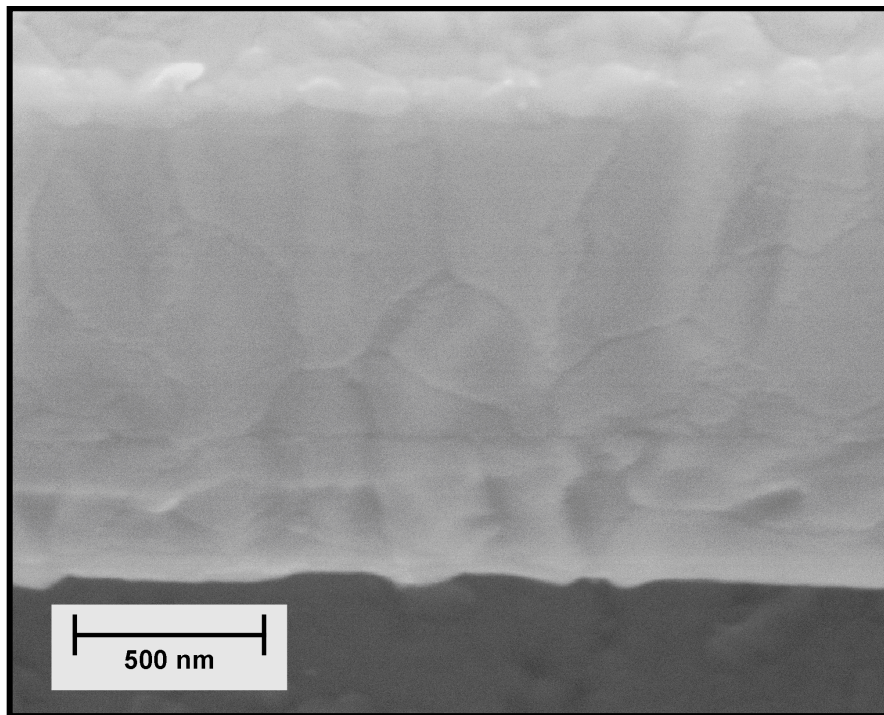


Figure 4.9 SEM image of the contact area after approximately 800 cycles of sliding contact.

Also, given that the as-fabricated surfaces are coated with a low surface energy monolayer, removal of this monolayer to expose the SiO₂ subsurface could also have a noticeable effect on the measured tribological characteristics. The feasibility of monolayer removal can be checked by comparing the energy required to sever the relevant siloxane bonds (~3.5 J/m²) with the work of friction per unit area:

$$W_f = \frac{F_f \Delta y}{A_r} \quad (4.6)$$

where F_f is the force of friction, Δy is the sliding distance, and A_r is the real contact area estimated using the Greenwood-Williamson model. For the initial friction measurement shown in Figure 4.8, this calculation yields a work of friction value of 52.9 J/m², which is more than enough to break all of the silicon-oxygen bonds in the real contact area.

Regardless of the specific degradation mechanism, the monolayer fails to protect the device from degradation in tribological performance. Therefore, MEMS devices whose functionality depends upon mechanical contact will require more robust tribological solution such as replenishable surface passivation layers or more strongly bound coatings that resist both physical and chemical surface degradation.

4.4 Summary

A surface micromachined tribometer was used to investigate tribological degradation in monolayer-coated polysilicon MEMS sidewall interfaces under sliding and normal contact conditions. Under normal contact conditions, the adhesion force increased by a factor of two after degradation compared to the initial as-fabricated surface. Under sliding conditions in dry nitrogen, the degradation began immediately

upon contact and caused device motion to cease within a relatively short number of sliding cycles. A two-fold increase in adhesion force was also observed. The degradation in the tribological properties can be attributed to physical mechanisms, including fracture and deformation of surface asperities, and to chemical mechanisms such as changes in the surface energy due to removal of chemisorbed monolayer molecules. A simple estimate of energy input at the interface due to sliding and normal contact suggests that the available mechanical energy greatly exceeds that required to break all of the siloxane bonds between the monolayer and the surface.

4.5 Acknowledgements

Special thanks to Josh Wien for AFM data taken at the AML at University of New Mexico. The AFOSR Extreme Friction MURI F49620-01-1-0132/FA9550-04-1-0381 and Sandia National Laboratories are gratefully acknowledged for supporting the work reported here. Sandia is a multi-program laboratory operated by Sandia Corporation, a Lockheed Martin Company, for the United States Department of Energy's National Nuclear Security Administration under contract DE-AC04-94AL85000.

REFERENCES

- [1] R. Maboudian and C. Carraro, *J. Adhesion Sci. and Technol.* **17**, 583 (2003).
- [2] R. Maboudian and R.T. Howe, *Tribology Lett.* **3**, 215 (1997).
- [3] S. M. Hsu and Z. C. Ying, *Nanotribology: Critical Assessment and Research Needs*. Boston: Kluwer Academic Publishers, (2003).

- [4] B. Bhushan, Tribology of MEMS Components and Materials, (1998).
- [5] S. Ren, S. Yang, Y. Zhao, J. Zhou, T. Xu, and W. Liu, Tribology Lett. **13**, 233 (2003).
- [6] R. A. Singh, E. Yoon, H. Han, and H. Kong, Wear. **262**, 130 (2007).
- [7] M.T. Dugger, D.C. Senft, and G.C. Nelson, Microstructures and Tribology of Polymer Surfaces, V.V. Tsukruk and K.J. Wahl, Eds., Washington, DC: American Chemical Society, (1999).
- [8] S. J. Timpe and K. Komvopoulos, Rev. Sci. Instrum. **78** (6), 065106-1 (2007).
- [9] J. J. Sniegowski and M. P. de Boer, Annu. Rev. Mater. Sci. **30**, 299 (2000).
- [10] M. G. Hankins, P. J. Resnick, P. J. Clews, T. M. Mayer, D. R. Wheeler, D. M. Tanner, and R. A. Plass, Proc. SPIE. **4980**, 238 (2003).
- [11] J.A. Ohlhausen, and K.R. Zavadil, J. Vac. Sci. Technol. A. **24** (4), 1172 (2006).
- [12]"Bond Dissociation Energies in Diatomic Molecules", in CRC Handbook of Chemistry and Physics, 88th Edition (Internet Version 2008), David R. Lide, ed., Boca Raton, FL: CRC Press/Taylor and Francis, 2008.
- [13] W. C. Tang, T. -C. H. Nguyen, and R. T. Howe, Sens. and Actuators, **20** (1-2), 25 (1989).
- [14] W. C. Tang, M. G. Lim, and R. T. Howe, J. of Microelectromech. Syst. **1** (4), 170 (1992).
- [15] S. J. Timpe, D. A. Hook, M. T. Dugger, and K. Komvopoulos, Sensors & Actuators: A. Physical, to be published.
- [16] K. L. Johnson, Contact Mechanics. Cambridge, UK: Cambridge University Press, (1985).

- [17] D. B. Asay, M. T. Dugger, and S. H. Kim, *Tribology Lett.* **29**, 67 (2008)
- [18] U. Srinivasan, J. D. Foster, U. Habib, R. T. Howe, D. C. Senft, and M. T. Dugger, ,
Proc. of the 1998 Solid-State Sens. Act. Workshop, Hilton Head, (1998).
- [19] M. A. Philippine, S. J. Timpe, and K. Komvopoulos, *App. Phys. Lett.* **91**, 063102
(2007)
- [20] J. I. McCool, *Wear*, **107**, 37 (1986).
- [21] S. J. Timpe, K. Komvopoulos, and M. T. Dugger, *Journ. App. Phys.* **102** (12),
123503, (2007).
- [22] J. Rutledge, personal communication

Chapter 5

Wear of Polysilicon Surface Micromachines Operated in High Vacuum

Shannon J. Timpe, Daan Hein Alsem, D. Adam Hook, Michael T. Dugger, and Kyriakos

Komvopoulos

Article Published: JMEMS, Vol. 18, NO. 2, April 2009

Abstract - The evolution of wear at sidewall surfaces of polysilicon microelectromechanical systems was investigated in high vacuum under controlled normal load and sliding speed conditions. The static adhesion force was used as an indicator of the changes in wear characteristics occurring during oscillatory sliding contact. Measurements of the static adhesion force as a function of sliding cycles and scanning electron microscopy observations of micromachines from the same batch process subjected to nominally identical testing conditions revealed two distinctly different tribological patterns, namely, low-adhesion/high-wear behavior and high-adhesion/low-wear behavior. The static adhesion force and wear behavior were found to be in direct correlation with the micromachine operational lifetime. Transmission electron microscopy, selected area diffraction, and energy dispersive X-ray spectroscopy yielded insight into the origin, microstructure, and composition of wear debris and agglomerates adhered onto the sliding surfaces. Results demonstrate a strong dependence of micromachine operational life on the removal of the native oxide film and the organic monolayer coating as well as the formation of agglomerates consisting of organic coating material and wear debris.

5.1 Introduction

Advances in microfabrication technology have enabled the design of a wide range of microscopic devices capable of performing various sensing, control, and actuation tasks. Because the operation of these devices depends on a combination of electrical and mechanical principles, they are commonly referred to as microelectromechanical systems (MEMS). Increasing demands for MEMS that can perform various mechanical functions, such as micrometer-scale motions in different applications ranging from complicated biological and photovoltaic structures to simple sensors and actuators, have led to the development of devices with load-bearing contact interfaces, notably micromotors¹, microswitches², and digital micromirrors³.

Surface interactions assume a dominant role when the device dimensions are reduced to micrometer levels. At very small length scales, adhesion, electrostatic, and friction forces exceed inertial forces often by orders of magnitude. This increases the importance of tribological properties, and device operation can be significantly affected by the evolution of friction, adhesion, and mechanical wear. Since the sizes of polycrystalline grains, asperities, and wear debris can be of order of magnitude comparable to that of some of the device dimensions, topographical changes due to the removal of contacting asperities and the formation of wear debris can drastically alter the tribological characteristics of the device. The development of wear processes at contact interfaces of MEMS is usually accompanied by abrupt adhesion and friction force fluctuations, producing detrimental effects on the device functionality and efficiency. In addition to these mechanical effects, wear debris may influence the electrical behavior by

bridging the gaps between electrically isolated surfaces or by preventing electrical conduction between surfaces of contact-mode devices, such as microswitches. The alteration of mechanical and electrical behaviors by mechanical wear can become the dominant factor affecting the device lifetime.

Several researchers have attempted to study wear phenomena at MEMS scales. For example, Tanner *et al.*⁴ studied the effects of humidity and surface treatment on the formation of wear debris in a microengine, and Patton *et al.*^{5,6} examined tribological effects on the reliability of an electrostatic lateral output motor. While both of these studies elucidated the effect of operating environment on the wear mechanisms and the formation of wear debris in specific devices, difficulties were encountered in relating the failures observed in these structures to generalized design rules. Other investigators used simple experimental setups to approximate the contact conditions in MEMS structures. For instance, Beerschwinger *et al.*⁷ used a pin-on-disc apparatus to study the wear behavior of single-crystal silicon microstructures with different geometric configurations and surface coatings, whereas Bandorf *et al.*⁸ and Bhushan *et al.*⁹ used an atomic force microscope (AFM) to characterize the wear behavior of MEMS devices. However, the results of these investigations are not necessarily indicative of the tribological characteristics of MEMS contact interfaces due to the unique contact conditions in the pin-on-disc and AFM experiments.

The previous studies point toward a need for specialized microdevices and experimental procedures for testing under controlled environmental and loading conditions that directly mimic *in situ* device behavior. Various specialized surface

micromachines have been used to characterize the tribological properties of MEMS devices. Much of the early work on surface characterization and friction testing has been discussed by Komvopoulos¹⁰. Senft and Dugger¹¹ and de Boer *et al.*¹² conducted friction and adhesion experiments using micromachined test structures. Flater *et al.*¹³ performed wear experiments with a surface micromachine that generated nanoscopic sliding at the contact interface. Alsem *et al.*^{14,15} studied friction and wear mechanisms at sidewall surfaces of polysilicon microdevices operated in ambient air under loads in the micronewton range and observed that the dominant wear mechanism was abrasion. Timpe and Komvopoulos¹⁶ designed a surface micromachine suitable for studying sidewall adhesion in MEMS and devised a procedure to predict the contributions of both contacting and noncontacting asperities to the total adhesion force at the inception of surface separation. Static friction experiments carried out by Lumbantobing and Komvopoulos¹⁷ with surface micromachines demonstrated a nonlinear dependence of the interfacial shear strength on the contact pressure and strong effects of the normal force, apparent contact area, and relative humidity on the static coefficient of friction of in-plane polysilicon surfaces. In a later friction study by Timpe and Komvopoulos¹⁸, the true static coefficient of friction was introduced by including contributions from both van der Waals and capillary forces to the normal force applied at micromachine sidewall interfaces.

The previous studies show that significant effort has been devoted to examine adhesion and friction phenomena at MEMS interfaces. However, relatively less research has been carried out to elucidate the evolution of mechanical wear and associated

mechanisms, particularly under dynamic contact conditions. The main objective of this investigation was to bridge this gap of knowledge by performing wear experiments with special surface micromachines operated in high vacuum under controlled loading and sliding speed conditions. Static adhesion force measurements, electron microscopy observations, and microanalysis results demonstrated a strong dependence of sidewall wear behavior on the formation of wear debris and the development of agglomerates consisting of wear debris and organic material from the worn-off monolayer coating.

5.2 Description of the Test Micromachine

Test micromachines were fabricated by the Sandia National Laboratories Ultra-planar Multi-level MEMS Technology 5 (SUMMiT V) fabrication process¹⁹, which includes a ground plane and four structural layers all consisting of highly doped n-type polysilicon. All of the layers were deposited by low-pressure chemical vapor deposition and etched by reactive ion etching. Silicon dioxide was used as the sacrificial layer and silicon nitride as an electrical isolation layer. The last process step involved the release of the test micromachines and the application by vapor deposition of a hydrophobic organic monolayer coating consisting of tridecafluoro-1,1,2,2 tetrahydrodecyltris(dimethylamino) silane²⁰. After fabrication, chips with several micromachines were wire bonded in 24-pin ceramic dual in-line packages for voltage application.

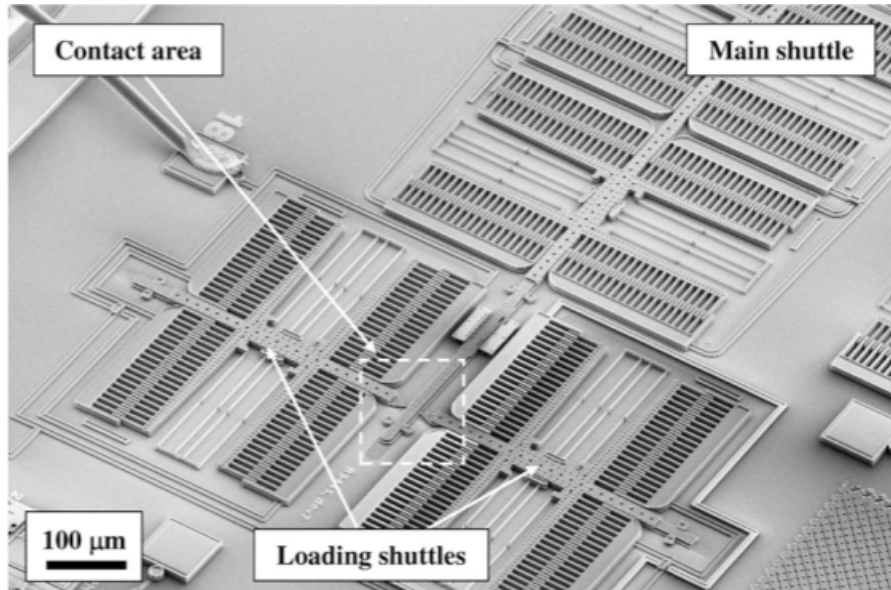


Figure 5.1 SEM micrograph of the polysilicon surface micromachine used to perform reciprocating sliding experiments in high vacuum under controlled loading and sliding speed conditions typical of MEMS devices.

Figure 5.1 shows a scanning electron microscope (SEM) image of the polysilicon micromachine used in this study. The micromachine includes a main shuttle for generating tangential (sliding) motion and two loading shuttles for applying a normal force at the sidewall surface of the main shuttle. In the experiments of this study, the desired normal force was generated by electrostatic actuation of only one of the loading shuttles using conventional comb drives with interdigitated fingers. Reciprocating motion was generated by individual electrically isolated banks of comb-drive actuators on each side of the shuttle. For convention, the two actuators of the main shuttle will be referred to as push and pull comb-drive actuators, while the two actuators of the loading shuttle, one close and the other remote from the contact interface, will be referred to as load and unload comb-drive actuators, respectively. The electrostatic forces generated by the main shuttle F_m and the loading shuttle F_l are given by²¹

$$F_m = \frac{N_m \epsilon_0 h}{g} (V_{push}^2 - V_{pull}^2) \quad (5.1)$$

$$F_l = \frac{N_l \epsilon_0 h}{g} (V_{load}^2 - V_{unload}^2) \quad (5.2)$$

where N_m (= 80) and N_l (= 40) are the numbers of comb fingers in the actuators of the main and loading shuttles, respectively, ϵ_0 is the permittivity in vacuum ($= 8.854 \times 10^{-12}$ F/m), h is the thickness of the polysilicon structural layer ($\sim 7.2 \mu\text{m}$), g is the gap between the comb fingers ($\sim 1.8 \mu\text{m}$), V_{push} and V_{pull} are the voltages applied to the push and pull actuators of the main shuttle, and V_{load} and V_{unload} are the voltages applied to the load and unload actuators of the loading shuttle.

The shuttles are supported by sets of double-folded flexure suspension systems, which can be modeled as linear springs of mechanical restoring force given by

$$F_r = \frac{1}{2} N_f E x w^3 d \left(\frac{1}{L_1^2} + \frac{1}{L_2^2} \right) \quad (5.3)$$

where N_f is the number of double-folded flexures (two for the main shuttle and one for the loading shuttle), E is the elastic modulus of polysilicon ($= 165 \text{ GPa}^{22}$), w is the width ($\sim 1.2 \mu\text{m}$) and d is the thickness ($\sim 4.5 \mu\text{m}$) of the suspension beams, x is the in-plane shuttle displacement, and L_1 ($\sim 271 \mu\text{m}$) and L_2 ($\sim 256 \mu\text{m}$) are the lengths of the inner and the outer suspension beams, respectively. Alternatively, the mechanical restoring force during operation can be determined from the voltages applied to the load and unload comb drives at the instant of contact, V_{load}^{con} and V_{unload}^{con} , respectively, using the following relationship:

$$F_r = \frac{N_f \epsilon_0 h}{g} \left[(V_{load}^{con})^2 - (V_{unload}^{con})^2 \right] \quad (5.4)$$

To minimize inaccuracies in the loads calculated during device operation, electrostatic equations were used throughout, i.e., the mechanical restoring force was calculated using (5.4) rather than (5.3). The micromachine dimensions used in (5.1)–(5.4) were determined from SEM images.

The main shuttle possesses a long free extension that enables contact with the loading shuttle. When a voltage is applied to the comb drives of the main shuttle, the entire structure including this extension moves parallel to the contact interface, generating the shear (friction) force in the sliding experiments. The loading shuttle was used to apply a desirable normal force to the sidewall contact interface. A cylindrical protrusion at the side of the loading shuttle was brought into contact with the main shuttle extension by applying a suitable voltage to the comb-drive actuators of the loading shuttle. Figure 5.2 shows a high-magnification SEM micrograph of the protrusion end used to apply the desired normal force to the sidewall surface of the main shuttle during testing. The resulting contact geometry resembles a cylinder-on-flat contact configuration. In all of the micromachines, the cylindrical protrusion of the loading shuttle was 4 μm in radius and 2.3 μm in height, as measured from SEM images.

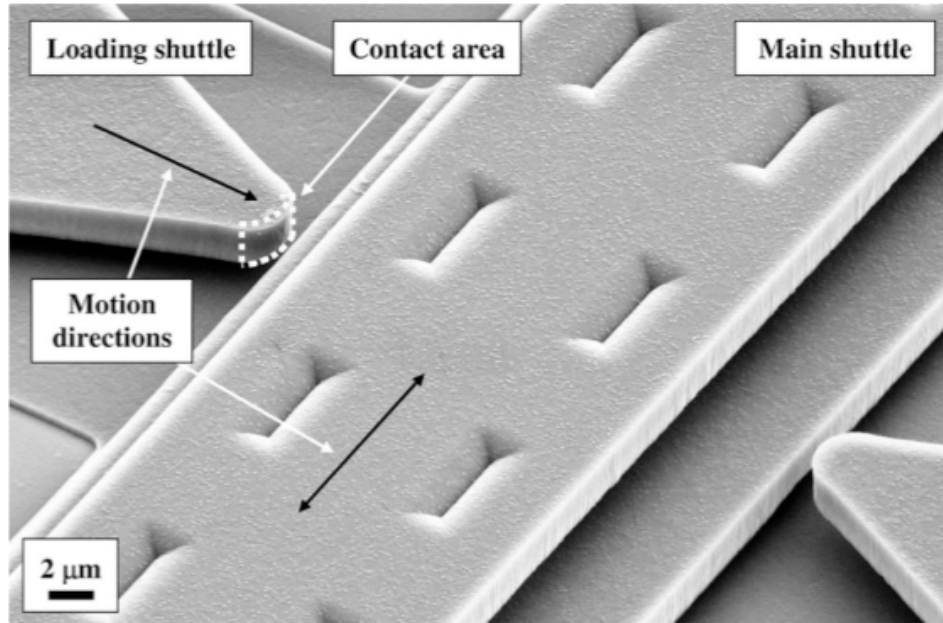


Figure 5.2. SEM micrograph showing critical portions of the main and loading shuttles where sidewall surface contact occurred during reciprocating sliding.

In addition to providing translational motion, the comb-drive actuators produce a levitation force that raises the shuttles to a vertical position, depending on the applied voltage²³. This levitation force is due to an imbalanced electrostatic field generated by the ground plane below the suspended microstructure. To account for the levitation force effect, the dynamic levitation compensation method developed by Timpe *et al.*²⁴ was used to ensure relatively uniform and constant contact area throughout the oscillatory motion. In this method, the voltages applied to the push/pull actuators of the main shuttle and the load/unload actuators of the loading shuttle are adjusted throughout each reciprocation cycle to minimize out-of-plane motion.

5.3 Experimental Procedures

One of the objectives in the wear experiments was to correlate the variation of the adhesion force with the changes in the sidewall surface morphology encountered during the micromachine operation lifetime. The measured static adhesion force was used as an *in situ* indicator of the changes in the tribological behavior during reciprocating sliding under high vacuum conditions, which were subsequently correlated to the generation of wear debris. The experimental procedure for wear testing in high vacuum under controlled loading and reciprocating sliding conditions is presented in this section along with a description of the microanalysis techniques used to characterize the wear debris and the material smeared onto the sliding surfaces.

The first step in the wear experiments was to measure the static adhesion force. The comb drives of the loading shuttle were first activated to bring the cylindrical protrusion in contact with the sidewall surface of the main shuttle under an external normal force $F_{ex} \approx 190$ nN, calculated from the force balance relationship

$$F_{ex} = F_l^{\max} - F_r \quad (5.5)$$

where F_l^{\max} is the maximum electrostatic force generated by the comb-drive actuators of the loading shuttle (5.2) and F_r is the mechanical restoring force generated by the mechanical suspension system (5.4). The shuttles were kept in contact under this force for 1 min to ensure equilibrium of the system. Then, the interface was gradually unloaded until the commencement of surface separation. At that instant, the adhesion force F_{ad} was determined from the force balance relationship

$$F_{ad} = F_r - F_l^{sep} \quad (5.6)$$

where F_l^{sep} is the electrostatic force produced by the comb-drive actuators of the loading shuttle (5.2) at the instant of surface separation ($F_l^{\text{sep}} < F_l^{\text{max}}$). This static adhesion measurement was repeated five times for statistical analysis. During contact, the adhesion force (5.6) contributes to the total normal force, which is the sum of all external and internal forces acting at the contact interface. Therefore, the applied external force (5.5) and the measured adhesion force (5.6) can be used to calculate the total normal force F_{tot} at the contact interface, i.e.,

$$F_{\text{tot}} = F_{\text{ex}} + F_{\text{ad}} \quad (5.7)$$

Once the baseline adhesion value was established, the micromachine was operated in sliding mode. First, a constant velocity waveform was used to set the main shuttle in oscillatory motion of peak-to-peak amplitude equal to $\sim 14 \mu\text{m}$. Then, the loading shuttle was slowly brought into contact with the oscillating main shuttle, and an external force $F_{\text{ex}} \approx 190 \text{ nN}$ was gradually applied to the contact interface by the cylindrical protrusion. After sliding for 20 min at 100 Hz under this external force, the shuttles were separated and the static adhesion force was measured again (using the procedure discussed previously) to assess any changes in the interfacial characteristics. Five measurements of the static adhesion force were obtained after each 20-min test interval.

All of the experiments were performed in a custom-made environmental chamber mounted on a vibration isolation table (PEPS-VX, Technical Manufacturing). The vacuum in the test chamber was controlled by a mechanical roughing pump (ACP 15, Alcatel Vacuum Products) and a cryosorption pump (500000, MDC Vacuum Products). During testing, the vacuum level was maintained at $\sim 7.5 \times 10^{-5}$ Torr. The packaged

chips were placed inside the chamber, and the 24 pins of the ceramic package were inserted into a pin socket that was wired to external power supplies. Voltages were applied to the micromachine by a set of computer-controlled arbitrary waveform generators (2414A, Pragmatic Instruments). The motion of the main shuttle was observed with an optical microscope (FS-60 Finescope, Mitutoyo America). The displacements of the main shuttle were captured by a video camera (GP-MF622, Panasonic) mounted onto the optical microscope and analyzed using custom-made imaging software.

The tested micromachines were examined with a field emission SEM (Zeiss Supra 55VP) at 10 kV and a dual-beam focused-ion-beam (FIB) system (FEI Strata DB235) at 5 kV. After obtaining the FIB and transmission electron microscope (TEM) samples^{14,15,16} TEM, selected area diffraction (SAD), energy-filtered TEM (EFTEM), and energy dispersive X-ray spectroscopy (EDS) were used to analyze the microstructure and composition of the agglomerated wear debris and smeared layers. A 300-kV JEOL 3010 (LaB6 filament) was used for TEM and SAD, and a 200-kV Philips CM200FEG (field emission gun) was used for EFTEM and EDS.

5.4 Results

Sliding experiments revealed two distinctly different wear behaviors. In one type of behavior, wear debris could not be observed on the sliding sidewall surfaces (even at high SEM magnifications) and the adhesion force increased dramatically with sliding time. The second type of wear behavior was characterized by the formation and agglomeration of fine wear debris on the sliding track, accompanied by a moderate increase in the

adhesion force. All of the 11 micromachines tested under identical conditions exhibited one of these two tribological trends. However, significant micromachine-to-micromachine deviation was observed in these experiments, consistent with previous studies of the tribological behavior of MEMS microstructures^{16,18} where the experimental scatter was attributed to variations in the local surface conditions due to process effects. Behavioral fluctuations caused by such local surface variations can complicate the study of scientific phenomena. Thus, to reduce micromachine-related variations and to perform an in-depth analysis of the surface phenomena encountered during sliding, the following results and discussion are for the two characteristic micromachine adhesion/wear behaviors obtained under identical external force (~ 190 nN), oscillation frequency (100 Hz), and vacuum ($\sim 7.5 \times 10^{-5}$ Torr) conditions.

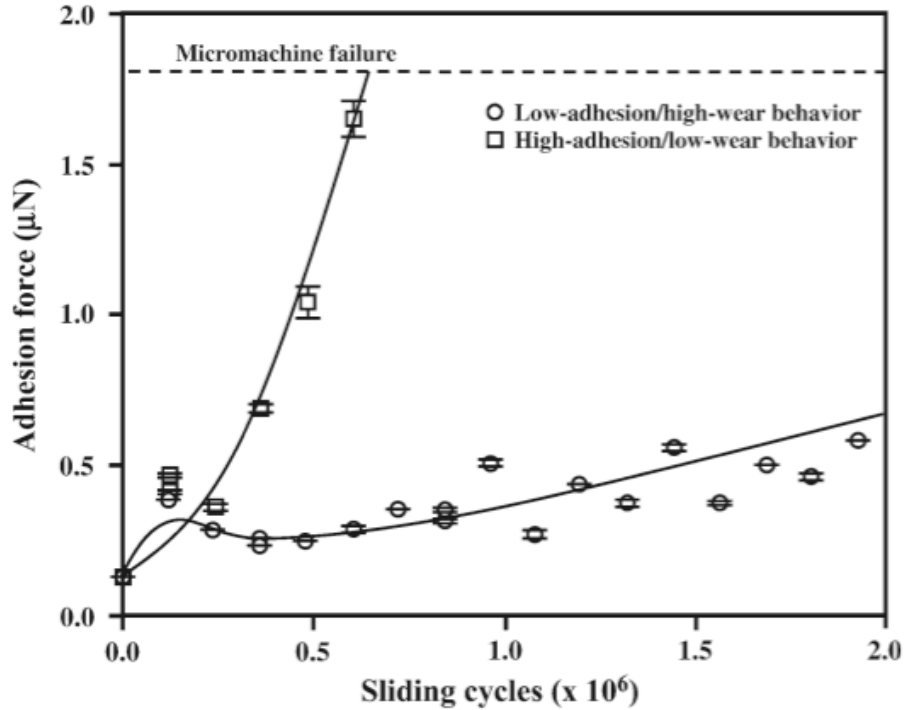


Figure 5.3 Adhesion force versus sliding cycles of two micromachines that demonstrated low-adhesion/high-wear behavior and high-adhesion/low-wear behavior (data points represent average values obtained from ten experiments, and error bars indicate one standard deviation above and below corresponding average values).

A. High-Adhesion/Low-Wear Behavior

Figure 5.3 shows the variation of the adhesion force with sliding cycles. In the case of high-adhesion/low-wear behavior, the adhesion force changed significantly during sliding. After a short run-in period, the adhesion force increased rapidly, eventually exceeding the available restoring force and causing the cessation of the micromachine movement. The adhesion force at the sidewall surface [Figure 5.4(a)] increased from an initial value of 0.13 to 1.65 μN after $\sim 6 \times 10^5$ sliding cycles. This represents an increase in the adhesion force by an order of magnitude. This trend is different from that observed in a previous study by Ashurst *et al.*²⁶ where static friction first decreased slightly and

then increased sharply resulting in failure. However, the formation of much more wear debris that caused surface roughening indicates that the prevailing friction and wear mechanisms in [26] were different from those in the present study, presumably due to significant differences in testing and environmental conditions. Similar sliding track topographies and rise of the interfacial adhesion force were observed with all of the micromachines that demonstrated high-adhesion/low-wear behavior. Despite this increase in the adhesion force, the SEM micrographs of the main shuttle shown in Figure 5.4 reveal almost unchanged sidewall surfaces that are free of wear debris. The sidewall surface shown in Figure 5.4(a) was subjected to $\sim 6 \times 10^5$ sliding cycles at 100 Hz. This sliding surface can be compared to the sidewall surface outside of the sliding track shown in Figure 5.4(b), which is typical of the as-fabricated sidewall surfaces. Even though the surface topographies shown in Figures 5.4(a) and (b) do not demonstrate discernible differences, a small amount of wear debris adhered to the tip of the loading shuttle can be observed in Figure 5.4(a).

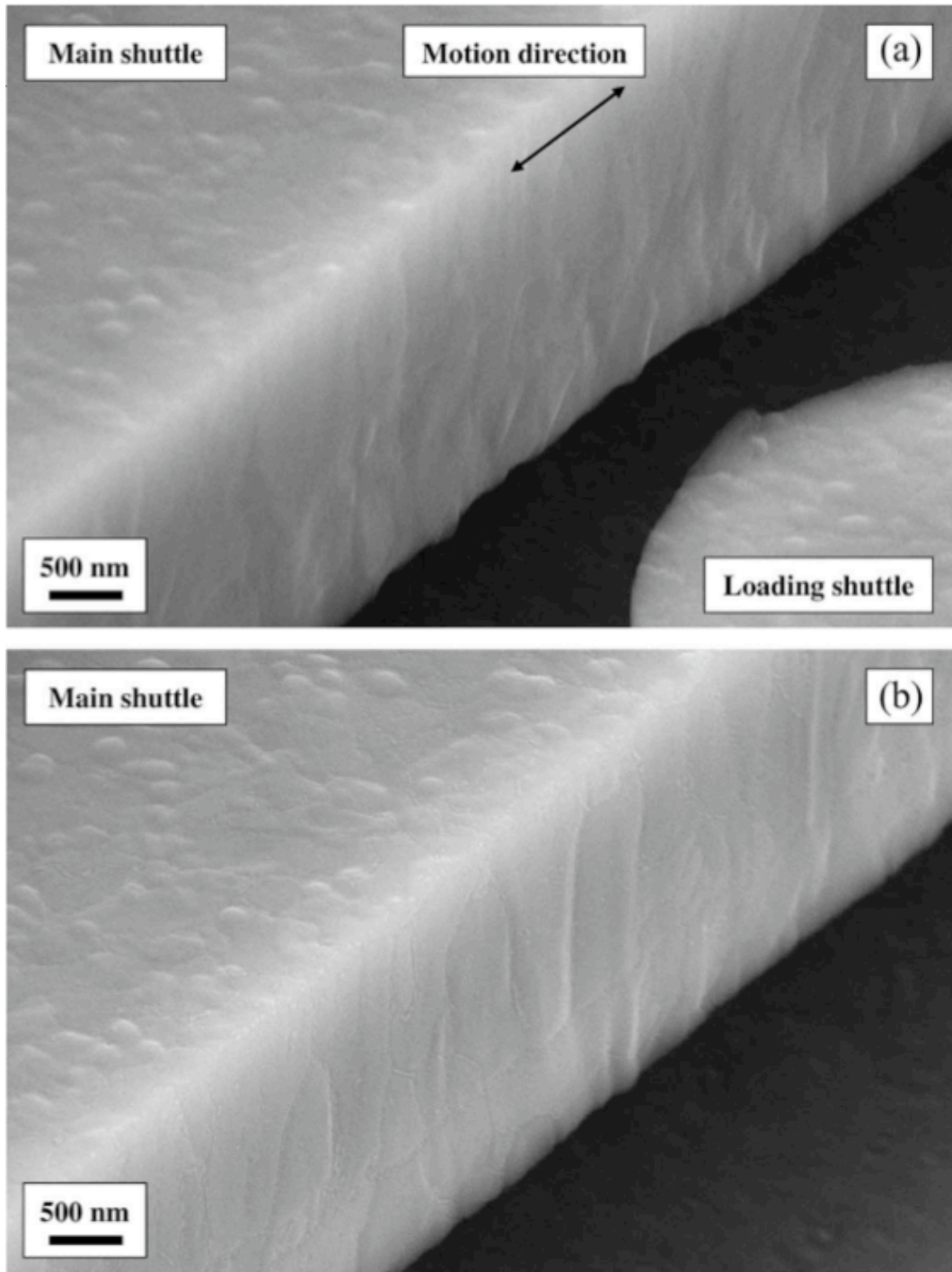


Figure 5.4. SEM micrographs of a micromachine that demonstrated high-adhesion/low-wear behavior showing (a) the sidewall surface of the oscillating main shuttle after $\sim 6 \times 10^5$ sliding cycles and (b) a region of the sidewall surface of the main shuttle outside the sliding track.

B. Low-Adhesion/High-Wear Behavior

Seven of the tested micromachines demonstrated small changes in sidewall adhesion force during sliding and visible wear debris. The increase of the adhesion force was significantly less pronounced than that in the experiments that did not yield any detectable wear debris. In this case, the adhesion force increased from an initial value of ~ 0.13 to $0.58 \mu\text{N}$ after sliding for $\sim 2 \times 10^6$ cycles at 100 Hz (Figure 4.3). This represents an increase in the adhesion force by a factor of ~ 4.5 compared to ~ 12.5 for high-adhesion/low-wear behavior.

Figure 5.5(a) shows a SEM image of the sidewall contact interface of a micromachine that exhibited low adhesion. The micrograph shows wear debris at the top surface of the main shuttle spread along the sliding direction, suggesting that some wear debris was forced out of the sliding interface on top of the main shuttle. This is attributed to the tendency for wear debris to be pushed upward during reciprocating sliding due to the slightly nonvertical sidewall surfaces. Figure 5.5(b) shows a SEM micrograph revealing the aggregation of smooth wear debris. The lack of significant plowing marks on the sidewall surface [Figure 5.5(a)] and the relatively low normal force indicate that the dominant wear mechanism was adhesion.

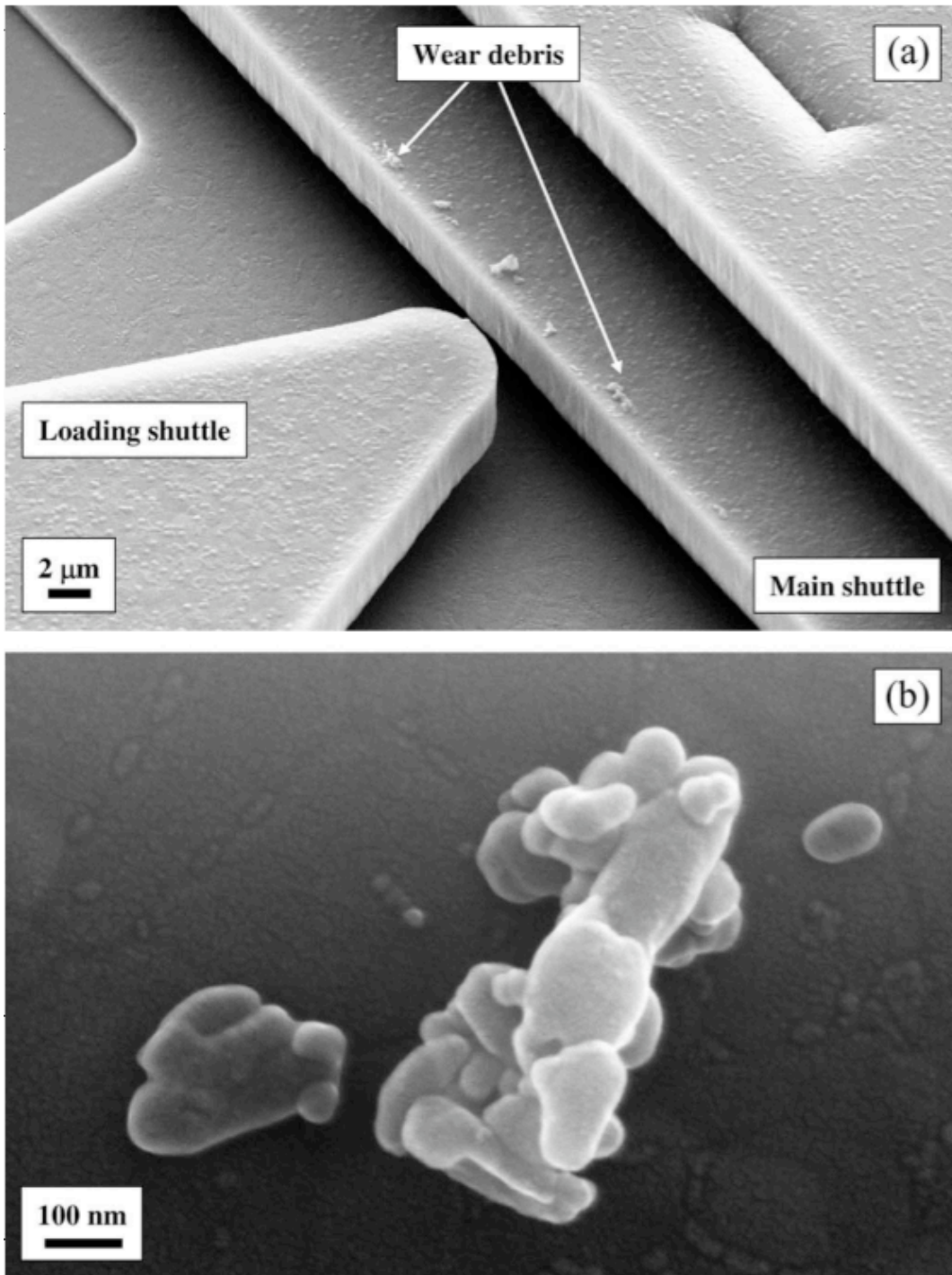


Figure 5.5 SEM micrographs of a micromachine that demonstrated low-adhesion/high-wear behavior showing (a) wear debris pushed out of the sliding track on top of the main shuttle and (b) agglomerates of very small wear debris.

Several of the micromachines that demonstrated low-adhesion/high-wear behavior also showed smeared material across the wear track. The SEM micrographs shown in Figure 5.6 provide evidence of material smearing at the sidewall surface in the case of low-adhesion/high-wear behavior. In this experiment, smearing was confined at the sidewall surface of the main shuttle, while that of the loading shuttle did not show material smearing. In all of the micromachines that exhibited low-adhesion/high-wear behavior and material smearing, this surface morphology was mainly observed only on one of the sliding surfaces. In addition, the area at the bottom of the sidewall surface of the main shuttle directly above the loading shuttle, shown in Figure 5.6(b), has been significantly worn off, most likely contributing to the large amount of wear debris generated by this micromachine.

TEM yielded further insight into both the smeared material shown in Fig. 5.6 and the wear debris shown in Figures 5.5 and 5.6. Figure 5.7(a) shows a bright-field TEM image and diffuse rings in the corresponding SAD pattern [inset of Figure 5.7(a)] of the smeared material. This TEM image (obtained from the region marked in Figure 5.6(a) without FIB thinning) and accompanying SAD pattern indicate that the smeared material is amorphous. The dark contrast in the smeared material is due to wear debris located either above or below the smeared material. This material is also amorphous, as evidenced by the SAD patterns of the individual agglomerates of wear debris.

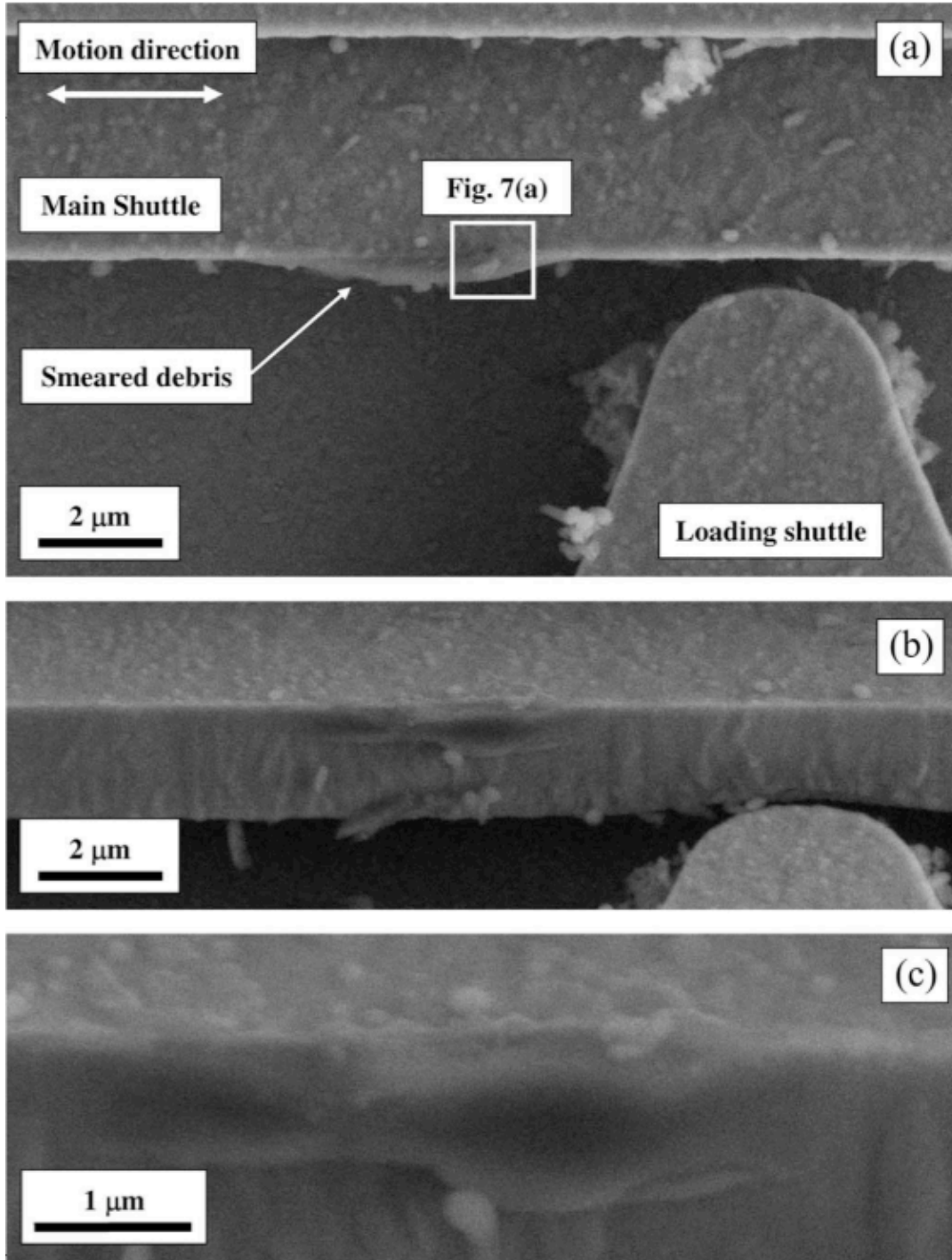


Figure 5.6 SEM micrographs of a micromachine that demonstrated low-adhesion/high-wear behavior showing [(a) and (c)] material smearing at the sidewall surface of the main shuttle and (b) wear debris formation, agglomeration, and smearing onto the sidewall surface [the section marked in (a) is shown in Figure 4.7(a)].

To further investigate the nature of wear debris, a TEM sample of the main shuttle and smeared wear debris was thinned down with the FIB to a thickness of ~350 nm. Figures 5.7(b) and (c), respectively, show a bright-field TEM image and an EFTEM oxygen map of the interface between the shuttle and the smeared material. Two polysilicon grains are visible on the left of both images, while the right half of each image shows smeared material. Although the smeared material contains some oxygen, a brighter oxygen band exists at the interface between the silicon grains and the smeared material [Figure 5.7(c)]. Despite the noise due to the relatively thick sample, the oxide film was estimated to be ~4 nm thick, consistent with previous thickness measurements of native oxide film at sidewall surfaces of devices produced by the SUMMiT V process²⁷. The demarcation of this post release silicon oxide film at this interface shows that the smeared material is not dominantly composed of silicon oxide. If the smeared debris consisted of oxidized silicon, it would have displayed a similar brightness as the silicon oxide layer at the interface.

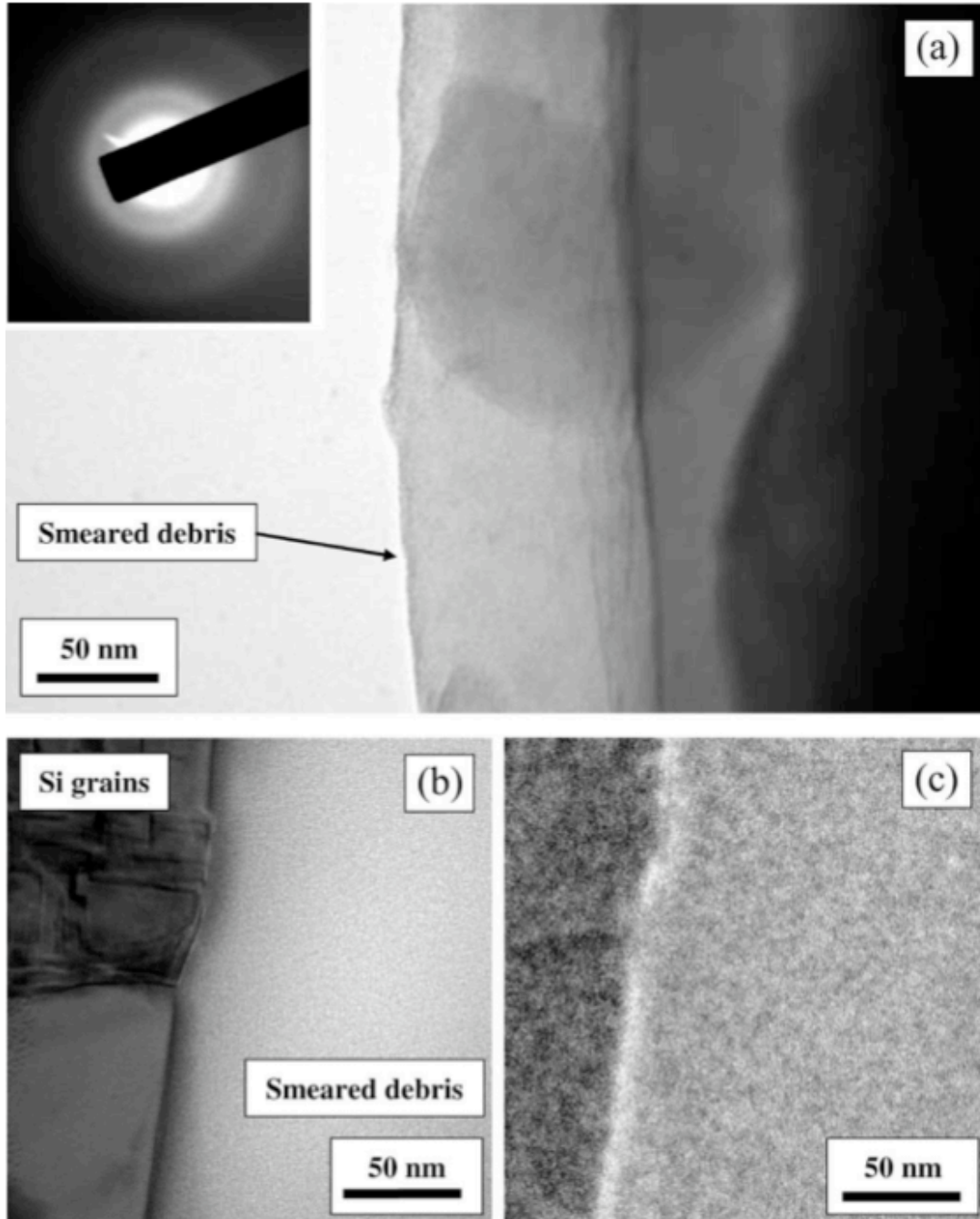


Figure 5.7. (a) Bright-field TEM image and SAD pattern of smeared debris, (b) bright-field TEM image of the interface between the main shuttle and smeared wear debris, and (c) corresponding oxygen map showing the presence of oxygen at the interface and to a lesser extent in the smeared wear debris (due to image drifting, (b) and (c) were obtained at a slightly different location).

Nanoprobe EDS was performed on various micromachine locations to determine the composition of smeared debris. The EDS results given in Table I indicate that the polysilicon grains consist mostly of silicon and traces of oxygen and carbon, while the smeared layer consists mainly of carbon. The small amount of Pt in the smeared material is attributed to residues of the protective Pt layers used in FIB thinning.

Table 5.1

CHEMICAL COMPOSITION OF WEAR DEBRIS AND BASE MATERIAL

Structure	Element (at%)				
	C	F	O	Pt	Si
Smeared Material	80	0	15	2.5	2.5
Base Material	3	2	2	0	95

It is noted that the percentages given in Table 5.1 can only be used for comparative measure and not for absolute identification. A typical error of $\pm 10\%$ of the measured value can be assumed for clearly visible peaks in the EDS spectrum. A similar analysis was performed on larger wear debris. Figure 5.8 shows a bright-field TEM image and an oxygen EFTEM map of (not thinned) wear debris. Unlike the smeared layer, these images reveal the formation of wear debris exhibiting high oxygen content throughout, suggesting that this debris most likely consists of silicon oxide.

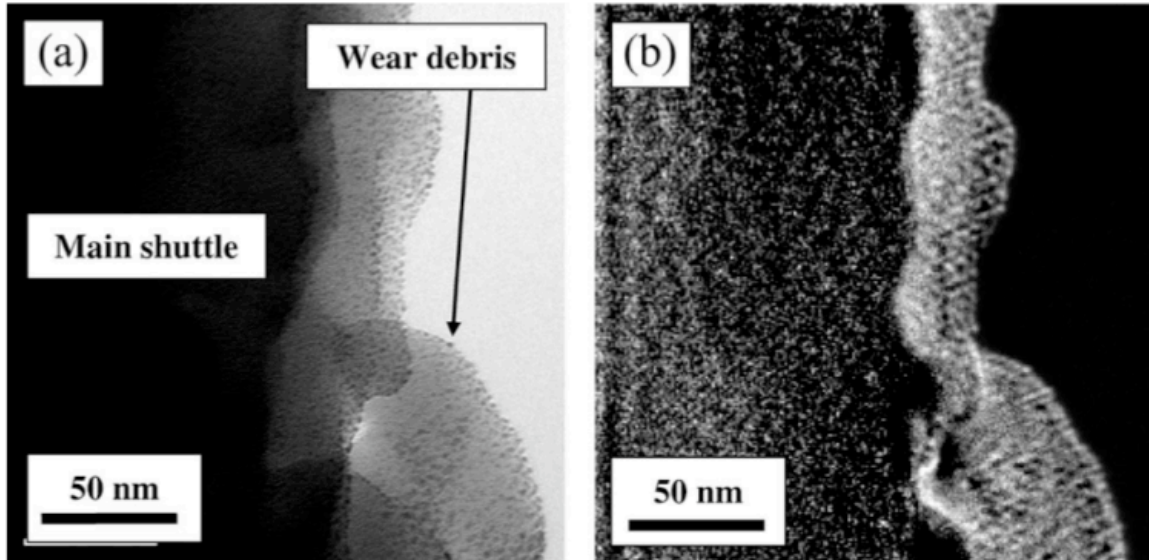


Figure 5.8 (a) Bright-field TEM image of the interface between the main shuttle and a layer consisting of wear debris and (b) corresponding oxygen map showing the presence of oxygen in the wear debris.

5.5 Discussion

The presented results provide insight into the tribological behavior of polysilicon micromachines operated in high vacuum under conditions of contact loading and sliding speed typical of MEMS devices. Specifically, the development of sliding wear and the evolution of the static adhesion force were correlated with the accumulation of sliding cycles and SEM/TEM investigations of the wear debris. The occurrence of two distinctly different adhesion/wear behaviors, despite the identical fabrication and testing conditions, suggests that both micromachine operation and type of dominant failure mechanism can be affected by several seemingly random factors, such as wear debris entrapment, accumulation, and smearing. In addition, a comparison of the observed wear behaviors with the abrasive wear found in previous studies^{14,15} shows that the dominant wear

mechanisms are also highly load dependent. The subtle details that can affect the tribological response appear to be magnified in the present study since the applied normal loads were less than those in [14] and [15] by one to two orders of magnitude.

A primary revelation of this investigation is the interdependence of amount of wear debris, static adhesion force, and micromachine lifetime. Microscopy and microanalysis results and adhesion force measurements indicated that the wear behavior of the rough polysilicon surfaces was affected by two primary factors: 1) changes in sidewall surface composition (surface energy) due to the removal of the organic monolayer coating and the native oxide film and 2) fluctuations in surface intimacy due to third-body wear debris trapped at the sliding interface, which increased the average surface separation distance and decreased the real contact area. TEM results provided additional insight into the chemical composition and microstructure of wear debris and showed that, in the case of low-adhesion/high-wear behavior, the smeared material mostly consisted of carbon, whereas the wear debris consisted of silicon oxide. It appears that agglomerates consisted of small oxide wear debris produced from the native oxide film and silicon wear debris from the subsurface that was fully oxidized upon exposure to the atmosphere because of its very small size. The carbon-rich material smeared onto the sidewall surface is believed to be an agglomerate of the organic coating material and may also contain some organic contaminant. Despite the seemingly large agglomeration of carbon-rich material, the amount of worn monolayer coating was estimated to be of a similar order of magnitude as the amount of smeared material. Assuming a monolayer coating thickness of 1.5 nm, a first-order calculation of the volume of coating covering a

surface area equal to that of the wear track yields a value of $\sim 0.05 \mu\text{m}^3$. This volume can be compared with the typical volume of smeared layers, such as those shown in Figures 5.6 and 5.7, estimated to be equal to $\sim 0.18 \mu\text{m}^3$.

Insight into each adhesion/wear behavior can be obtained by examining characteristic results. In the case of high-adhesion/low-wear micromachines, the tribological behavior was affected by changes in the surface composition. Since polysilicon surfaces exhibit much higher adhesion than those covered by an organic monolayer or native oxide film, the rapid increase in the adhesion force (Figure 5.3) can be associated with the increase in surface energy due to the removal of these layers by surface rubbing. The absence of any significant wear debris on the sliding surfaces is attributed to the very small amount of material removed from the sliding surfaces.

The tribological characteristics of low-adhesion/high-wear micromachines most likely resulted from changes in the degree of surface intimacy. EDS analysis revealed the removal of the organic monolayer, whereas material smearing suggested that the removed material could not escape from the sliding interface. Therefore, unlike high-adhesion/low-wear micromachines, the removal of the native oxide film and the organic coating exhibited a secondary effect on the wear behavior because the produced wear debris inhibited intimate surface interaction, hence resulting in a lower adhesion force. Further evidence of this effect can be obtained by contrasting the fluctuation levels in the two tribological behaviors. Figure 5.3 shows that the adhesion force of the low-adhesion/high-wear micromachine exhibited significant fluctuations after $\sim 10^6$ sliding cycles. The standard deviation in a particular set of five consecutive measurements

obtained after a given number of sliding cycles was similar to that observed previously (~ 10 nN). However, much greater variability between data points was found after $\sim 10^6$ sliding cycles. A first-order estimation of the deviation between successive measurements was made by calculating the difference between each measurement and average values from previous and subsequent measurements. By using this method, the average deviation of the adhesion force in the low-adhesion/high-wear experiments was found to be equal to 229 nN. This increase in the fluctuation of the static adhesion force after $\sim 10^6$ sliding cycles is attributed to third-body wear debris trapped at the sliding interface. Since both the distribution and the amount of wear debris play dominant roles in the development of the adhesion force, the standard deviation over the time range that each data point of Figure 5.3 was calculated is relatively low, while the fluctuation between data points is much higher. This hypothesis was confirmed by taking five adhesion force measurements at each of four different locations along the wear track for fixed number of sliding cycles. The standard deviation of the five measurements at one point (33 nN) was comparable to that of the data points shown in Figure 4.3 (~ 10 nN). However, significant variation in the adhesion force was observed from location to location along the wear track, as indicated by the high standard deviation of 189 nN, which is comparable to the scatter in the data observed after $\sim 10^6$ sliding cycles in the case of low-adhesion/high-wear behavior (Figure 5.3).

The existence of two profoundly different tribological behaviors in micromachines with identical fabrication processes indicates that the tribological behavior of MEMS contact interfaces is highly dependent on intricate details of the

surface topography, surface chemical structure, and wear debris distribution. At submicrometer scales, the ratio of the real-to-apparent contact area can be as low as 10^{-8} .²⁸ Therefore, while the microscale properties are nominally identical, the nanoscale properties can differ significantly from device to device. In view of the two dramatically different behaviors, it may be inferred that the wear behavior in the present study was dominated by nanoscale properties, rather than microscale surface properties. This is plausible because the sizes of asperities and wear debris are of order of magnitude comparable to those of the motion range and the wear track dimensions. Consequently, a few asperities can completely dominate the adhesion force measurement due to their unique size and/or chemical structure. Similarly, a small change in the number of interacting asperities can significantly modify the tribological behavior. Therefore, the observed micromachine-to-micromachine scatter can be attributed to the previous surface anomalies. Regardless of this type of experimental scatter, the wear experiments of this study revealed two significantly different behaviors. This implies that, depending on the particular MEMS application, the prevailing wear mechanisms may lead to unique modes of failure. For example, micromachines exhibiting high-adhesion/low-wear behavior would most likely fail in static adhesion mode when the adhesion force exceeds the available restoring force. Alternatively, micromachines demonstrating low-adhesion/high-wear behavior will be expected to fail due to the formation of wear debris. The evolution and agglomeration of wear debris at the contact interface can be particularly detrimental in electrical devices where intimate conductive contact is critical to effective operation (e.g., microswitches).

These two distinct tribological behaviors and associated failure mechanisms present major obstacles in the reliability of contact-mode MEMS devices. Deposition of thin films and surface treatments that can prevent these behaviors are therefore of paramount importance. Even if a certain degree of tolerance for wear debris exists, such as in the absence of an electrical conductance requirement, maintaining a low adhesion force may be critical to the effective operation of a particular device. Such a design requires a robust or self-replenishing coating that can prevent significant changes in surface composition despite the generation of wear debris. Alternatively, a design with increased tolerance for a high adhesion force due to the high stiffness of the mechanical suspension (e.g., inertial sensors) may exhibit a small tolerance for wear debris due to the electrical activation of the device. Under these circumstances, more robust tribological coatings must be developed with a proclivity toward high-adhesion/low-wear tribological behavior.

5.6 Conclusion

A special surface micromachine was used to examine the adhesion and sliding wear behavior of polysilicon MEMS operated in high vacuum. The focus in this investigation was on wear phenomena inherent to sidewall contact interfaces. Micromachines from the same batch process were tested in high vacuum under controlled contact load and reciprocating sliding conditions typical of MEMS devices.

Several of the micromachines exhibited high-adhesion/low-wear behavior, characterized by a nanoscale adhesive wear process (undetectable in the SEM) that resulted in the rapid increase of the interfacial adhesion force with the accumulation of

sliding cycles. The remaining micromachines demonstrated low-adhesion/high-wear behavior, characterized by a microscale wear process that produced nanometer-sized wear debris. This small debris was rolled smooth between the sliding surfaces, eventually forming agglomerates of several hundred nanometers in size consisting of oxide debris or carbon-rich layers smeared over portions of the sliding track. The increase in the adhesion force of these micromachines was much less pronounced compared to the other type of tribological behavior. This is attributed to third-body wear debris trapped at the sliding interface that inhibited intimate surface contact by increasing the relative surface separation distance.

Wear of polysilicon micromachines is highly dependent on the evolution of the surface topography and changes in the surface chemical composition occurring during sliding. This dependence manifests itself in several behaviors, such as cycle-to-cycle and along the wear track variations in the adhesion force, material smearing mainly on one of the sliding surfaces, and development of agglomerates of oxide wear debris. The evolution of wear at MEMS contact interfaces plays a dominant role in determining micromachine lifetime. Nanoscale wear may increase the surface energy through the removal of the native oxide film, organic monolayer coating, and any adsorbed contaminant, leading to the cessation of the micromachine oscillation. Although third-body wear debris may extend the operation life by preventing intimate surface contact, wear debris entrapment and agglomeration at the sliding interface could be detrimental to the device functionality. This is particularly important in contact-mode applications, such

as microswitches, where intimate surface contact is essential, and micromirrors, where displaced debris can interfere with the optical performance.

5.7 Acknowledgements

Authors S. J. Timpe and D. A. Hook would like to thank Sandia National Laboratories, Albuquerque, NM, for summer student intern support and the National Center for Electron Microscopy, Lawrence Berkeley National Laboratory, for using the microscopy facilities.

REFERENCES

- [1] W. M. Zhang and G. Meng, *Microsyst. Technol.*, vol. 12, no. 4, pp. 283–292, 2006.
- [2] J. Lampen, S. Majumder, R. Morrison, A. Chaudhry, and J. Maciel, *Int. J. RF Microw. Comput.-Aided Eng.*, vol. 14, no. 4, pp. 338–344, 2004.
- [3] A. Jain and H. Xie, *Sens. Actuators A, Phys.*, vol. 130/131, pp. 454–460, 2006.
- [4] D. M. Tanner, J. A. Walraven, L. W. Irwin, M. T. Dugger, N. F. Smith, W. P. Eaton, W. M. Miller, and S. L. Miller, *Proc. IEEE Int. Rel. Phys. Symp.*, San Diego, CA, 1999, pp. 189–197.
- [5] S. T. Patton, W. D. Cowan, and J. S. Zabinski, *Proc. IEEE Int. Rel. Phys. Symp.*, San Diego, CA, 1999, pp. 179–188.
- [6] S. T. Patton and J. S. Zabinski, *Tribol. Int.*, vol. 35, no. 6, pp. 373–379, 2002.
- [7] U. Beerschwinger, D. Mathieson, R. L. Reuben, and S. J. Yang, *J. Micromech. Microeng.*, vol. 4, no. 3, pp. 95–105, 1994.

- [8] R. Bandorf, H. Lüthje, C. Henke, J. Wiebe, J.-H. Sick, and R. Küster, *Surf. Coat. Technol.*, vol. 200, no. 5/6, pp. 1777–1782, 2005.
- [9] B. Bhushan, T. Kasai, G. Kulik, L. Barbieri, and P. Hoffmann, *Ultramicroscopy*, vol. 105, no. 1/4, pp. 176–188, 2005.
- [10] K. Komvopoulos, *Wear*, vol. 200, no. 1/2, pp. 305–327, 1996.
- [11] D. C. Senft and M. T. Dugger, *Proc. SPIE*, vol. 3224, pp. 31–38, 1997.
- [12] M. P. de Boer, J. M. Redmond, and T. A. Michalske, *Proc. SPIE*, vol. 3512, pp. 241–250, 1998.
- [13] E. E. Flater, A. D. Corwin, M. P. de Boer, and R. W. Carpick, *Wear*, vol. 260, no. 6, pp. 580–593, 2006.
- [14] D. H. Alsem, E. A. Stach, M. T. Dugger, M. Enachescu, and R. O. Ritchie, *Thin Solid Films*, vol. 515, no. 6, pp. 3259–3266, 2007.
- [15] D. H. Alsem, M. T. Dugger, E. A. Stach, and R. O. Ritchie, *J. Microelectromech. Syst.*, vol. 17, no. 5, pp. 1144–1154, 2008.
- [16] S. J. Timpe and K. Komvopoulos, *J. Microelectromech. Syst.*, vol. 14, no. 6, pp. 1356–1363, 2005.
- [17] A. Lumbantobing and K. Komvopoulos, *J. Microelectromech. Syst.*, vol. 14, no. 4, pp. 651–663, 2005.
- [18] S. J. Timpe and K. Komvopoulos, *J. Microelectromech. Syst.*, vol. 15, no. 6, pp. 1612–1621, 2006.
- [19] M. S. Rodgers and J. J. Sniegowski, *Tech. Dig., Solid-State Sens. Actuators Workshop*, Hilton Head Island, SC, 1998, pp. 144–149.

- [20] M. G. Hankins, P. J. Resnick, P. J. Clews, T. M. Mayer, D. R. Wheeler, D. M. Tanner, and R. A. Plass, *Proc. SPIE*, vol. 4980, pp. 238–247, 2003.
- [21] W. C. Tang, Ph.D. dissertation, Univ. California, Berkeley, CA, 1990.
- [22] C. D. White, R. Xu, X. Sun, and K. Komvopoulos, *Proc. SPIE*, vol. 4980, pp. 63–74, 2003.
- [23] W. C. Tang, M. G. Lim, and R. T. Howe, *J. Microelectromech. Syst.*, vol. 1, no. 4, pp. 170–178, 1992.
- [24] S. J. Timpe, D. A. Hook, M. T. Dugger, and K. Komvopoulos, *Sens. Actuators A, Phys.*, vol. 143, no. 2, pp. 383–389, 2008.
- [25] L. A. Giannuzzi and F. A. Stevie, Eds., *Introduction to Focused Ion Beams: Instrumentation, Theory, Techniques and Practice*. New York: Springer-Verlag, 2005.
- [26] W. R. Ashurst, M. B. J. Wijesundara, C. Carraro, and R. Maboudian, *Tribol. Lett.*, vol. 17, no. 2, pp. 195–198, 2004.
- [27] D. H. Alsem, B. L. Boyce, E. A. Stach, and R. O. Ritchie, *Sens. Actuators A, Phys.*, vol. 147, no. 2, pp. 553–560, 2008.
- [28] M. P. de Boer, J. A. Knapp, T. A. Michalske, U. Srinivasan, and R. Maboudian, *Acta Mater.*, vol. 48, no. 18/19, pp. 4531–4541, 2000.

Chapter 6

Vapor-phase lubrication at ultra low partial pressures of ethanol

D. Adam Hook, Brendan P. Miller, Brian M. Vlastakis, Michael T. Dugger and

Jacqueline Krim

Submitted: Langmuir

Abstract - This paper reports a study of the lubricating properties of sub-saturation pressures of ethanol, pentanol and trifluoroethanol vapors adsorbed on a Micro-Electro-Mechanical System (MEMS)-based test device in a vacuum environment. The device employed a capacitive ringdown technique specifically designed for friction measurements, and was situated within an ultrahigh vacuum chamber that was also equipped with optical monitoring capabilities. Devices were observed to fail rapidly in both air and alcohol-free vacuum environments. They remained operational however for indefinitely long time periods for partial pressures in vacuum exceeding very low values ($P/P_{\text{sat}} = 2 \times 10^{-5}$), and for very long residual periods after the gas was removed. The presence of a Self-Assembled Monolayer (SAM) enhanced this effect, consistent with the SAM acting as a lubricant reservoir. In contrast, pentanol lubrication was observed only for vapor pressures exceeding $P/P_{\text{sat}} = 0.08$, and trifluoroethanol vapors had no lubricating effects whatsoever. Device lifetimes were observed to be only weakly correlated with friction coefficients, but strongly correlated with adsorbed film mobility levels and slip times. It is therefore observed that even very low levels of lubricious

mobile adsorbates can prolong device lifetimes: Their mobility may be enabling adsorbate accumulation near the contact in quantities sufficient to lubricate it.

Nanoscale Lubrication, NEMS, MEMS, Friction, Alcohol, Surface Mobility

6.1 Introduction

Friction and its consequences are of great concern from both a national security and quality-of-life point of view, and the economic impact is massive.¹ Lubrication schemes for many macroscopic applications have been solved, but an era of science and engineering is emerging where control of mechanical and electrical systems at the atomic level will be required.^{1,2} Traditional macroscopic approaches to lubrication are ineffective for nano- and micro-scale applications.¹ Indeed, one of the most promising and compelling microscale applications, the on-chip MEMS microturbine for electrical power generation, remains stalled by air bearing failures associated with friction and wear.³

A number of elegant mechanical approaches have been proposed for controlling atomic scale friction,^{1,4-6} including careful orientation of the counterface materials in an atomically incommensurate fashion,^{1,4} reduction of normal forces and/or sliding speeds,⁵ and application of externally imposed vibrations at system resonant modes.⁶ Despite major recent advances in the reliable production of MEMS devoted to fundamentals of friction,^{7,8} these approaches have been investigated almost exclusively by means of atomic force microscopy.²

We focus here on the impact of mobile adsorbed molecules on atomic-scale friction, utilizing MEMS devices designed specifically for friction studies. Adsorbed films, whether intentionally applied or present as trace levels of physisorbed contaminants, are ubiquitous at virtually all surfaces.^{1,9,10} Their impact on atomic-scale friction is expected to be profound. Low levels of mobile adsorbed atoms, for example, have been predicted to increase friction through migration of atoms to locations that most effectively lock opposing surfaces together.¹¹ This effect could potentially neutralize, if not totally negate, superlubricity effects associated with incommensurate contacts.^{1,4}

Submonolayer coverages of alcohols fail to lubricate macroscopic contacts¹² and it has been hypothesized that diffusion related displacement of particles out of the contact zones is responsible for this.^{12,14} Diffusive mobility of an adsorbate however both enhances a film's ability to be displaced from a contact, as well as its ability to replenish areas scratched free of the lubricant. Further studies must therefore be conducted to confirm or dispute this hypothesis.^{2,14,15} At the scale of MEMS,¹³ it is known that submonolayers of pentanol fail to lubricate, while pentanol monolayers extend device lifetimes indefinitely. Diffusion may play a role here as well. A chemically reacted layer, for example, has been observed during chemical analysis of macroscopic silicon contacts^{16,17} lubricated by pentanol films, with recent studies suggesting that complex oligomer formation is not the primary mechanism associated with pentanol's lubricity.¹⁷ Tribochemical reaction products detected in the contact regions instead appear to be linked to wear mechanisms associated with insufficient lubricant supply via the gas phase or surface diffusion.¹⁷

Surface coverage and mobility of adsorbed film particles can be probed with a Quartz Crystal Microbalance (QCM), yielding “slip times” t that are inversely proportional to friction^{1,18} and directly proportional to film diffusivity.¹⁹ Physisorbed films typically exhibit slip times on the order of ns, while more strongly bound chemisorbed layers are characterized by ps.¹ Picosecond scale slip times and zero slippage have been linked, respectively, to success and failure of monolayer and multilayer lubricants at the macroscale,²⁰ and also to film displacement by single asperity contacts.¹⁵

6.2 Experimental Details and Results

For the present study, friction, wear, and device lifetimes were measured in a custom vacuum chamber (Figure 6.1a) on silicon MEMS friction test devices with perfluorodecyltrichlorosilane (PFTS) SAM layers (Figure 6.1b) exposed to sub-monolayer coverages of ethanol and related alcohols,²¹ and compared to QCM measurements of their coverage and mobility on identical SAM surfaces.

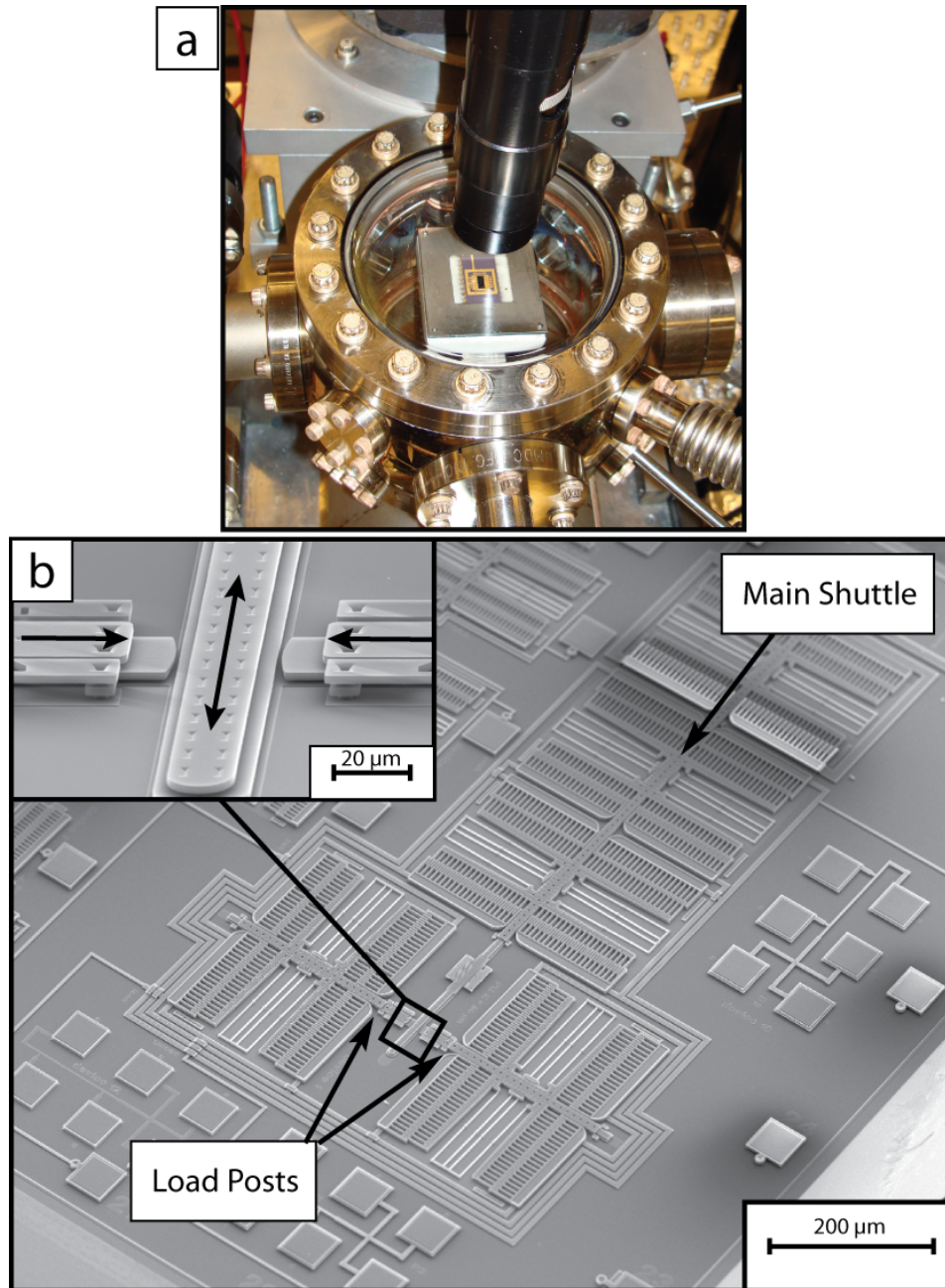


Figure 6.1 Custom Chamber and Measurement Device A) Custom vacuum chamber with a test device mounted in the center prepared for operation. B) Scanning electron micrograph of the entire test structure with the main shuttle and loading posts indicated. The inset is a zoomed in image of the load and main shuttles with direction of motion indicated.

Ethanol was selected as the primary candidate for these studies based on the well-documented nature of its macroscopic lubricity above monolayer coverages,¹² and the fact that alcohols in general are promising candidates for both MEMS^{13,18} and macroscopic^{12,22} applications. Ethanol has also been mentioned in passing within the context of microturbines, where it was reported that application of ethanol liquid increased the microturbine operation velocity by several orders of magnitude, presumably due to a reduction in friction.²³

MEMS device lifetimes were monitored with a Charge Coupled Device (CCD) camera connected to a video recorder.²¹ Device “lifetime” was defined as either the time (cycle number) at which device motion ceased or at the onset of wear.⁸ A load of 500 nN was selected so that the test structures would cease to oscillate before a significant number of wear particles were generated.⁸ The devices were operated in a custom built chamber, capable of an ultimate pressure of 5×10^{-9} Torr. The chamber was equipped with a Masstorr FX residual gas analyzer (RGA) to measure residual gas components present in the chamber, two Baratron capacitance manometers to measure pressures from atmosphere to 1 millitorr, and a cold cathode gauge to measure pressures from 1 millitorr to 1×10^{-9} Torr. Before each test the capacitance manometers were zeroed at base vacuum pressure and although the cold cathode gauge pressure measurement is gas species dependant the overlap with the one millitorr ranged Baratron head (gas independent) showed good agreement as did the overlap between the 1 millitorr Baratron head and the 10 millitorr head. Vacuum was established with a dry mechanical pump backed turbomolecular pump and an ion pump. Systematic errors and artifacts are

virtually eliminated by the cleanliness of our vacuum chamber and the purity of the substances we are working with. Extreme care was taken in the preparation of the MEMS chip itself, the conditioning of the vacuum chamber and nitrogen lines, and the purification of the ethanol, TFE, and pentanol. The lines connecting the 99.999% nitrogen lecture bottle were baked, pumped, and purged until after a purge and pump cycle the H₂O peak in the residual gas signal remained virtually constant at 5×10^{-10} Torr. The ethanol, pentanol, and trifluoroethanol were all individually purified by a freeze-pump-thaw method while connected to the chamber, which can be found here.¹⁸ With residual gas analysis it was determined that partial pressures of water, oxygen, nitrogen, and heterogeneous hydrocarbons were many orders of magnitude below that of the ethanol, TFE and pentanol. Prior to device insertion into the vacuum chamber a base pressure was established of 5×10^{-9} Torr such that there could be no hysteresis between experiments. Therefore the response of the MEMS device was a direct result of either the ethanol, pentanol, or trifluoroethanol vapor.

MEMS device friction coefficients were measured using a capacitive ringdown technique similar to that used to measure damping in quartz crystal microbalances²⁴. In this technique a sensing capacitor made up of isolated comb fingers interlaced with grounded fingers on the main shuttle was biased by a constant voltage V_{bias} , the main shuttle was displaced, the loading protrusions were brought into contact at 50 nN of normal load per side, and finally the main shuttle was released and allowing it to oscillate at its resonant frequency. There is a direct relationship between the velocity of the oscillating shuttle and the current flowing into and out of the sensing capacitor given by

$$i = C_{sense} V_{bias} v \quad (6.1)$$

where i is the current flowing into and out of the sense capacitor, V_{bias} (=9.515 V) is the constant voltage applied to the sense capacitor, C_{sense} ($=3.363 \times 10^{-9}$ F/m) is the capacitance per unit length of the sense capacitor's comb fingers, and v is the velocity of the main shuttle. Therefore a measure of the current flowing into and out of the sensing capacitor's comb fingers at a constant voltage gives a measure of the velocity of the main shuttle. A relationship between the change in the peak velocities and the force of friction is given by an analysis of the equations of motion of the main shuttle given by

$$\frac{d^2x}{dt^2} + \gamma \frac{dx}{dt} + \frac{F_f}{m} \text{sgn}\left(\frac{dx}{dt}\right) + \omega_0^2 x = 0 \quad (6.2)$$

where ω_0 is the resonant frequency of the main shuttle, γ is the gas damping constant, F_f is the force of friction, m is the mass of the shuttle, and $\text{sgn}(dx/dt)$ is a function that represents the friction force opposing the direction of motion ($\text{sgn}(dx/dt) = 1$ if $dx/dt > 0$ and $\text{sgn}(dx/dt) = -1$ if $(dx/dt) < 0$). The peak velocities are determined by a recursive solution to the given equation of motion

$$v_{n+1} = -v_n e^{\frac{\gamma}{\omega_0} \pi} - (-1)^n \delta \quad (6.3)$$

where n is the half cycle number, v_n is the n th half cycle peak velocity, ω_0 and γ are defined above, and δ is the parameter that defines the linear decrease in velocity per half cycle due to coulomb friction. The relationship between δ and the force of friction is given by

$$F_f = \frac{\delta}{2\sqrt{\omega_0^2 - \gamma^2}} e^{\frac{\gamma}{\omega_0} \left(\frac{\pi}{2} - \arctan\left(\frac{\gamma}{\omega_0}\right) \right)} \quad (6.4)$$

therefore the force of friction is determined by a fit to the peak values of current measured per half cycle of oscillation. Thus the rate of the main shuttles velocity decrease provides a direct and quantitative measure of the force and form of the friction. The kinetic friction measurements were performed on a single device by taking the average of 5 different measurements. An example ringdown data set can be found in figure 6.2a

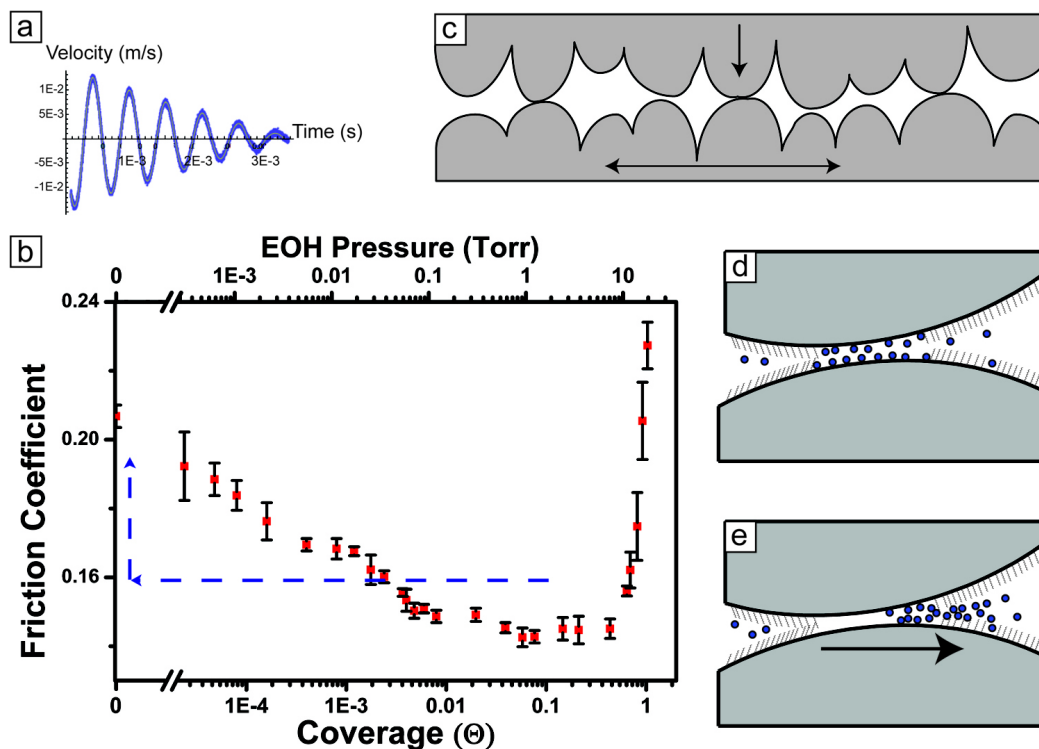


Figure 6.2 Ultra Low Coverage Ethanol Lubrication. Friction coefficient measurements are made by a ringdown technique with a sample set of data shown in (a). At significantly low ethanol vapor pressures an effect on the coefficient of kinetic friction in our test devices can be seen (b). A distinct decrease can be seen even at a coverage of 2.5×10^{-4} ($P/P_0 = 2 \times 10^{-5}$) of a monolayer. (c) Depicts schematically a cross section of the contact area of our MEMS test structures. The roughness gives a real contact area of approximately $2 \times 10^{-15} \text{ m}^2$. A coverage of 2.5×10^{-4} implies as little as 5 molecules in the contact (ethanol molecular area 12 square angstroms). The actual coverage in the contact area could be increased by damage to the self-assembled monolayer increasing ethanol adsorption in those areas (d), or 2D ethanol islands diffusing in, and subsequently being trapped as the device moves in one direction (e).

Measurements were performed in equilibrium by waiting 5 minutes between pressure increase and experimentation, so film coverage levels were controlled by the surrounding vapor pressure^{9,10} and not the exposure time. Remarkably, the lowest pressure at which device lubrication occurred, 1 mTorr, was two orders of magnitude lower than that at which the QCM could detect uptake! Irrespective of whether a SAM

was initially present, beginning at 1 mTorr devices could be operated for over 6×10^7 cycles (3.5 days at 200Hz) without any evidence of wear, based on scanning electron microscopy images with 5-10 nm resolution.

At the chamber's base pressure of 5×10^{-9} Torr, no uptake was detected and the coefficient of friction was approximately 0.21. This measurement was taken over a long baseline (approximately 30 minutes) to show no variation due to deposition from the walls of the vacuum chamber itself. As ethanol was leaked into the chamber, the coefficient of friction first began to drop at 0.1 mTorr and reached a minimum of ~ 0.14 for the pressure range 100-500 mTorr, corresponding to ethanol film coverage of 0.01 to 0.5 monolayers as measured by the QCM. (Figure 6.2b) As the coverage approached one monolayer, the coefficient of friction rose dramatically, attributable to an increase in adhesion forces due to capillary film formation. Reducing the chamber pressure back to 1×10^{-8} Torr did not immediately cause the friction coefficient to return to its initial value of ~ 0.21 . (blue line in Figure 6.2b). Backfilling with pure nitrogen (99.999%) was required for this to occur, indicating that ethanol was still physisorbed to the surface after the ethanol vapor was reduced. Vacuum chamber conditioning with pure nitrogen is well known in the ultra high vacuum community. Nitrogen displaces physisorbed contaminants by kinetic processes from vacuum chamber walls and carries them away as the nitrogen gas is removed from the chamber.

Open surface coverages below the QCM detection limit of 0.01 monolayers were estimated by extrapolation of the vapor pressure isotherm²¹ (Figure 6.5 Supplemental Section) to be 2×10^{-4} monolayers at 1 mTorr. This was consistent with independent

measurements of ethanol adsorption levels on unconfined planar substrates.²⁵ Below 0.1 mTorr, no lubricating effect was detected, and for 0.1 – 1 mTorr (estimated coverage: 2×10^{-5} to 2×10^{-4} monolayers), the devices ceased operating after 100 – 20,000 cycles, with a large variation from measurement to measurement. To place this in context, 1 mTorr of ethanol is only 0.002 % of the bulk saturation pressure (45 Torr) of ethanol, compared to the 8% P/P_{sat} and monolayer coverages required for successful lubrication of devices in partial pressures of pentanol in nitrogen.¹³

6.3 Discussion

Mechanisms for the observed lubrication will now be discussed. Apparent MEMS contact pressures (<250 MPa) are typically much lower than those of AFM (1-10 GPa) and macroscale (0.5-2 GPa) contacts.^{14,16} As the two sidewall surfaces approach one another, only a few of the asperities actually come into contact, (Fig. 6.2c) leading to a real contact area of approximately 2×10^{-15} m² at 500 nN applied load. Failure is believed to begin with wear that is initiated through intimate contact between Si-Si or SiO₂-SiO₂ molecules across the interface.^{8,26} A coverage of 2.5×10^{-4} monolayers over this area results in only approximately 5 molecules of ethanol present per contact, assuming a uniform distribution of adsorbed molecules. Clearly this does not lock the surfaces together, as has been theorized for small physisorbed spherical particles.¹¹ Submonolayers have been observed numerically to reduce friction in other systems by simply separating the contacting surfaces.²⁷ However since the models were of different materials, more intensive modeling of this particular system would be needed to determine whether

simple separation plays a role. In addition, the trapping of mobile particles by SAM defects (presumably very few in number) or broken bonds, acts to “repair” SAM locally and prevent Si-Si contact in each rubbing cycle.²⁸

An accumulation of molecules in the confined regions of the contact is highly likely on account of stronger binding strengths, but not capillary condensation at these low pressures. The adsorption isotherms used to determine coverage in our MEMS experiments were performed on flat quartz crystal microbalances coated in PFTS. However the actual MEMS surface has an rms roughness of approximately 20 nm. The valleys in the surface can have cylindrical pores of approximately 1nm radius. Also contacting surfaces and imperfections in the self-assembled monolayer can create pore-like surfaces of similar radius. In these instances a higher coverage would be present on the surface than would be seen on the idealized QCM surface due to capillary condensation. Here pore radii of 1 nm and 2 nm were used to calculate the pressure at which capillary condensation for each of our lubricants tested. The Kelvin equation shown here:

$$\ln \frac{P}{P_0} = \frac{2\gamma V_m \cos \theta}{rRT} \quad (6.5)$$

describes the relationship between the pressure of a surrounding vapor and the minimum pore size required for capillary condensation.²⁹ Where P_0 is the vapor pressure, γ is the surface tension of the bulk liquid, V_m is the molar volume, θ is the contact angle between the liquid and the adsorbing surface, R is the gas constant, T is the temperature in Kelvin, and r is the pore radius. In all of the cases a temperature of 300 K was used. Table 6.1 lists the physical properties of three test lubricants ethanol (EOH), pentanol, and

trifluoroethanol (TFE). The contact angle measurements were made in single crystal silicon (100) wafers coated with PFTS.

Table 6.1. List of physical properties of the test lubricants for use in the Kelvin equation. The contact angles were estimated by standard goniometry techniques on silicon (100) wafers coated in PFTS.

Substance	Surface Tension (N/m)	Molar Volume (m ³ /mol)	Contact Angle	Vapor Pressure (Torr)
EOH	0.0221	5.87E-5	40	45
Pentanol	0.0257	1.087E-4	35	2
TFE	0.0211	7.239E-5	15	60

Table 6.2 lists the results of the Kelvin equation analysis at the two pore radii. As can be seen from the table the pressures at which capillary condensation would occur are orders of magnitude larger than the pressures at which long lifetimes were seen for ethanol.

Table 6.2. Results of the Kelvin equation calculation of the pressure at which capillary condensation would occur for pores of 1nm and 2nm radii. The molecular radii were calculated via the molar volume and represent a maximum value.

	P ₀ (Torr)	r _{molecule}	P/P ₀ (1nm)	P _{1nm} Torr	P/P ₀ (2nm)	P _{2nm} Torr
EOH	45.0	0.23 nm	0.451	20.3	0.671	30.2
Pentanol	2.00	0.28 nm	0.160	0.319	0.400	0.799
TFE	60.0	0.25 nm	0.306	18.4	0.553	33.2

Therefore, the results of the experiment cannot simply be attributed to a higher than estimated surface coverage due to capillary condensation. Moreover capillary condensation around contacting asperities would result in a dramatic increase in adhesion force due to the Laplace pressure leading to an increase in the apparent coefficient of friction.²⁵ This effect was only observed in the coefficient of friction measurement as the coverage reached one monolayer.

Submonolayer cluster and island diffusion levels, although dramatically size dependent, are generally much higher than either their constituents or full monolayers,^{18,19,30-33} and such islands readily diffuse into a contact where they could become trapped long enough to lubricate it. In fact for ethanol islands the size of the real contact area ($2 \times 10^{-15} \text{ m}^2$) the diffusion rate is $1.14 \times 10^{-8} \text{ m}^2/\text{s}$ calculated by the method in ref. 18. At a reciprocating rate of 200Hz the area covered by an island that size would be $5.7 \times 10^{-11} \text{ m}^2$, 4 orders of magnitude larger than the contact area, virtually assuring that an island would have ample time to return to the depleted area before the sliding contact returned. For smaller islands the diffusion rate is increased. Mobility is likely to decrease dramatically within the confinement of the contact, particularly if a chemical reaction were to occur there. The paradox here is that mobile islands both easily diffuse towards but are easily pushed away from the contact.^{15,18} (Figure 6.2d, e) “Ballistic” behavior of sliding clusters away from a contact upon being struck by a moving asperity is key to understanding this issue, and is just beginning to be explored theoretically.³¹

With the exception of 3D capillary condensation, the aforementioned explanations are closely associated with the mobility of the adsorbed molecules. To test the various

hypotheses, we performed measurements on trifluoroethanol (TFE), which has similar capillary effects as ethanol (Table 6.2), but is pinned and immobile on PFTS,¹⁸ (the SAM layer utilized throughout this study) and pentanol, which exhibits little mobility on PFTS below one monolayer¹⁸ while exhibiting much stronger capillary condensation effects.²¹ TFE and ethanol show almost identical adsorption isotherms. Also there is little difference between all three molecule's vapor flux rate at a given pressure.²¹ They should therefore exhibit similar ability to replenish from the vapor phase. The results are presented in Figure 6.3, which summarizes the observations in terms of the atomic scale slip time t , reported in [18] for coverages above 0.5 monolayer.

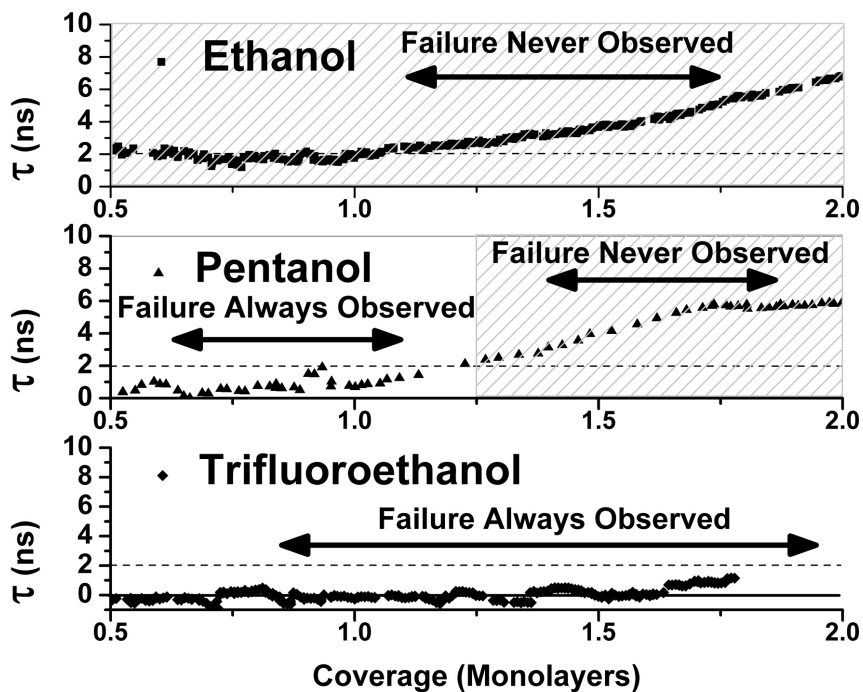


Figure 6.3 Lifetimes of Devices in Vapors of Alcohols. Lifetimes of devices were measured as a function of vapor pressure for various alcohols and compared to the slip time of the alcohols on a PFTS SAM covered surface reported in Ref.[18]. Devices in ethanol vapor never failed and ethanol slips significantly on PFTS. Devices in pentanol exhibit indefinite life above 1.25 monolayers of coverage where pentanol slips significantly on PFTS. Between 0.1 and 1 monolayer device lifetimes were increased but devices always failed. Devices in trifluoroethanol never exhibited extended lifetimes and trifluoroethanol does not slip on PFTS coated surfaces.

Devices exposed to pentanol vapors exhibited indefinitely long lifetimes above 1.25 monolayers (grey region), similar to earlier reports for pentanol condensing from partial pressures of nitrogen.¹³ Pentanol between 0.1 and 1 monolayer extended device operation but did not result in indefinite life, and consistently failed to lubricate at lower coverage. Pentanol's increase in slip time mobility with increasing coverage could be indicative of the formation and unpinning of 2D islands.^{19, 32} TFE meanwhile not only failed to lubricate, but *increased* the friction coefficient for all coverages studied (Figure

6.6 Supplemental Material).²¹ Successful lubrication was therefore firmly linked to adsorbate surface mobility, but not 3D capillary condensation or vapor replenishment effects.

6.4 SAM Reservoir Experiment

To test the ability of SAM to act as lubricant reservoirs, device lifetimes were compared in the presence and absence of SAM, and also with damaged SAM. Devices with undamaged SAM operated for over 2 million “residual” cycles (arrow labeled “Residual Ethanol + SAM/silicon) in vacuum after an initial exposure to 10 Torr of ethanol. (Figure 6.4) Damaging the SAM by imaging with a scanning electron microscope³⁴ caused the “residual” lifetime to decrease to about 150,000 cycles. Complete removal of the SAM (arrow labeled Residual Ethanol + Silicon) by UV-ozone cleaning resulted in a sharp plummet to approximately 10,000 cycles.

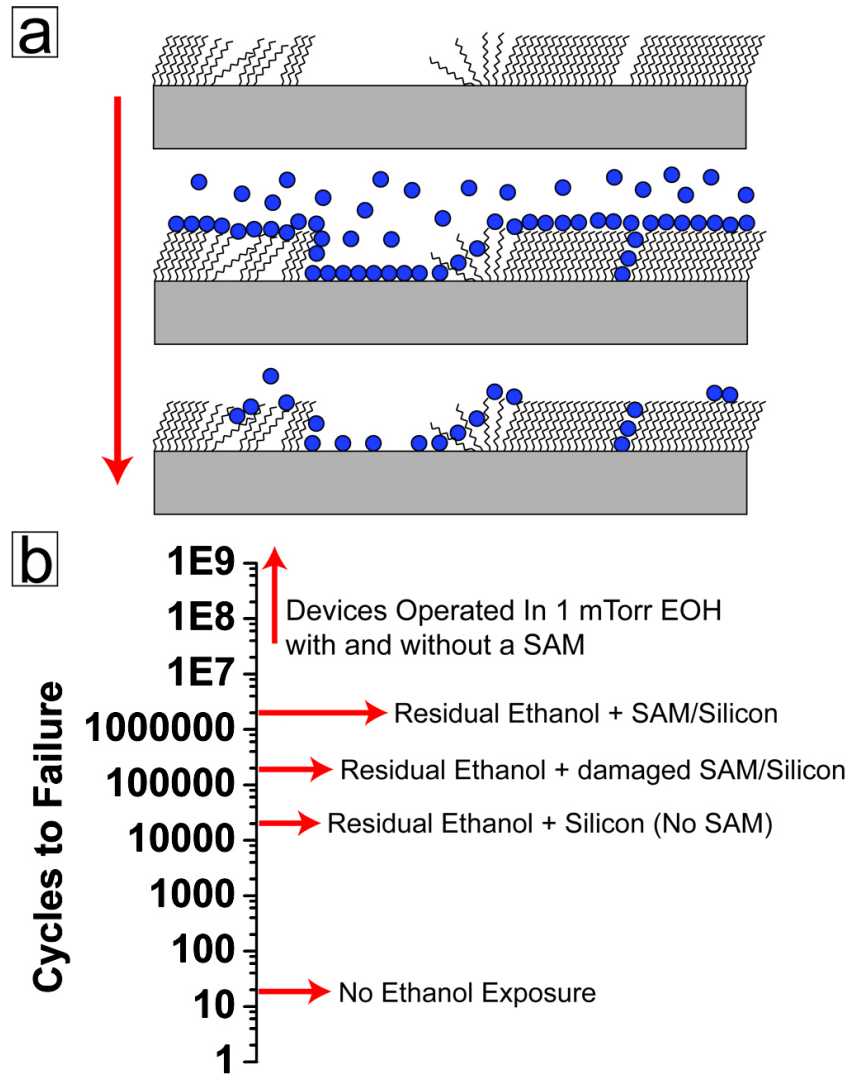


Figure 6.4 SAM Reservoir Effect Devices dosed with ethanol have varying lifetimes depending upon the surface onto which the ethanol is deposited. (a) depicts schematically the dosage process, in which a SAM-coated device (top panel) is exposed to a vapor of ethanol corresponding to 1 monolayer of surface coverage (middle panel), and the ethanol vapor is then removed (bottom panel). The monolayer provides a reservoir for the ethanol to replenish the contact area. (b) For devices oscillated at 200 Hz with undamaged SAM, dosage with one monolayer of ethanol will allow the device to operate for about 2×10^6 cycles (1×10^4 s). As the SAM layer is damaged by scanning electron microscopy and eventually completely removed, device lifetimes decrease by orders of magnitude.

6.5 Conclusion

We have utilized a MEMS based friction test device to record friction coefficients during operation in trace levels of ethanol, and found that devices remained operational for indefinitely long time periods in the presence of very low levels of surrounding gas. The mobility of ethanol on the surface was directly linked to its ability to provide lubrication, revealing a new type of lubrication regime at very low partial pressures. Devices also operated for very long residual periods after the surrounding ethanol gas was removed. The presence of a SAM enhanced this residual effect, evidently acting as a reservoir for the lubricant. The measurements reported here demonstrate both exceptionally high promise for successful lubrication of nano and microscale machinery, and also their high degree of sensitivity to adsorbed species. Furthermore the alcohol + SAM system provides an ideal model for theoretical calculations to determine the precise mechanism of lubrication and the role of mobility inside the contact area.

6.6 Acknowledgments

We thank J. E. Rutledge and S. H. Kim for helpful discussions. This work has been supported by the Extreme Friction MURI program, AFOSR # FA9550-04-1-0381, by NSF DMR0805204 and by Sandia National Laboratories. Sandia is a multi-program laboratory operated by Sandia Corporation, a Lockheed Martin Company, for the United States Department of Energy's National Nuclear Security Administration under contract DE-AC04-94AL85000.

References:

- 1) Krim, J. *Surf. Sci.* **2002**, 500, 741-758.
- 2) Lorenz, C. D.; Chandross, M.; Grest, G. S. *J. Adhesion Sci. Tech.*, **2010**, 24, 2453
(2010)
- 3) Savoulides, N. Development of a MEMS turbocharger and gas turbine engine. Ph.D. Thesis, Massachusetts Institute of Technology **2004**.
- 4) Dienwiebel, M.; et al. *Phys. Rev. Lett.* **2004**, 92, 126101.
- 5) Socoliuc, A.; Bennetwitz, R.; Gnecco, E.; Meyer, E. *Phys. Rev. Lett.* **2004**, 92, 134301.
- 6) Socoliuc, A. et al. *Science*. **2006**, 313, 207-210.
- 7) van Spengen, W. M.; Frenken, J. W. M. *Trib. Lett.* **2007**, 28, 149-156.
- 8) Timpe, S.; Alsem, D.; Hook, D. A.; Dugger, M. T.; Komvopoulos, K. *JMEMS* **2009**, 18, 229-238.
- 9) Panella, V.; Chiarello, R.; Krim, J. *Phys. Rev. Lett.* **1996**, 76, 3606-3609.
- 10) Mecke, K. R.; Krim, J. *Phys. Rev. B.* **1996**, 53, 2073-2092.
- 11) He, G.; Müser, M. H.; Robbins, M. O. *Science* **1999**, 284, 1650-1652.
- 12) McFadden, C. F.; Gellman, A. J. *Surf. Sci.* **1997**, 391, 287-299.
- 13) Asay, D. B.; Dugger, M. T.; Ohlhausen, J. A.; Kim, S. H. *Langmuir*. **2008**, 24, 155-159.
- 14) Miller, B. P.; et al. *Tribo. Lett.* **2010**, 38, 69-78.
- 15) Abdelmaksoud, M.; et al. *Langmuir*. **2006**, 22, 9606-9609.
- 16) Barnette, A. L.; et al. *Langmuir*. **2009**, 25, 13052-13061.

- 17) Barnette, A. L.; Asay, D. B.; Ohlausen, J. A.; Dugger, M. T.; Kim, S. H. *Langmuir*, published online August 15, **2010**, DOI: 10.1021/la101481c.
- 18) Miller, B. P.; Krim, J. *J. Low Temp. Phys.* **2009**, 157, 252-267.
- 19) Pisov, S.; Tosatti, E.; Tartaglino, U.; Vanossi, A. *J. Phys. Condens. Matter.* **2007**, 19, 305015.
- 20) Abdelmaksoud M.; Bender J.; Krim, J. *Phys. Rev. Lett.* **2004**, 92, 176101.
- 21) Methods Supplementary Online Material
- 22) Martin, J. M.; et al. *J. Phys. Chem.* **2010**, 114, 5003-5011.
- 23) Dhariwal, R.; Leonard, M.; Sriphung, C. *Proc. Inst. Mech. Eng. Part C J. Mech. Eng. Sci.* **2008**, 222, 65-72.
- 24) Rodahl, R.; et al *Rev. Sci Instrum.* **1995**, 66. 3924–3930
- 25) Asay, D.B.; and Kim, S.H. *Langmuir* **2007**, 23, 12174-12178.
- 26) Patton, S. T.; Zabinski, J. S. *Tribol. Int.* **2002**, 35, 373-379.
- 27) Ciraci, S.; Buldum, A. *Wear.* **2003**, 254, 911-916.
- 28) Irving, D. L.; Brenner, D. W. *J. Phys. Chem. B.* **2006**, 110, 15426-15431.
- 29) Wang, C. L.; Krim, J.; and Toney, M. F. *J. Vac. Sci. Tech. A* **7**, 2481 (1989)
- 30) Hedgeland H.; Fouquet P.; Jardine, A. P.; Alexandrowicz, G.; Allison, W.; Ellis, J. *Nature Physics.* **2009**, 5, 561-564.
- 31) Guerra, R.; Tartaglino, U.; Vanossi, A.; Tosatti, E., *Nature Mat.* **2010**, 9, 634-637.
- 32) Bruschi, L.; et al. *Phys. Rev. Lett.* **2006**, 96, 216101.
- 33) Krim, J. *Langmuir.* **1996**, 12, 4564.
- 34) Seshadri, K.; et al. *J. Phys. Chem.* **1996**, 100, 15900-15909.

Chapter 6 Supplemental Material

Methods and Materials

6.7 Device Description Operation and Chamber Preparation

The MEMS onboard friction test devices used in this study were fabricated by the Sandia National Laboratories Ultra-planar Multi-level MEMS Technology 5 (SUMMiT V) fabrication process¹, which includes a ground plane and four structural layers all consisting of highly doped n-type polysilicon. All of the layers were deposited by low-pressure chemical vapor deposition and etched by reactive ion etching. Silicon dioxide was used as the sacrificial layer and silicon nitride as an electrical isolation layer. The last process step involved the release of the test micromachines and the application by liquid deposition of a hydrophobic organic self-assembled monolayer (SAM) coating consisting of (heptadecafluoro-1,1,2,2 tetrahydrodecyl) trichlorosilane $\text{CF}_3(\text{CF}_2)_8\text{CH}_2\text{SiCl}_3$ (PFTS).² Application of a SAM is standard procedure in MEMS fabrication, to avoid capillary adhesion due to water. SAMs alone, however, do not prevent tribological failure, as they become damaged and/or worn in the course of rubbing contact.³ After fabrication, chips with several micromachines were wire bonded in 24-pin ceramic dual in-line packages for voltage application. Figure 6.1b shows a scanning electron microscope (SEM) image of the polysilicon micromachine used in this study. The micromachine includes a main shuttle for generating tangential (sliding) motion and two loading shuttles for applying a normal force at the sidewall surface of the main shuttle. In the experiments of this study, the desired normal force was generated by electrostatic actuation of the loading shuttles using conventional comb drives with interdigitated

fingers. Individual electrically isolated banks of comb-drive actuators on each side of the shuttle generated reciprocating motion. The two actuators of the main shuttle will be referred to as push and pull comb-drive actuators, while the two actuators of the loading shuttles, one close and the other remote from the contact interface, will be referred to as load and unload comb-drive actuators, respectively. The electrostatic forces generated by the main shuttle F_m and the loading shuttle F_l are given by⁴

$$F_m = \frac{1}{2} C_m (V_{push}^2 - V_{pull}^2) \quad (6.6)$$

$$F_l = \frac{1}{2} C_l (V_{load}^2 - V_{unload}^2) \quad (6.7)$$

where C_m ($=6.725 \times 10^{-9}$ F/m) and C_l ($=3.363 \times 10^{-9}$ F/m) are the capacitance per unit length of the comb drive actuators of the main and loading shuttles, respectively, V_{push} and V_{pull} are the voltages applied to the push and pull actuators of the main shuttle, and V_{load} and V_{unload} are the voltages applied to the load and unload actuators of the loading shuttle. The shuttles are supported by sets of double-folded flexure suspension systems whose spring constant can be determined by a linear fit of displacement versus applied voltage squared given by

$$\frac{1}{2} C_m (V_{push}^2 - V_{pull}^2) = k_m x \quad (6.8)$$

$$\frac{1}{2} C_l (V_{load}^2 - V_{unload}^2) = k_l x \quad (6.9)$$

where the left side components are equivalent to equations (6.8) and (6.9), k_m ($=0.384$ N/m) is the spring constant of the main shuttle's folded flexures, and k_l (0.128 N/m) is the spring constant of the loading shuttles' folded flexures.

The main shuttle possesses a long extension that allows contact with the two loading shuttle protrusions. When a voltage is applied to the comb drive actuators of the main shuttle, the structure moves parallel to the contacting interfaces, generating the shear (friction) force. The loading shuttles apply a normal force to the sidewall interfaces. A cylindrical protrusion at the end of each loading shuttle was brought into contact with the main shuttle by applying a suitable voltage to the comb drive actuators of the loading shuttle. The radii of the cylindrical protrusions are 50 μm and are 2.3 μm in height.

6.8 Self-assembled Monolayer Effect Experiment

The ethanol used in the experiments was anhydrous nondenatured 200 proof ethanol purchased from Sigma Aldrich. To measure the reservoir effect of self-assembled monolayer coating on MEMS, devices coated in PFTS were placed in the custom vacuum chamber and baked at approximately 150°C until the H₂O pressure measured with the RGA fell to below 5×10^{-10} Torr corresponding to an ultimate pressure of approximately 5×10^{-9} Torr when the chamber reached room temperature. The device was then oscillated at a peak to peak amplitude of approximately 20 μm by a sine wave at 200Hz. Initial failure measurements were taken to ensure any effect observed was due to addition of ethanol into the system and not tribological evolution of the device. As the device was being oscillated the load shuttles were brought into contact with the main shuttle and the load was increased to 500nN. Device lifetimes were then monitored by a Panasonic CCD camera mounted on a custom microscope assembly connected to a DVD recorder. Device failure was determined to be the point at which all motion ceased. Once the device ceased

to oscillate the loading structures were brought out of contact. This process was repeated 10 times to establish consistent baseline failure times. After a baseline failure time was determined a gate valve closed off the ion pump to the experimental chamber and ethanol was leaked into the chamber to a pressure of 10 Torr. This corresponded to a surface coverage of one monolayer. 5 minutes were given for the system to reach equilibrium and the vapor was removed. When the pressure in the chamber reached 1×10^{-7} Torr the loading shuttles were once again brought into contact and the load increased to 500nN. The failure time was then recorded. After failure the load was removed and immediately reapplied. The failure time was once again recorded and this process repeated until the failure time returned to that of the initial baseline values. The leak up pump out process was repeated 5 times to establish average failure times.

The device was then removed from the vacuum chamber and taken to an SEM to determine whether or any surface wear debris could be observed. After SEM images were taken the device was returned to the experimental chamber, baseline failure measurements were conducted and the ethanol leak in pump out failure measurements repeated as above. Since it is known that electron beams can degrade self assembled monolayers.⁵

Finally the device was removed from the chamber and placed in a UV-Ozone cleaner for 15 minutes to remove all remaining components of the self assembled monolayer.⁶ The device was returned to the experimental chamber and the pressure reduced to 5×10^{-9} Torr. The failure time process was once again repeated. Device

lifetime measurements were performed on three different devices located on two separate chips, with little variation observed from one device to another.

6.9 Quartz Crystal Microbalance Coverage and Sliptime Measurements

As the friction and lifetime experiments were being conducted a quartz crystal microbalance (QCM) was used to monitor the vapor uptake onto the chip in-situ. A thorough description of the QCM technique can be found elsewhere.⁷ Briefly a quartz crystal cut to oscillate in shear mode with an aluminum electrode was coated with PFTS and placed in the vacuum chamber along with the MEMS devices. The crystals are oscillated at resonance. As vapor is leaked into the chamber the deposition of mass onto the surface causes a shift in the crystal's resonant frequency, which can be measured.

The measurements give mass per unit area as a function of gas pressure down to the coverage measurement limit of $\Theta = 1 \times 10^{-2}$ monolayers. The QCM mass measurement is more or less independent of the mechanism by which a molecule adsorbs onto the surface. The more a molecule is decoupled (higher slip) from the surface the effective mass load on the QCM decreases meaning the frequency does not decrease as much for a given mass however the amplitude decreases (the resonance is damped). The mass load is then corrected for this decoupling. Therefore a chemisorbed molecule with no slip or extremely short slip is more accurately detected by a QCM frequency shift than a physisorbed molecule with a long slip time. However a relation to the amplitude shift corrects this.

To extrapolate the data down to the necessary minimum pressure/coverage range we modeled the isotherms with the Guggenheim-Anderson-de Boer equation, which allows for multilayer adsorption and is a modification of the classic BET equation.⁸ The fit gave good agreement with the isothermal uptake data and we extrapolated the adsorption isotherm down to a minimum coverage of $\Theta = 2 \times 10^{-5}$ monolayers at 10^{-4} Torr. (Figure 6.5)

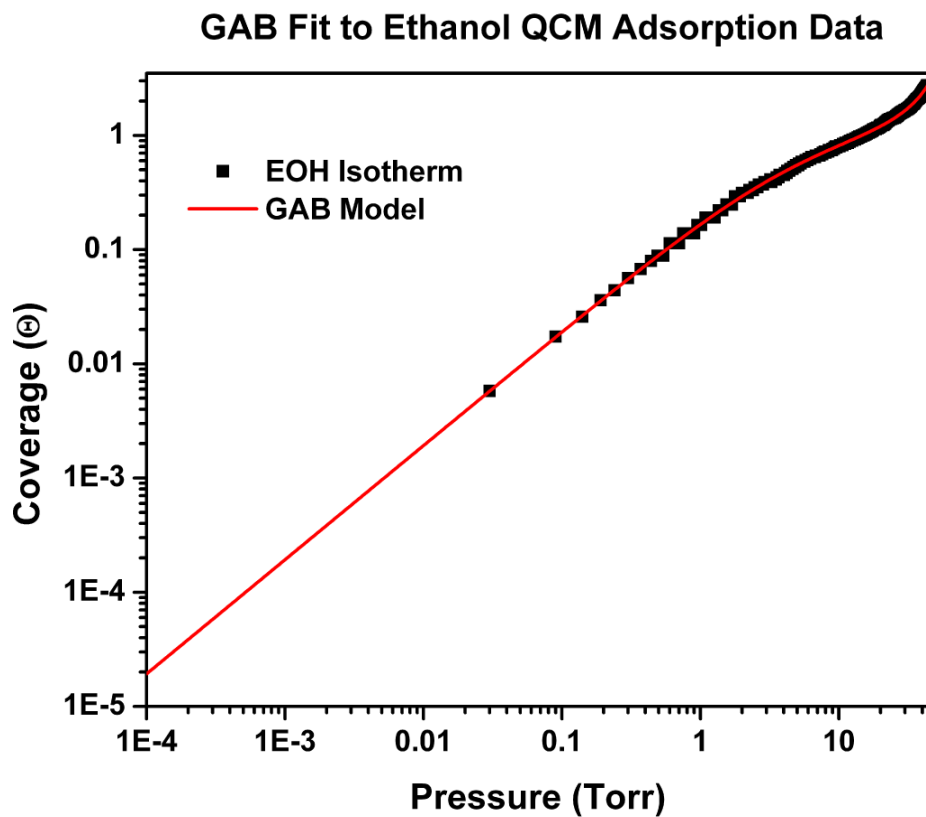


Figure 6.5 Ethanol adsorption data fit with the GAB equation and extrapolated down to the lowest pressure at which a change in coefficient of friction was observed.

The coverage determined by the QCM is likely very close to that of the actual device. A vast difference between the real/apparent ratios could cause a large variation between

coverages at the same pressure, however, the real/apparent surface area ratio for both the PFTS coated QCM and the MEMS device is less than 1.1. Therefore, roughness would introduce no more than a 10% uncertainty in coverage measurement.⁹ The film adsorption onto the crystal also shifts the amplitude of the crystals oscillation. Amplitude shifts are due to frictional shear forces exerted on the surface electrode by the adsorbed film. Characteristic slip times τ , and friction coefficients (i.e. shear stresses per unit velocity) η , are determined via⁷

$$\delta(Q^{-1}) = 4\pi\tau\delta f_0 \quad (6.10)$$

and

$$\eta = \frac{\rho_2}{\tau} \quad (6.11)$$

where ρ_2 is the mass per unit area of the adsorbed film and amplitude shifts are converted to quality factor shifts $\delta(Q^{-1})$ through calibration with nitrogen gas at room temperature.

6.10 Vapor Flux Rates

As a point of comparison the vapor flux rates were calculated for ethanol, TFE, and pentanol using kinetic theory. For ethanol, TFE, and pentanol in a contact area of $2 \times 10^{-15} \text{ m}^2$ the rate of flux at 1×10^{-4} Torr is 6.0×10^5 , 4.0×10^5 , and 4.3×10^5 molecules/s. At 1×10^3 Torr the flux rate is 6.0×10^6 , 4.0×10^6 and 4.3×10^6 molecules/s. At a sticking coefficient of as little as 1/100 and frequency of 200 Hz the time to replenish the surface coverage is comparable to the oscillation time for 1×10^{-4} Torr and an order of magnitude faster than the oscillation time at 1×10^{-3} Torr. At a sticking coefficient of 1/1000 the time

to replenish the contact at 1×10^{-4} Torr is an order of magnitude slower than the oscillation rate and at 1×10^{-3} Torr is comparable to the oscillation rate.

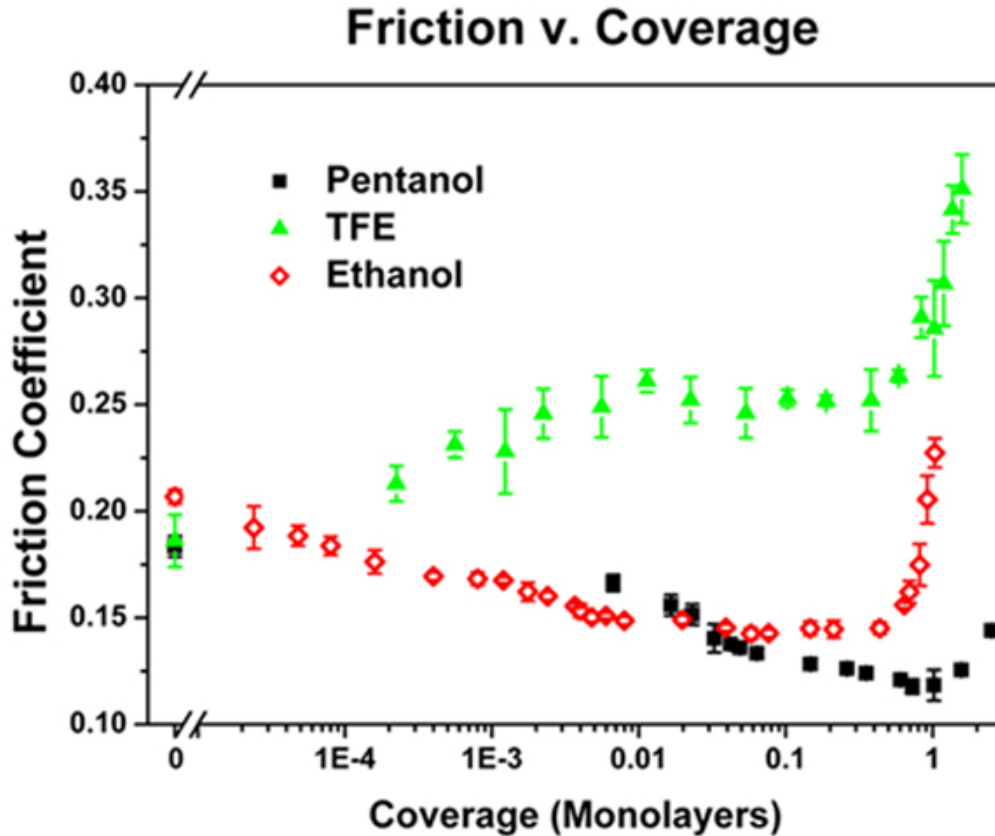


Figure 6.6 Friction coefficient versus coverage data for three test lubricants. Variations in vapor pressure are the reason for the difference in second coverage data points between the different lubricants. Only Pentanol and Ethanol lower to coefficient of kinetic friction.

References:

[1] J. J. Sniegowski and M. P. de Boer, *Annu. Rev. Mater. Sci.* **30**, 299 (2000)
[2] U. Srinivasan, M. R. Houston, R. T. Howe, and R. Maboudian, *Proc. of the 9th Inter. Conf. on Solid State Sens. and Act.* 210 (1997)

- [3] D. A. Hook, S. J. Timpe, M. T. Dugger, and J. Krim, *J. Appl. Phys.* **104**, 034303 (2008)
- [4] W. C. Tang, Ph.D. Thesis, University of California - Berkeley 1990
- [5] K. Seshardi, *et. al.*, *J. Phys. Chem.* **100**, 39 (1996)
- [6] D. A. Hook, J. A. Ohlhausen, J. Krim, and M. T. Dugger, *JMEMS* **19** (6), 1292 (2010)
- [7] B. P. Miller, J. Krim, *J. Low Temp. Phys.* **157**, 252 (2009)
- [8] M. M. Pradas, M. S. Sanchez, G. G. Ferrer, and J. L. G. Ribelles, *J. Chem. Phys.* **121**, 8524 (2004)
- [9] R. Rodahl, *et al* *Rev. Sci Instrum.* **1995**, 66. 3924–3930

Chapter 7

Evaluation of Oxygen Plasma and UV Ozone Methods for Cleaning of Occluded Areas in MEMS Devices

D. Adam Hook, James A. Olhausen, Jacqueline Krim and Michael T. Dugger

Article Published: JMEMS Vol 16 Dec 2010

Abstract - UV ozone and oxygen plasma treatments are two common procedures for cleaning silicon surfaces. The extent to which hidden surfaces of MicroElectroMechanical systems (MEMS) are cleaned by these methods has not been well-documented. In order to probe and compare the effectiveness of the two methods for cleaning occluded regions in MEMS, devices consisting of large moveable flaps were fabricated to produce hidden surfaces whose occluded regions exceeded the aspect ratios that typically occur in MEMS devices. The gaps between the flap and the substrate in the custom flap devices were designed to be variable in extent. Their interior regions were initially coated with chemisorbed monolayers and then subjected to cleaning. Both techniques removed monolayers on exposed surfaces and both, to some extent, removed monolayers present on the occluded surfaces. Oxygen plasma was found to be a far more effective method for cleaning the occluded surfaces than the UV ozone method. However in occlusions with exceptionally large aspect ratios of 1700:1 even oxygen plasma could not remove all traces of the chemisorbed monolayers.

7.1 Introduction

The dominant effects of surface forces on the operation of MicroElectroMechanical Systems (MEMS) necessitate control of the surface chemistry to control and mitigate these forces.¹ Cleaning is an important part of surface chemistry control, as attachment of chemisorbed monolayer films relies upon exposure of the desired coating molecules to a surface with known termination.¹ Variations in MEMS fabrication processes, for example, can result in a wide range of post-production surface chemistries while surface contamination routinely occurs during device storage and/or operation. UV ozone and oxygen plasma are two common methods used to clean and/or oxidize MEMS surfaces, particularly those with aluminum (mirror), gold (electrical switch), and silicon (mechanical interface) surfaces.²⁻¹⁵ UV ozone cleaning procedures for semiconductor materials were in use as early as 1972.² In this technique atmospheric air is exposed to ultraviolet light. Oxygen in the air absorbs UV light at 185 nm creating highly active ozone this ozone adsorbs UV light at 253.7 nm to form atomic oxygen. These react with surface organics to produce carbon-oxygen based products which desorb from the surface. Oxygen plasma techniques have been used for removal of organics in vacuum deposition techniques since the late 1950's.² Here plasmas generated in sub atmospheric pressures of oxygen create highly reactive ions which bombard a surface and react with organics forming volatile species (e.g. CO). These plasmas also contain significant kinetic energies therefore when colliding with a surface can also sputter-etch them.¹⁵ While a variety of studies have been performed that focus on the effectiveness of

these techniques for cleaning exposed surfaces of common MEMS materials, the extent to which occluded surfaces are cleaned has to date not been well documented.

The relative effectiveness of oxygen plasma and UV ozone for cleaning occluded and open areas of silicon MEMS devices are investigated here. MEMS devices with large moveable flaps were fabricated to include occluded regions that far exceed typical aspect ratios. The flaps were held closed during cleaning, and could be opened afterward to reveal areas that were occluded during the cleaning processes. The devices were coated with a chemically bonded monolayer of tridecafluorotris(dimethylamino)silane, $\text{CF}_3(\text{CF}_2)_5(\text{CH}_2)_2\text{Si}(\text{N}(\text{CH}_3)_2)_3$ or FOTAS before the cleaning treatment. Surface analysis using time-of-flight secondary ion mass spectrometry (ToF-SIMS) was performed on the surfaces after the flaps were opened in order to assess the effectiveness of the cleaning method. Both techniques effectively removed the FOTAS layer on exposed surfaces. Oxygen plasma was found to be a far more effective method for cleaning the occluded regions than the UV ozone method. It removed all traces of the chemisorbed layer except in occluded areas having exceptionally large aspect ratios of 1700:1.

7.2 Experiment Setup

7.2.1 MEMS Flap Structure Fabrication and Monolayer Treatment

Figures 7.1 and 7.2 show SEM images along with cross sections of the four styles of MEMS flap devices employed for these studies. All four devices have flaps with dimensions of 50 x 100 microns that can be flipped over to reveal areas that are occluded after release. The structures include hinges to assist in the flipping process as well as

latches to hold the flaps in place for surface analysis. The structures were designed and fabricated at Sandia National Laboratories, and have been used in the past to assess the ability of vapor deposited monolayers to penetrate into occluded areas of MEMS structures.¹⁶ The devices are fabricated using Sandia National Laboratories' SUMMiT V surface micromachining technology and are constructed from layers of polycrystalline silicon separated by sacrificial layers of silicon dioxide that are subsequently removed.¹⁷ Each layer can be patterned and etched, allowing complex structures to be fabricated. Figures 7.1a and 7.1b show SEM images and cross-sections of devices 1 and 3 respectively. Each SEM image in Figure 6.1 contains two identical flap structures. The upper device is shown in its as-fabricated state, and the bottom device shows the overturned flaps latched and ready for analysis. The flap on device 1 was fabricated from the poly 12 (P12) layer and the flap on device 2 was fabricated from the poly 3 (P3) layer. After release both rest flat on their respective underlayers, i.e. poly 0 (P0) for device 1 and poly 2 (P2) for device 3, as can be seen from the cross section schematics below the SEM images in Figure 7.1. Figures 7.2a and 7.2b show SEM images and cross sections of devices 2 and 4, respectively. Each SEM image shows two identical devices, in this case with the bottom device is in the as-fabricated state and the top device showing the flap turned over and latched into place. Devices 2 and 4 are identical to devices 1 and 3, respectively, except for the presence of dimples on their undersides, which prop them up so that the bottom of the flap in device 2 sits approximately 1.49 μm above the P0 layer, and the flap in device 4 sits approximately 1.63 μm above the P2 layer this is the gap height for both devices.

The minimum distance from the center of the flaps in devices 2 & 4 to the edge (25 μm), divided by the distance between the bottom of the flaps and the substrates, yield minimum gap aspect ratios of 17:1 and 15:1, respectively. These aspect ratios are less than that typically seen in MEMS gear-hub structures shown in Figure 7.3a, where gap aspect ratios are on the order of 100:1. Devices 2 and 4 therefore represent relatively open structures. However, the flaps do have gap aspect ratios typical of RF switches, such as the device shown in Figure 7.3b having aspect ratio of 10:1. In devices 1 and 3 some of the SUMMiT V design rules were intentionally violated to create gaps with extremely high aspect ratio. After release, the bottom of the flaps rest directly on the layer of polycrystalline silicon below, and the gap is defined by the roughness of both surfaces. Atomic force microscopy (AFM) measurements of the P0 surface and the bottom of P12 give an RMS roughness of 1.6 ± 0.1 nm and an asperity radius of approximately 480 ± 100 nm. Using only the gravitational force to prescribe the load ($\sim 1\text{nN}$) between the flap and the underlying substrate, a Greenwood-Williamson contact mechanics model gives a mean plane separation (gap) of approximately 14 nm. Therefore in Devices 1 and 3 the minimum gap aspect ratio is 1700:1.²¹ Inclusion of the adhesion forces that are undoubtedly present would decrease the gap, and create an even larger aspect ratio. As an example, if an adhesion force of $1\mu\text{N}$ is included the gap drops to 11nm and the aspect ratio increases to 2230:1.

The fabrication and etch process for SUMMiT V devices has been described in detail previously.¹⁷ Briefly, the sacrificial oxide was removed using an aqueous HF etch. They were then rinsed in deionized water, and transferred to methanol which was

supercritically extracted in CO₂ to avoid irreversible adhesion of the structures arising from liquid capillary forces. The devices were then transferred to a vacuum chamber for surface preparation and monolayer deposition. The devices were cleaned using an O₂/H₂O plasma, and coated with a monolayer of tridecafluorotris (dimethylamino) silane, CF₃(CF₂)₅(CH₂)₂Si(N(CH₃)₂)₃ or FOTAS. The dimethylamino groups can react exothermically with surface hydroxyl groups, and afford the potential for up to three covalent bonds with the surface per molecule, as illustrated schematically in Figure 7.4. This process results in a water contact angle by sessile drop of approximately 110 degrees. A complete description of the monolayer treatment process can be found elsewhere.²⁰ ToF-SIMS indicates that this coating process results in a surface coverage of approximately 2.5 x 10¹⁴ molecules/cm² on all surfaces exposed to the vapor, including areas of occlusion.¹⁶ This chemisorbed monolayer was then used as the controlled “contamination” layer that was subsequently used to evaluate the cleaning efficiency of UV ozone and oxygen plasma treatments. This particular layer was chosen because of its uniform coverage in open as well as occluded areas. In addition it is more thermally stable in oxidizing environments than other similar hydrocarbon based SAM layers.²² Finally it’s chemical bond to the surface makes it more difficult to remove than any heterogenous hydrocarbons deposited from the atmosphere. Therefore if either of the cleaning procedures employed here remove the layer then they are assured to remove hydrocarbons.

7.2.2 Cleaning Processes and ToF-SIMS Analysis

In the UV-Ozone cleaning process a MEMS die containing all four test devices coated in FOTAS was placed in an aluminum foil-lined Petri dish and placed in a UV ozone cleaner (Jelight model 144AX) for 15 minutes, along with the lid for the dish. After cleaning the dish was covered and carried to a probe station. There the flaps were manually turned over using tungsten whisker probes (Signatone model SE-20T) and latched into place. After all flaps were turned over to expose the occluded areas, the die were placed back in the Petri dish, covered, and transferred to the ToF-SIMS chamber for analysis. MEMS devices were placed in dishes containing Al foil in hopes that during transfer between the cleaning equipment and the surface analysis chamber, the cleaned foil would act as a strong adsorber of contaminants that would otherwise desorb and potentially deposit on the MEMS surfaces.

The oxygen plasma cleaning process was similar to that for UV ozone. A die containing all four test devices coated in FOTAS was placed in a foil-lined Petri dish and placed in a RF oxygen plasma cleaner (Yield Engineering, model Glen-R3A). The chamber was then evacuated and the oxygen plasma cleaning process commenced at 400 Watts in 110 - 115 mTorr of oxygen for 5 minutes. Once cleaned the devices were again transferred to the probe station, the flaps turned over and latched into place, and then taken to the ToF-SIMS analysis chamber. Both of these techniques reflect standard conditions used in cleaning of structures and representative surfaces.

Another MEMS die was placed in a foil-lined Petri dish, but did not go through any cleaning processes. The devices on this die were analyzed for comparison.

The ToF-SIMS monolayer analysis technique used in this study has been described thoroughly elsewhere.¹⁶ Briefly, a Physical Electronics TRIFT I ToF-SIMS system was used to generate positive secondary ion spectral images using a 25kV $^{69}\text{Ga}^+$ primary ion beam rastered over an area of 140x140 mm². To completely cover the full area of the flaps, four separate scans were acquired and the images concatenated together to form a spectral image montage. The montaged spectral image was then processed using Automated eXpert Spectral Imaging Analysis (AXSIA), a multivariate analysis routine developed at Sandia National Laboratories. It works by fitting self-generated spectral shapes to the data using least squares procedures and the number of chemical components is estimated through an eigenanalysis of the data cross-product matrix, essentially finding the minimum number of chemical components required to fully describe the spectral image.²³ Figure 5 shows an optical image of the four devices flipped, latched into place, and ready for SIMS analysis. The boxes indicate the entire analysis area.

7.3 Experimental Results and Discussion

Figure 7.6 shows the ToF-SIMS mean ion image montage for each of the four tested devices on each of the three die. The flaps are shown flipped over and latched into place. The latch structures can be seen on the left side of the flaps. AXSIA resolved two components of interest, and these are presented in Figures 7.7 and 7.8. Figure 7.7 shows the spatial locations of a “FOTAS” component in each of the analysis areas shown in Figure 6.5, along with the corresponding ion spectrum. Bright pixels correspond to areas

with high concentration of this component, while in the dark areas this component is absent. The FOTAS signature is dominated by C_xF_y fragments originating from the fluorocarbon backbone of the monolayer. It is clear that both the UV-Ozone and O_2 plasma cleaning techniques remove all of the FOTAS from the exposed surfaces of the entire flap structure. The figure shows that UV-Ozone leaves significant amounts of FOTAS in the occluded areas, corresponding to where the flaps covered the substrate when the devices were treated with FOTAS. Matching patterns of FOTAS can be observed on the bottom of the opened flaps, and on the corresponding areas of the substrate that were covered during FOTAS treatment. The most residual FOTAS is present on device 3, while in contrast most of the FOTAS was removed under device 4. Here the UV-Ozone appears to have removed the FOTAS approximately 18 microns into the occlusion. In device 2, which has the same general geometry but is fabricated by layers closer to the P0 layer and has a slightly higher aspect ratio, the penetration depth was only about 10 microns. UV-Ozone's inability to penetrate can be attributed to its fairly short mean free path at atmospheric pressure (11 nm at 760 Torr (1 atm) using the kinetic theory of gases). The classical phenomenological model of diffusion shows a direct relation between mean free path and the diffusion coefficient.²⁴ A short mean free path (ie small diffusion coefficient) makes it difficult for the ozone and reactive oxygen generated outside of the gap to diffuse deeply into the gap before colliding with other gas molecules, losing energy and recombining to form less reactive molecular oxygen, ie limiting the lifetime of the generated ozone and oxygen radicals when they travel into the occlusion. Lowering the total pressure in the UV-Ozone environment would increase the

mean free path and likely allow deeper penetration into the occlusion. Another factor that affects the ability of UV-Ozone processes to clean is the percentage of molecular oxygen present in the air. An increased molecular oxygen concentration would lead to higher ozone and atomic oxygen concentrations that would likely increase the cleaning efficiency and possibly penetration depth. However, in our particular UV-Ozone cleaner controlled variations in total pressure and oxygen concentration are not available. Variations in surface roughness and the state of the flap before cleaning make it difficult to draw quantitative conclusions about penetration depth of UV-Ozone from the ToF-SIMS data, but it is clear that UV-Ozone cleaning in air is not capable of removing carbonaceous contaminants from high aspect ratio occlusions.

The O₂ plasma cleaning technique showed vastly superior cleaning capabilities to that of UV-Ozone. After cleaning for only 5 minutes, no FOTAS was seen inside of the relatively open occlusions of devices 2 and 4, and only trace amounts were observed in the high aspect ratio occlusions of devices 1 and 3. Here it is probable that increasing the cleaning time for the O₂ plasma by as little as 5 minutes could completely clean the devices with high aspect ratio gaps. The mean free path of oxygen ions at 100 mTorr, neglecting additional energy generated by the ionization process, is 140μm. This is significantly higher than that of UV-Ozone at atmospheric pressure, and allows diffusion throughout the deep occlusions. While simulation of reactive ion trajectories down deep trenches would need to be conducted for a thorough discussion of the limits of this technique it is clear that these aspect ratios have not yet reached this limit. The increased kinetic energy of oxygen ions in plasmas can also sputter-clean surfaces, whereas UV-

Ozone only has a reactive cleaning component. However, this sputtering process can potentially have negative consequences. The ToF-SIMS data shows an aluminum component in the spectral images for O₂ plasma-cleaned devices, as shown in Figure 7.8. No aluminum is seen in the as-deposited FOTAS die or the UV ozone cleaned die, ruling out aluminum deposition from outside influences or deposition in the ToF-SIMS chamber. The O₂ plasma cleaned die exhibit aluminum deposition on all exposed surfaces, but not in the occlusions, consistent with line-of-sight physical vapor deposition. The aluminum may have originated from the foil lining the Petri dish in which the die were sitting, or from the oxygen plasma cleaning chamber electrodes, since it is known that plasma can sputter metals from the generating electrodes.^{2,15} Therefore when using O₂ plasma to clean MEMS, care should be taken to ensure that the plasma power used does not generate metals from the plasma electrodes or surrounding materials, or that the sputtered species are not detrimental to the MEMS device operation by changing surface chemistry or shorting electrical connections. An optimum plasma power should be found that removes the undesired contamination species but does not result in the deposition of foreign sputtered materials.

7.4 Summary

Oxygen plasma and UV-Ozone cleaning techniques were used to remove FOTAS molecules from flap test structures designed to mimic exposed and high-aspect ratio occluded areas. Both UV-Ozone and O₂ plasma remove FOTAS from exposed surfaces of silicon MEMS. UV-Ozone cleaning (15 minutes in 1 atmosphere of air) fails to

penetrate into deep occlusions. The O₂ plasma conditions used (400 Watts in 110 - 115 mTorr of oxygen for 5 minutes) resulted in penetration into occlusions better than UV-Ozone, completely removing all traces of FOTAS from underneath relatively open geometries while leaving trace amounts of FOTAS underneath extremely high aspect ratio occlusions. However, these conditions also left behind residual aluminum deposits.

7.5. Acknowledgments

The AFOSR Extreme Friction MURI F49620-01-1-0132/FA9550-04-1-0381 and Sandia National Laboratories are gratefully acknowledged for supporting the work reported here. Sandia is a multi-program laboratory operated by Sandia Corporation, a Lockheed Martin Company, for the United States Department of Energy's National Nuclear Security Administration under contract DE-AC04-94AL85000.

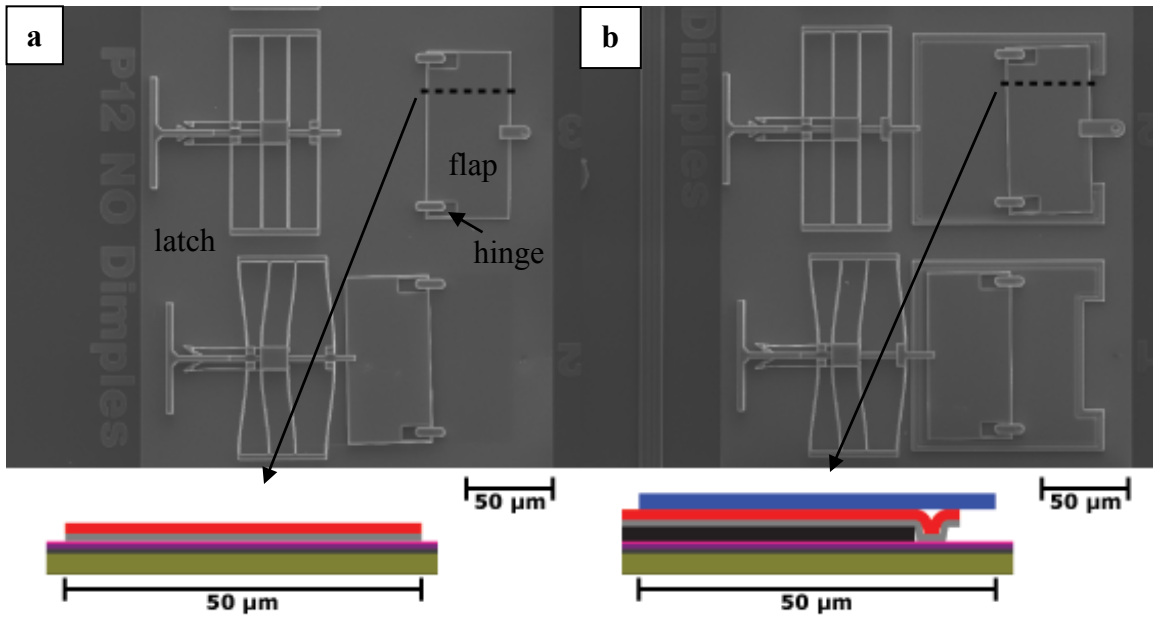


Figure 7.1 Scanning electron micrographs of (a) device 1 and (b) device 3 in the as-fabricated (upper) and flipped (lower) states with cross sections in the as-fabricated position. The cross-sections show polySi layers as gray, red, and blue, while the sacrificial oxide is black, and the other layers represent the wafer substrate and dielectric stack.

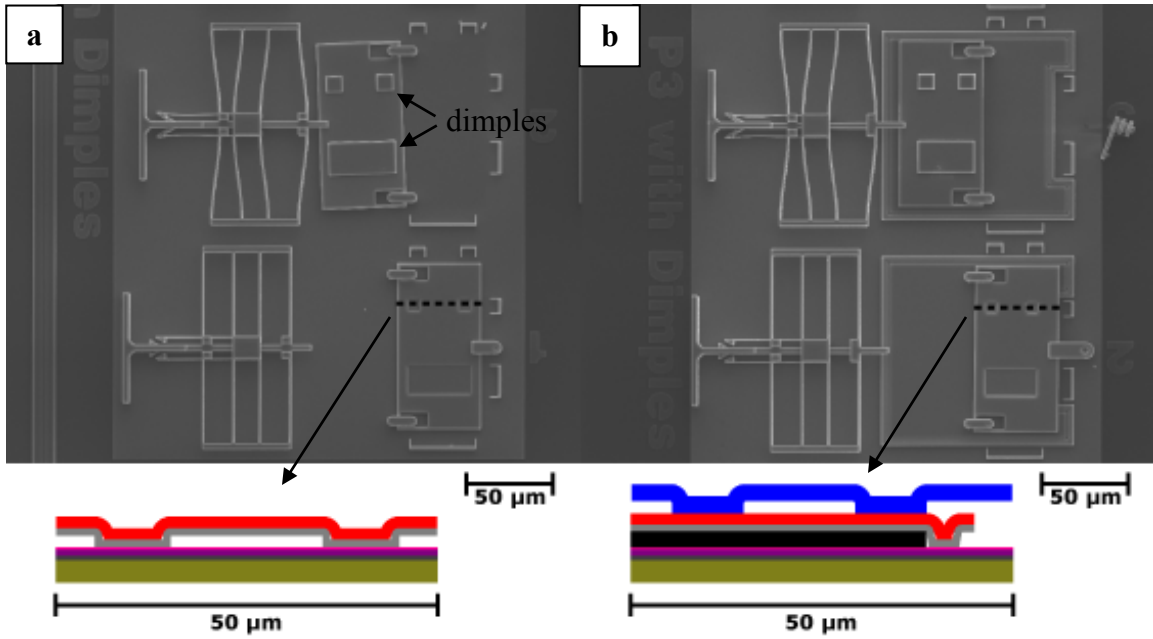


Figure 7.2 Scanning electron micrographs of (a) device 2 and (b) device 4 in the as-fabricated (lower) and flipped (upper) states with cross sections in the as-fabricated position. The cross-sections show polySi layers as gray, red, and blue, while the sacrificial oxide is black, and the other layers represent the wafer substrate and dielectric stack.

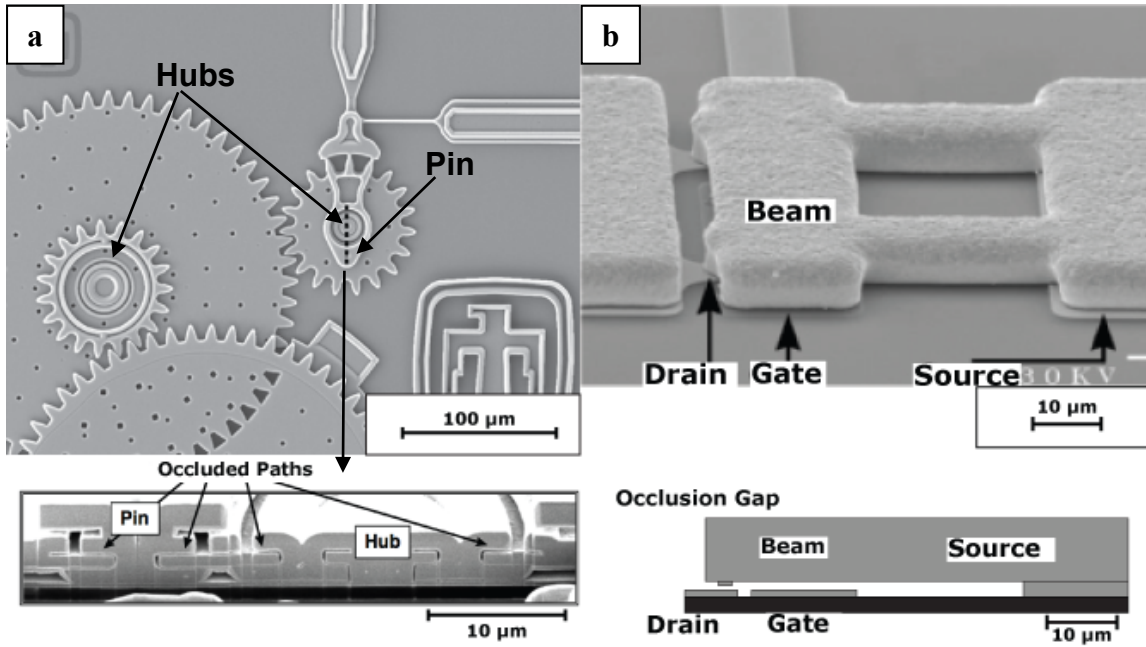


Figure 7.3 Scanning electron micrograph of (a) Sandia's microengine and gear train [18, 20], and (b) Northeastern University's cantilever RF-MEMS switch [19].

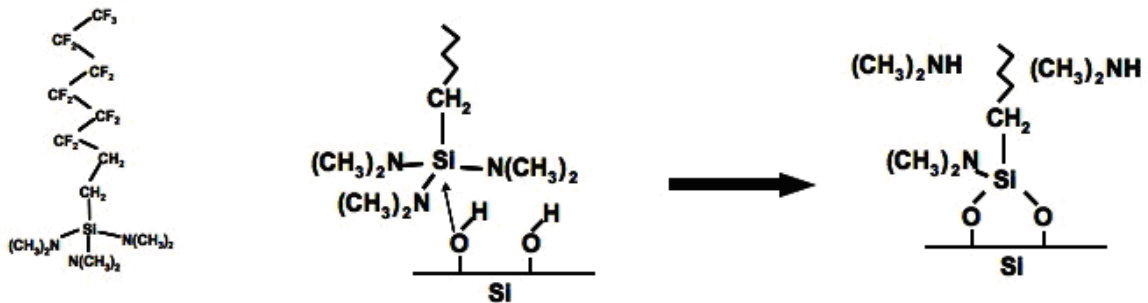


Figure 7.4 Schematic representation of the FOTAS reaction with a hydroxylated silicon surface.

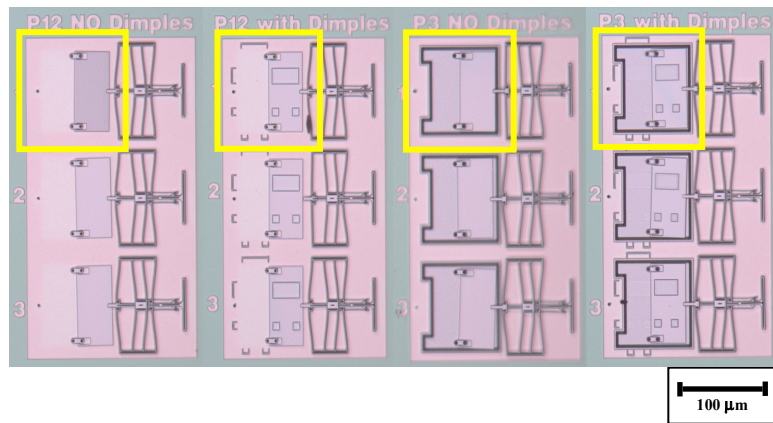


Figure 7.5 Optical microscope image of (from left to right) flap devices 1, 2, 3, and 4. Flaps are shown flipped and latched into place. Yellow boxes indicate ToF-SIMS analysis areas for each device.

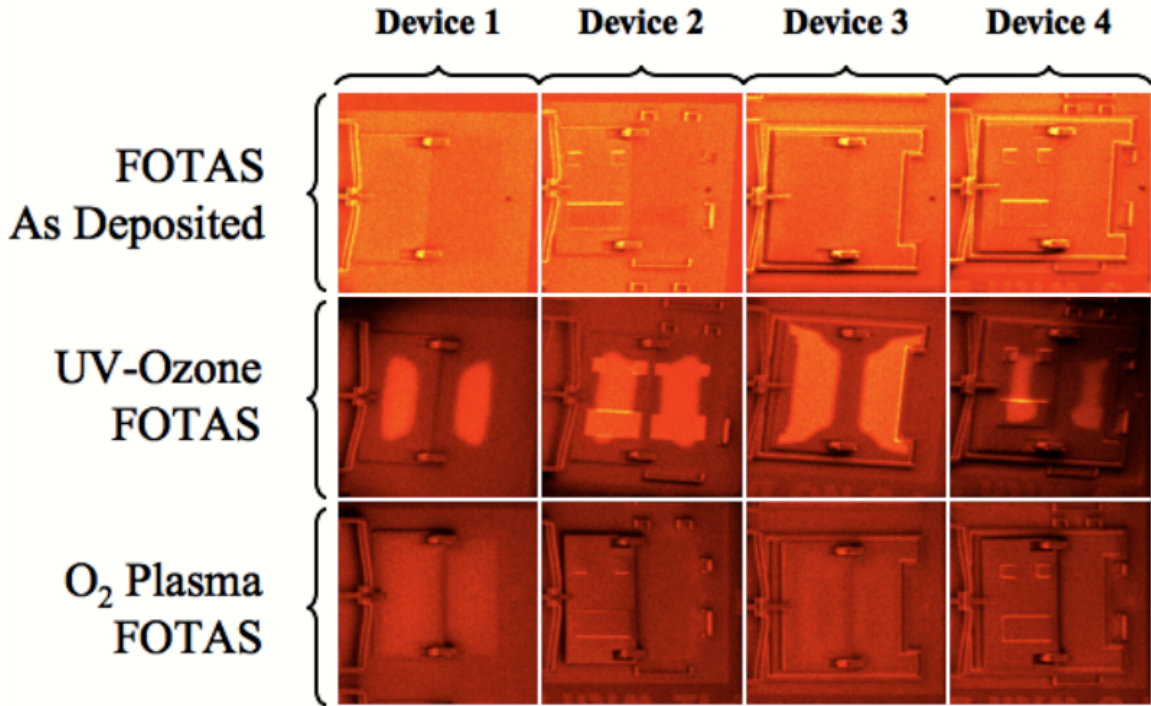


Figure 7.6 ToF-SIMS mean ion image montage of flaps as-deposited with FOTAS, UV ozone cleaned, and O₂ plasma cleaned. Each flap has been turned over and latched into place. Each analysis area is 140x140 mm². Contrast in this image originates both from chemical differences and from topography, allowing easy identification of the structures in the analysis.

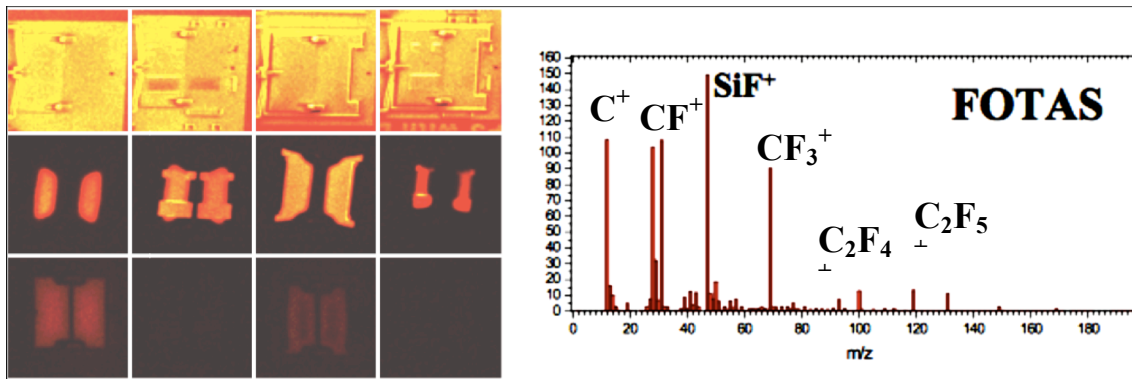


Figure 7.7 AXSIA analysis of the die montage showing the FOTAS component. Device numbers and cleaning processes correspond to the relative placements in Figure 7.6.

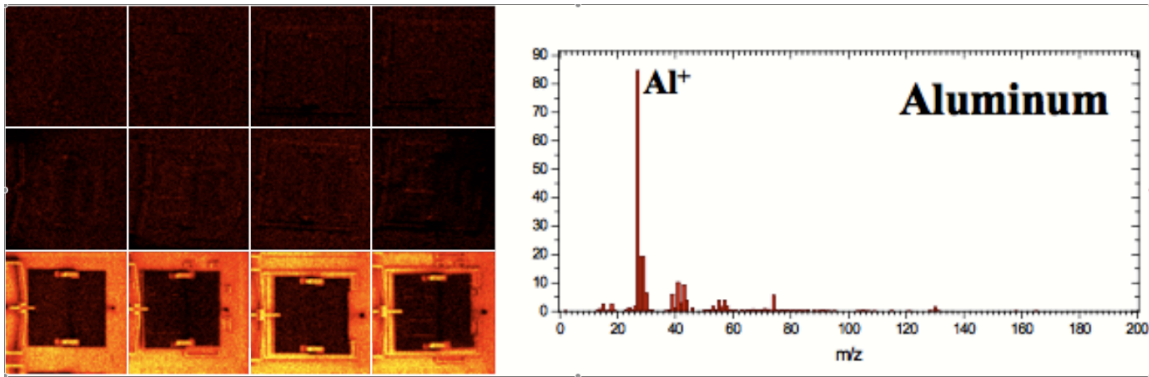


Figure 7.8 AXSIA analysis of the die montage showing an aluminum component. Device numbers and cleaning processes correspond to the relative placements in Figure 6. Only the O₂ plasma cleaning technique showed any trace of aluminum. Aluminum is only seen in exposed areas of the device.

References

- [1] R. Maboudian and C. Carraro, *J. Adhesion Sci. and Technol.*, vol. 17, pp. 583-592, Apr. 2003.
- [2] L. Holland, *Vacuum Deposition of Thin Films*. New York: Wiley, 1960
- [3] D. A. Bolon and C. O. Kunz, *Poly. Eng. And Sci.* vol. 12, pp. 109-111, Mar. 1972.
- [4] J. R. Vig and J. W. Le Bus, *IEEE Trans. Parts, Hybrids and Packaging*, vol. 12, pp. 365-370, Dec. 1976.
- [5] P. Erikson, J. Y. Andersson, and G. Stemme, *J. Microelectromech. Syst.*, vol. 6, pp. 55-61, Mar. 1997
- [6] Y. Berdichevsky, J. Khandurina, A. Guttman, Y.-H. Lo, *Sens. And Act. B*, vol. 97, pp. 402-408, 2004
- [7] D. Gao C. Carraro, R.T. Howe, and R. Maboudian, *Trib. Lett.*, vol. 21, pp. 226-232
- [8] A. B. Frazier, H. A. Chong, and M. G. Allen, *Sens. And Act. A*, vol. 45, pp.47-55, Oct. 1994.

- [9] K. Arita, K. Noda, and T. Asano, *IEEE/CPMT Berlin Int'l Elec. Man. Tech. Symp.*, pp. 92-97, Apr. 1998.
- [10] A. Tran, Y. H. Lo, Z. H. Zhu, D. Haronian, and E. Mozdy *IEEE Photon. Tech. Lett.*, vol. 8, pp. 393-395, Mar. 1996.
- [11] M. Bartek and R. F. Wolffenbuttel, *J. Micromech. Microeng.*, vol. 8, pp. 91-94, June 1998.
- [12] S. E. Lin, *Surf. Coat. And Tech.*, vol. 173, pp. 47-57, Aug. 2003.
- [13] A. Yu, A. Q. Liu, J. Oberhammer, Q. X. Zhang, and H. M. Hosseini, *J. Micromech. Microeng.*, vol. 17, pp. 2024-2030, Sep. 2007.
- [14] Kern W and Reinhardt K A, *Handbook of Silicon Cleaning Technology*. Norwich, NY: William Andrew, 2008
- [15] J. L. Vossen, *J. Phys. E: Sci. Instrum.*, vol. 12, pp. 159-167, 1979
- [16] J. A. Ohlhausen, and K. R. Zavadil, *J. Vac. Sci. Technol. A*, vol. 24, pp. 1172-1178, July 2006.
- [17] J. J. Sniegowski and M. P. de Boer, *Annu. Rev. Mater. Sci.*, vol. 30, pp. 299-333, Aug. 2000.
- [18] <http://mems.sandia.gov/gallery/image>
- [19] S. Majumder, N. E. McGruer, G. G. Adams, P. M. Zavracky, R. H. Morrison, and J. Krim," *Sens. and Act. A*, vol. 93, pp. 19-26, Aug. 2001.
- [20] M. G. Hankins, P. J. Resnick, P. J. Clews, T. M. Mayer, D. R. Wheeler, D. M. Tanner, and R. A. Plass, *Proc. SPIE*, vol. 4980, pp. 238-247, 2003.

- [21] J. A. Greenwood and J. B. P. Williamson, *Proc. of the Royal Soc. of London. Series A, Math. and Phy. Sci.*, vol. 295, pp. 300-319, 1966
- [22] M.T. Dugger, R.J. Hohlfelder, and D.E. Peebles, *Proc. SPIE – The Inter. Soc. for Opt. Eng.*, vol. 4980, pp. 138-150, 2003
- [23] J. A. Ohlhausen, M. R. Keenan, P. G. Kotula, and D. E. Peebles, *Appl. Surf. Sci.*, vol. 231-232, pp. 230-234, June 2004.
- [24] E.L. Cussler, *Diffusion: Mass Transfer in Fluid Systems*, Cambridge, UK, Cambridge University Press, 1997.

Chapter 8

Conclusions and Future Work

8.1 Summary of Results and Impact

For MEMS contacts with normal loads of 750nN, those typical of MEMS operational conditions tightly bonded fluorinated self-assembled monolayers do not prevent tribological degradation in oscillating sliding contacts nor do they hold up to repeated normal contacting conditions. It was seen that the energy imparted to the surface through friction and normal loading is sufficient to break the covalent silicon – oxygen bonds that attached the layers to the surface. Therefore long term solutions to friction and wear need to be examined such as a mobile surface layer delivered by a surrounding vapor.

It has also been seen that these devices enter into two very distinct failure regimes. The first being a low adhesion/high wear regime and the other being a high adhesion/low wear regime. Nanoscale wear may increase the surface energy through the removal of the native oxide film, organic monolayer coating, and any adsorbed contaminant, leading to the cessation of the micromachine oscillation. Although third-body wear debris may extend the operation life by preventing intimate surface contact, wear debris entrapment and agglomeration at the sliding interface could be detrimental to the device functionality. This is particularly important in contact-mode applications, such as microswitches, where intimate surface contact is essential, and micromirrors, where displaced debris can interfere with the optical performance.

It has been and found that devices remained operational for indefinitely long time periods in the presence of very low levels of surrounding ethanol gas. The mobility of ethanol on the surface was directly linked to its ability to provide lubrication, revealing a new type of lubrication regime at very low partial pressures. Devices also operated for very long residual periods after the surrounding ethanol gas was removed. The presence of a SAM enhanced this residual effect, evidently acting as a reservoir for the lubricant. The measurements reported here demonstrate both exceptionally high promise for successful lubrication of nano and microscale machinery, and also their high degree of sensitivity to adsorbed species. Furthermore the alcohol + SAM system provides an ideal model for theoretical calculations to determine the precise mechanism of lubrication and the role of mobility inside the contact area.

Finally it is shown that UV-Ozone and Oxygen plasma are both effective methods of removing surface contaminants from open areas in MEMS devices either in preparation for controlled surface treatments or to establish perfectly known surfaces for further fundamental friction and lubrication studies. It was however found that the higher energies of oxygen plasma as well as its long mean free path make it the ideal cleaning method for devices with highly occluded areas.

8.2 Future Work

To better understand the role of surface mobility in lubrication of microstructures it is necessary to eliminate each variable and build. The next step in these experiments is to remove the self-assembled monolayer in-situ and conduct friction measurements of

freshly cleaned device surfaces. This will eliminate any contribution of adsorbed water or hydrocarbons associated with transfer in open atmosphere and build from a completely clean surface. It is evident that the quartz crystal microbalance is an important tool and the continuing examination of a wide variety of adsorbates is paramount in discovering the specific properties of lubricants. Mobility measurements of molecules of non-polar molecules such as pentane and ethane would give insight into the role of the hydroxyl group on mobility and lubrication. After QCM determination of possible lubrication candidates then MEMS tribometers can be used to test the effectiveness of each lubricant and a more thorough picture of mechanisms of lubrication can emerge. Also new microtribometer designs with multiple contact controls per device will lead to a more efficient experimentation and multiple use of each individual device.